Silicon Nanocrystals for Silicon Photonics

Thesis by
Robert Joseph Walters

In Partial Fulfillment of the Requirements
for the Degree of
Doctor of Philosophy

California Institute of Technology
Pasadena, California

2007

(Defended May 24, 2007)

To the memory of my grandfathers,

Jean Owen Thibault

(1923–2003)

and

Glenn Arthur Walters

(1920–1998)

Acknowledgements

Just over six years ago, I called up the chair of applied physics at Caltech, Harry Atwater, and asked about working somewhere in the department during the summer before I would begin my graduate studies. He found a position for me in his lab and I accepted, without fully realizing the terrific opportunity that he was offering me. I've been happily working for Harry ever since. I've always thought Polanyi got it right when he described the training of a scientist as an apprenticeship. Harry's approach to science will always be indelibly imprinted on my own career. I am grateful to acknowledge his superb mentorship and guidance over the years.

One of the advantages of working for Harry has been the excellent group of fellow students that I have had the pleasure to work with in his lab. In particular, I have collaborated with Julie Biteen, Julie Brewer, Ryan Briggs, Tao Feng, Dean Holunga, and Gerald Miller on silicon nanocrystal related projects. Tao contributed directly to this thesis through his work on nanocrystal characterization presented in section 2.2 and in the electrostatic modeling calculations in section 4.9. I've very much enjoyed having a front row seat to the growing field of plasmonics through the work of Jennifer Dionne, Stefan Maier, Carrie Ross, and Luke Sweatlock. I also have a great admiration for those in the group that have devoted their time to alternative energy research and I've always thought that our group's research in wafer bonding might eventually end up doing more to enable practical integrated photonic circuits than my own work in silicon nanocrystals. In addition to those already named, I have shared my time in the Atwater Group with (in alphabetical order): Melissa Archer, Rhett Brewer, Claudine Chen, Davis Darvish, Matthew Dicken, Ken Diest, Vivian Ferry, Jason Holt, Brendan Kayes, Michael Kelzenberg, Greg Kimball, Beth Lachut, Krista Langeland, Maribeth Mason, Morgan Putnam, Imogen Pryce, Regina Ragan, Cecily Ryan, Christine Richardson (who helped me collect data for figure 5.13), Jennifer Ruglovsky, Katsu Tanabe, Darci Taylor, and Jimmy Zahler. It has been a pleasure.

Additionally, I want to acknowledge the postdoctoral scholars and visiting scientists that have worked in the Atwater Group during my time at Caltech. I am particularly grateful to have worked closely with Domenico Pacifici, who has been extremely generous with his time in helping me refine this thesis. During my early years, I learned my way around the optics lab with a lot of help from Pieter Kik. Henri Lezec, a focused ion beam virtuoso,

is responsible for the sample fabrication described in section 5.4 of this thesis. I have also enjoyed working with Chang-Geun Ahn, David Boyd, Mark Brongersma, Michael Filler, Anna Fontcuberta í Morral, Sungjee Kim, Keisuke Nakayama, and Young-Bae Park.

I would also like to acknowledge several other students in the applied physics department with whom I have had productive conversations about my research: Deniz and Andrea Armani, Paul Barclay, Matt Borselli, Vikram Deshpande, Tom Johnson, Tobias Kippenberg, Deepak Kumar, Mary Laura Lind, Brett Maune, Raviv Perahia, and Sean Spillane. I want to thank the staff of the applied physics department including April Neidholt, Eleonora Chetverikova, Carol Garland, Ali Ghaffari, Irene Loera, and Cierina Marks. My apologies to those that I am undoubtedly forgetting.

I have twice had the pleasure of traveling to FOM-AMOLF in Amsterdam to complete experiments in the laboratory of Albert Polman. Albert also visited Pasadena on sabbatical in the fall of 2003, during which time he measured the majority of the data discussed in section 5.2. I have always been impressed with Albert's ability to simplify confusing results down to a few essential conclusions. I am happy to acknowledge several of Albert's students, including Michiel De Dood, Teun van Dillen, Jeroen Kalkman, Hans Mertens, Joan Penninkhof, Anna Tchebotareva, and Ernst Jan Vesseur. Michiel and Jereon both contributed to the work described in section 2.6.

I also want to note the contributions to section 2.4 of this thesis made by Nick Chiang during his SURF project in the summer of 2003 and during his senior thesis work. Most of the work presented in section 4.5 was completed by Josep Carreras, who visited Caltech from the University of Barcelona in the fall of 2004.

I have also worked closely with Doug Bell and Mihail Petkov of the Jet Propulsion Laboratory on aspects of silicon nanocrystal memory. Doug is responsible for some of the calculations given in section 4.9 and Mihail helped to develop a packaging process for the optical memory devices as shown in figure 3.8.

Robert Lindstedt, Maria Giorgi, and George Bourianoff of Intel Corporation were instrumental in the design and fabrication of our optical memory samples (section 3.4) during our early collaboration.

I greatly appreciate the effort of Yann Leroy, Bertrand Leriche, and Anne-Sophie Cordan, who were kind enough to simulate tunneling processes in my device geometry in late 2006. Their results are mentioned in section 4.9.

I am also appreciative of the financial support I received through a National Defense Science and Engineering Graduate (NDSEG) fellowship and also through a fellowship from the Intel Foundation. I thank Kyu Min for serving as my fellowship mentor at Intel. My research was also funded in part by the Air Force Office of Scientific Research under the direction of Gernot Pomrenke.

I have been fortunate to work in a field that is competitive and congenial at the same time. I am particularly grateful for the encouragement I have received at conferences from Philippe Guyot-Sionnest, Philippe Fauchet, Minoru Fujii, Francesco Priolo, Jan Linnros, and Jung Shin.

I'm happy to have made too many friends in my years at Caltech to list here. I will only say that I have had a great time and that although the time has come for me to graduate, I am in no hurry to leave. My family has also been a continual source of support and encouragement over the years.

Finally, I want to thank and acknowledge my thesis examination committee: Professors Harry Atwater, Marc Bockrath, Oskar Painter, and Kerry Vahala.

Robb Walters

May 2007

Pasadena, CA

Abstract

In the absence of suitable methods for integrating traditional semiconductor optoelectronic materials in CMOS microelectronic fabrication processes, nanostructured silicon has been actively explored as an alternative light emitter for silicon photonics. This thesis presents new experimental results in silicon nanocrystal photophysics and optoelectronics, including novel device designs for optical memory elements and light-emitting structures.

As quantum dots, silicon nanocrystals exhibit several interesting properties including size-tunable emission over visible and near-infrared wavelengths and improved oscillator strength for radiation. In contrast to bulk silicon, nanocrystals can emit light with quantum efficiencies approaching 100%. Through time-resolved photoluminescence measurements, we first quantitatively establish that the dense ensembles of nanocrystals that are attractive in device applications retain these advantages. We then describe the fabrication of fully CMOS compatible silicon nanocrystal optoelectronic test structures and show that such devices can function as room temperature optical memory elements.

We further demonstrate that electroluminescence can be achieved in our devices through a previously unreported process we call *field effect electroluminescence*, in which sequential charge carrier injection is used to create excitons in silicon nanocrystals. This mechanism is a promising approach for overcoming the difficulty inherent in electrically exciting silicon nanocrystals, which are necessarily surrounded by an electrical insulator. Finally, we present electrically excited infrared light sources that combine carrier injection through the field effect electroluminescence mechanism with near field energy transfer from silicon nanocrystals to infrared emitters.

Contents

List of Figures

List of Tables

List of Publications

Portions of this thesis have been drawn from the following publications:

Silicon nanocrystal field-effect light-emitting devices. R. J. Walters, J. Carreras, T. Feng, L. D. Bell, and H. A. Atwater, IEEE Journal of Selected Topics in Quantum Electronics, **12**, 1647, November/December 2006

Photoluminescence quantum efficiency of dense silicon nanocrystal ensembles in SiO_2. R. J. Walters, J. Kalkman, A. Polman, H. A. Atwater, and M. J. A. de Dood, Physical Review B **73**, 132302, April 2006

Field-effect electroluminescence in silicon nanocrystals. R. J. Walters, G. I. Bourianoff, and H. A. Atwater, Nature Materials **4**, 143, January 2005

Silicon optical nanocrystal memory. R. J. Walters, P. G. Kik, J. D. Casperson, H. A. Atwater, R. Lindstedt, M. Giorgi, and G. Bourianoff, Applied Physics Letters **85**, 2622, September 2004

Chapter 1

Introduction

1.1 Moore's Law and Silicon Technology

It is an understatement to remark that we live in a world made possible by silicon technology. Modern life has been shaped and defined by innumerable products that rely on integrated electronic circuits fabricated in mind-boggling number and precision on silicon wafers. The grand success of silicon technology is not only the dramatic improvements that have been achieved in performance, but also the exponentially decreasing per-component manufacturing costs that have kept that performance affordable. In fact, Gordon Moore's famous law describing progress in the semiconductor industry was originally stated in similar economic terms:

> The complexity for minimum component costs has increased at a rate of roughly a factor of two per year..., this rate can be expected to continue... [1]

Complexity is usually equated to transistor count, and by that measure the exponential progress predicted by Moore's Law has been maintained through the present day (figure 1.1). It has become cheaper over time to pack more and more transistors into integrated circuits because each individual transistor is continually being made smaller. This scaling process allows more powerful chips with more transistors to be made for a reasonable price. Smaller transistors also drive down the price of previous generation chips of any given complexity, because more functionally identical copies can be simultaneously made on the surface of a silicon wafer for nearly the same cost. Scaling is the engine of progress in silicon microelectronics. It is sustained only by intensive research and development in the face of perpetual technology challenges always looming on the horizon.

Goals and benchmarks for scaling are established and monitored in the International Technology Roadmap for Semiconductors (ITRS), a public document prepared every other

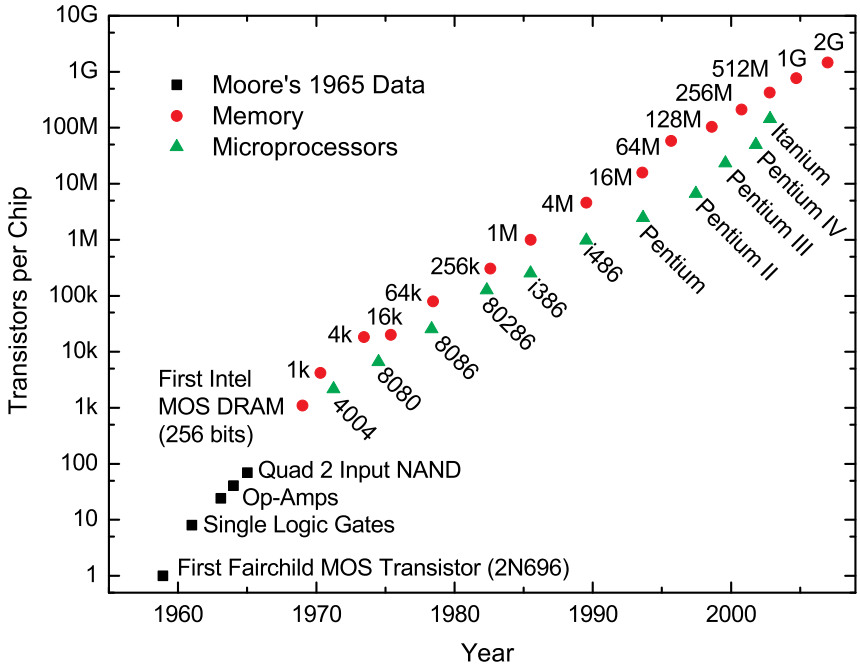

Figure 1.1. Transistor counts for integrated circuits showing the historical accuracy of Gordon Moore's prediction of exponentially increasing integrated circuit complexity.

year by a consortium representing the global semiconductor industry [2]. The roadmap is intended "to provide a reference of requirements, potential solutions, and their timing for the semiconductor industry" over a fifteen-year horizon. For many years, the ITRS has highlighted one threat to continued scaling in particular that must be addressed in the short term future in order to avoid slowing down the pace of Moore's Law.

The anticipated problem is often referred to as the "interconnect bottleneck." As the number of transistors in an integrated circuit increases, more and more interconnecting wires must be included in the chip to link those transistors together. Today's chips already contain well over one kilometer of wiring per square centimeter of chip area [3]. Sending information along these wires consumes significant power in resistive waste heat and introduces the majority of speed-limiting circuit delay in a modern integrated circuit. Scaling exacerbates both of these problems by decreasing the cross sectional area of each wire, proportionately increasing its electrical resistance. With further scaling the RC capacitive charging delays in the wires will increasingly dominate the overall performance of future integrated circuits.

The interconnect bottleneck has threatened Moore's Law before. In the late 1990s, integrated circuits contained aluminum wires that were surrounded by silicon oxide. As

interconnect cross sections decreased, mounting circuit delay in capacitive charging of these aluminum wires began to effect chip performance. A solution was found in a change of materials. Copper was introduced in place of aluminum, which cut the resistance of the wires nearly in half. Eventually low dielectric constant ("low-κ") doped silica infill materials were also phased in to reduce the capacitance.

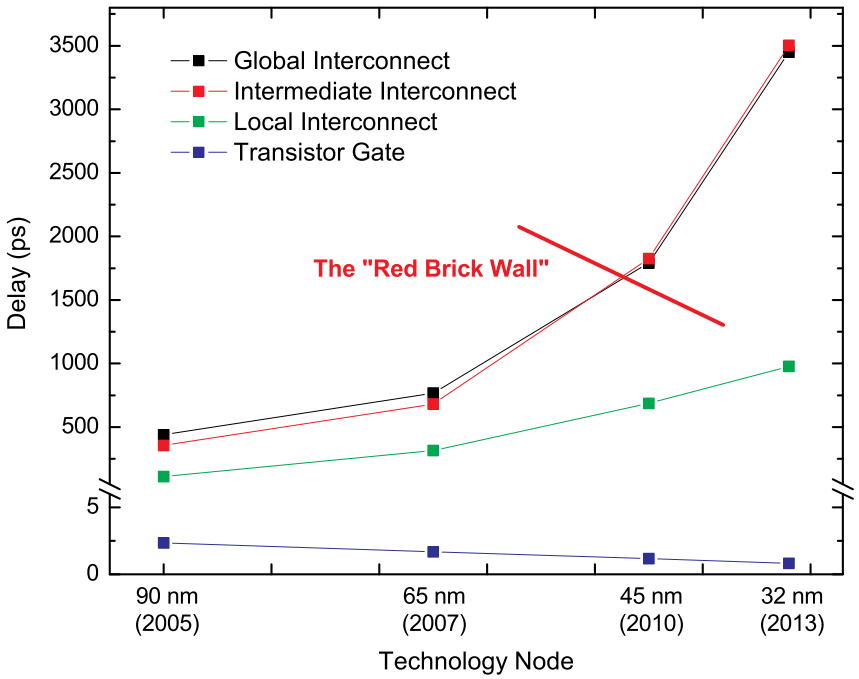

Figure 1.2. According to the ITRS, there no known manufacturable global or intermediate interconnect solutions for the 45 nm technology node. In the roadmap, such challenges are highlighted on a spreadsheet in red, forming the "red brick wall."

Incorporating these new materials into existing fabrication processes posed significant integration challenges. Copper can diffuse quickly through silicon and create short circuits in the transistors of a chip unless care is taken to avoid contact between the copper wires and the silicon substrate. Additionally, the nonexistence of any suitable gas phase etching process for copper requires additive deposition techniques to be used. The silicon industry invested heavily in research and development to find diffusion barriers and to perfect "Damascene" deposition processes relying on chemical-mechanical planarization (CMP) [4]. These technologies made copper interconnects possible and have allowed scaling to continue through the present day.

Further evolutionary progress through materials research in very low-κ dielectrics may postpone the return of the interconnect bottleneck, but a new approach to information transfer within integrated circuits will inevitably become necessary if transistors are to continue shrinking into the next decade. According to the latest update of the ITRS chapter on interconnects, traditional interconnect scaling is not expected to satisfy performance requirements after approximately 2010 (figure 1.2).

1.2 Optical Interconnects

Many expect photonics to provide the long term solution. In so-called optical interconnect schemes, the copper wires between regions of an integrated circuit would be replaced by a system of lasers, modulators, optical waveguides and photo-detectors [5–7]. The potential benefits of this approach include the virtual elimination of delay, cross talk, and power dissipation in signal propagation, although significant new challenges will be introduced in signal generation and detection.

The integration density and data rate that can be achieved using conventional electrical interconnects set very high performance requirements for any optical interconnect system to be viable. We can anticipate that optical interconnects will demand the chip-scale integration of the very best photonic technologies available today. Stable laser sources, interferometric modulators, dense wavelength division multiplexing (WDM), and low loss planar waveguides will all be necessary components of an optical interconnect system that can reach an acceptable per-wire information bandwidth-per-watt figure of merit.

These photonic technologies are now applied primarily in the long-haul telecommunications industry, where individual component cost and size do not drive the market. Data transfer rates and the cost per transmitted bit through optical fiber networks have improved dramatically in performance over the last few decades, following exponential progress curves that can compound even faster than Moore's Law. These advances underlie the infrastructure of the internet and are responsible for fundamental changes in our lives, particularly in our experience of distance around the globe. However, while millions of miles of fiber optic cable now stretch between cities and continents, the photonic components they connect are still typically packaged separately. Obviously this must change if optical networks are to be replicated in microcosm within millions of future chips.

Microphotonics refers to efforts to miniaturize the optical components used in long distance telecommunications networks so that integrated photonic circuits can become a reality. Work in this field spans many subjects, including planar waveguides and photonic crystals, integrated diode detectors, modulators, and lasers. In more recent years, research focused on the subwavelength manipulation of light via metal optics ("plasmonics" [8]) and dispersion engineered effective media ("metamaterials") has begun to explore the anticipated limits of scaling in future photonic integrated circuits. Advances in the related and often overlapping field of "nanophotonics" suggest the possibility of eventually controlling optical properties through nanoscale engineering.

Between the long-haul telecommunications industry and research in microphotonics lies a small market that will undoubtedly aid in driving the integration of on-chip optical networks: high performance supercomputing. Modern supercomputer performance is typically dominated by the quality of the interconnecting network that routes information between processor nodes. Consequently, a large body of research exists on network topology and infrastructure designed to make the most of each photonic component. This knowledge is ready to be applied to future optical interconnect networks that connect subprocessor cores within a single chip [9].

If optical interconnects become essential for continued scaling progress in silicon electronics, an enormous market will open for integrated photonic circuit technology. Eventually, unimagined new products will be made possible by the widespread availability of affordable, high-density optical systems. Considering the historical development of computing hardware from the relays and vacuum tubes of early telephone networks, it is possible that optical interconnects could someday lead to all-optical computers, perhaps including systems capable of quantum computation [10, 11].

Unfortunately, there is at present no clear path to practical on-chip optical data transfer and scalable all-photonic integrated circuits. The obstacles that currently stand in the way of optical interconnects are challenges for device physics and materials science. Breakthroughs are needed that either improve the set of materials available for microphotonic devices or obviate the need for increased materials performance through novel device designs.

1.3 Silicon Photonics

The goal of silicon photonics is to create high performance optical devices from the set of "CMOS compatible" materials used in electronic integrated circuits so that photonic components can be made using mature silicon fabrication technology. The initialism CMOS stands for "complementary metal oxide semiconductor", and refers to logic circuit designs that pair p-channel transistors with n-channel transistors to limit the quiescent currents that waste power when a circuit is not otherwise active. CMOS circuits have tremendous power efficiency advantages and are the building blocks for all microprocessors. It important to ensure that all materials used in a CMOS facility do not contaminate these fundamental components of the circuit. However, full CMOS compatibility contains an additional connotation of cost effective economic scaling. The materials and processes that are considered CMOS compatible therefore change over time as new techniques are developed that decrease integration costs or overcome contamination concerns.

Optical interconnects are an anticipated future application for silicon photonics; however we can also include several existing products under the banner of the discipline. For example, integrated photonic systems fabricated using silicon technology are essential elements of many displays, including large area liquid crystal display (LCD) monitors, widescreen televisions, and projectors that incorporate digital light processing (DLP) chips (micro-electro-mechanical systems (MEMS) devices consisting of large arrays of small tilting mirrors). However in both of these cases, light is generated externally with a fluorescent tube or a light bulb and only manipulated by the integrated silicon photonic system.

Displays incorporating luminescent components are in active development because of the cost, power efficiency, and image quality improvements that they might allow. Most of the problems encountered in this effort are related to materials issues, in either integration or stability in fabrication or operation. Ongoing research in CMOS compatible materials for active displays may solve these problems, but may not by itself drive the innovation required for silicon photonics to become useful for optical interconnects.

For displays, the relatively low performance required to exceed the acuity of the human eye limits the technology "push" to higher performance and smaller silicon photonic components. Pixels will never need to be smaller than $\sim$100 microns on a side or be able to switch faster than $\sim$100 Hz to satisfy the spatial and temporal resolution of the typical eye

(∼30 seconds of arc and ∼15 milliseconds respectively). Useful information transfer will require much faster switching speeds, and scaling requirements will demand much smaller component dimensions.

Of course, silicon itself is a CMOS compatible material that we can consider using for photonics. Many of the properties that make silicon a good choice for electronic chips are helpful in optical applications as well. It is an abundant material, with good thermal conductivity and good mechanical strength. It also has a high index of refraction and a small intrinsic absorption at infrared photon wavelengths. Silicon-based device solutions have been demonstrated for planar waveguides and for high-speed detectors. However, silicon is a poor material for making modulators or lasers, which together comprise the necessary signal transmission source in optical communication.

High performance modulators change the magnitude of the transmitted optical signal by switching between constructive and destructive interference conditions at the output terminal of the device. Typically this is accomplished by inducing a ninety degree relative phase shift in one arm of a Mach-Zehnder interferometer. This process can be faster and more efficient than changing the signal intensity by directly modulating the driving current of the source laser or by inducing attenuation through absorption.

A phase change can be quickly imposed via electro-optical effects, in which a controlling electric field changes the dielectric response of the material that the light is propagating through. A field can be created across a waveguide more quickly than a current can be established and requires much less energy to sustain. When the index of refraction varies linearly with a change in the applied electric field strength, the electro-optic effect is called the Pockels effect. If the variation is quadratic in the applied field, the effect is called the Kerr effect. Typically the Kerr effect is many orders of magnitude weaker than the Pockels effect. Unfortunately, the Pockels effect is forbidden in any crystal that has inversion symmetry, which includes silicon. Crystals with more complicated structure, such as lithium niobate, are used to make modulators for fiber optic telecommunications networks, but these materials are not considered CMOS compatible.

Silicon modulators must instead operate using weaker higher-order electro-optic effects, such as the Kerr effect, or resort to current-based switching mechanisms. Several groups have reported silicon modulators that function by the free carrier dispersion effect, in which a high density of injected charge carriers changes the effective refractive index of silicon

through a plasma interaction [12, 13]. However, the free carrier dispersion effect is relatively inefficient and such devices dissipate an unacceptable amount of power to be of practical use for intrachip optical interconnects.

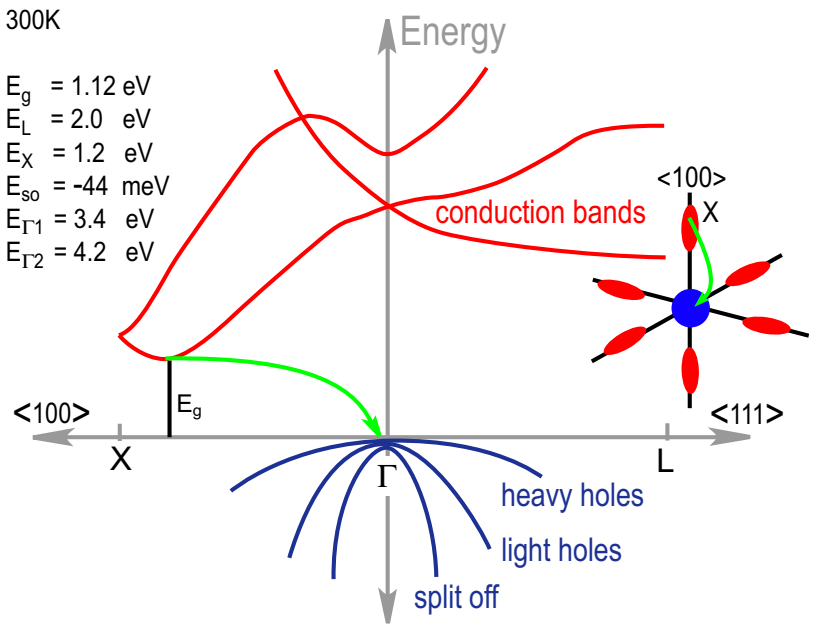

Figure 1.3. In the band structure of silicon, the lowest energy states in the conduction band are offset in momentum space from the highest-energy valence band states at the center of the Brillouin zone.

Silicon also makes a poor material for light emitting devices, including lasers, because it has an indirect band structure (figure 1.3). This means that the least energetic conduction band electrons in silicon are in motion relative to the most energetic valence band electron states. In order for silicon to absorb or emit a photon at visible frequencies, an electron must undergo a band-to-band transition between two of these states. This transition requires the simultaneous absorption or emission of a phonon (the quantum of mechanical vibration) in order to accommodate the momentum mismatch, making it much less likely to occur. Because a radiative transition is unlikely, competing nonradiative recombination channels tend to dominate the relaxation of the excited state electrons. Ultimately this makes photon emission in silicon extremely inefficient (10^{-7}–10^{-4}) unless great efforts are made to purify the material and to passivate all surfaces [14].

The recently reported "first silicon laser" [15, 16] did not rely on the emission of photons

by excited conduction band electrons. This laser instead operated by Raman scattering, in which sub-bandgap photons interact only with phonons. The crystallinity of silicon makes Raman scattering relatively strong in relation to amorphous glasses, but intense optical pumping is still required to create a population inversion of the excited virtual phonon state. Under such intense illumination, simultaneous two-photon absorption excites electrons into the conduction band, which can then attenuate the laser signal through free carrier absorption. The subsequent "first continuous silicon laser" was achieved through better management of these free carriers [17]. While these results are impressive, it is clear that Raman lasers do not have a practical future because they require optical excitation by a pump laser and have a relatively small spectral range in which gain can be achieved. The report of an all silicon laser that is electrically pumped will elicit a far more enthusiastic reception.

As is the case with modulators, materials that have superior optical properties, such as alloys of Group III and V elements, are used to make the lasers used in long-haul telecommunication networks. These materials are regrettably not CMOS compatible, primarily because of mismatched crystal lattice constants with respect to silicon. However, the list of materials that are CMOS compatible is always expanding as new methods of integration are introduced. Research in relaxed epitaxial growth techniques or flip-chip and wafer bonding technology, in which crystals with incompatible lattice constants are atomically fused together, may someday allow traditional optical materials to be used to build microphotonic modulators and lasers for silicon photonics.

This strategy is currently being pursued by start-up photonics companies such as Luxtera, as well as Intel's silicon photonics research group. Both companies have recently demonstrated electrically pumped lasers on silicon substrates that use integrated III–V materials to achieve gain [18, 19]. While these results are very encouraging, it remains to be demonstrated that flip-chip integration can be economical in a production CMOS fabrication process or useful for on-chip interconnect applications.

An alternative to developing integration methods for traditional optical materials is to attempt to exploit quantum mechanical effects to improve the optical properties of silicon or other currently CMOS compatible materials. Following this approach, nanostructured silicon has been identified for many years as a promising candidate material for silicon photonics.

1.4 Silicon Nanocrystals

The story of bright optical emission in silicon nanocrystals [20] began over fifteen years ago with the first report of photoluminescence from electrochemically etched silicon, later called porous silicon [21, 22]. Similar optical observations have since been made in nanostructured silicon materials fabricated by ion implantation [23–27], aerosol synthesis [28, 29], sputtering [30, 31], laser ablation [32], chemical vapor deposition [33, 34], and reactive evaporation of Si-rich oxides [35, 36]. The excitement generated by the possibility of using nanostructured silicon as an optical material is reflected in over 5200 publications mentioning "silicon nanocrystals" and over 9000 papers referring to "porous silicon" as of April 2007. In all of these systems, quantum mechanical effects are responsible for the enhanced photonic materials properties [37].

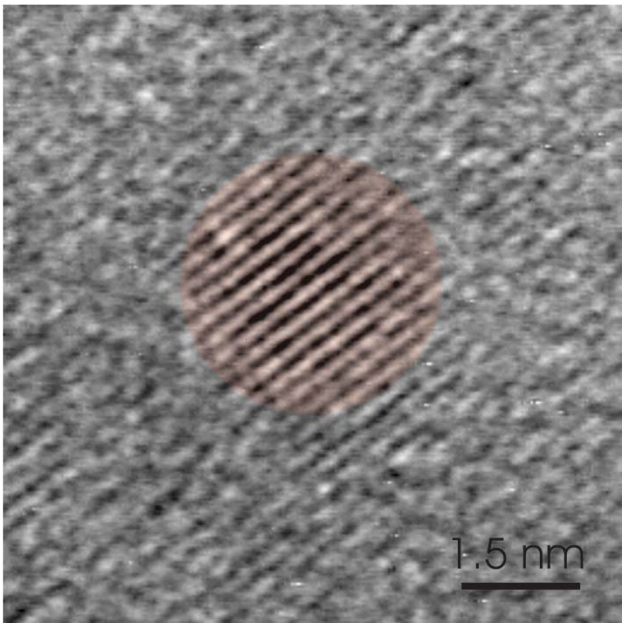

Figure 1.4. A silicon nanocrystal in SiO_2 imaged by high resolution transmission electron microscopy. The nanocrystal has been colored to guide the eye. [38]

Quantum mechanics describes the behavior of all physical systems, but conflicts with the predictions of classical physics only for systems that we can study at the length scale of the de Broglie wavelength. For electrons this corresponds to sizes on the order of nanometers, a regime that we can access experimentally and engineer to create useful devices that take advantage of quantum mechanical phenomena. Examples include quantum well lasers and

heterojunction bipolar transistors (HBTs), nanowires, and semiconductor quantum dots, which include silicon nanocrystals. In these quantum mechanical systems, the potential experienced by electrons is characterized by confinement in one, two, or three dimensions, respectively.

Qualitatively the effect of confinement in a quantum mechanical system can be understood by considering the simple "particle in a box" problem, in which we solve for the wavefunctions (eigenstates) and energies (eigenvalues) of an infinite potential well using Schrödinger's wave equation. In order to satisfy boundary conditions, we find that the characteristic ground state energy scales inversely with the square of the width of the confining potential well. At high energies (large quantum numbers), there is essentially a continuum of adjacent energy states available in the well, while at low energies, the states are disperse. Although momentum is no longer a valid quantum number, we can construct an equivalent density of electron states for particles inside the well and contrast to the parabolic density of states found for free particles.

This simple model already captures the essential physics of quantum dots. Confinement raises the energy of the ground state, tends to create a discrete density of states at low energies, and introduces uncertainty into the momentum of the particle. The last of these effects can also be understood by considering only the uncertainty principle, to the extent that the potential well localizes the particle in a small volume.

We can improve our approximation of a quantum dot by considering the particles of interest, excitons, in a three-dimensional, finite, spherical confinement potential representing the insulating matrix around the semiconductor nanocrystal. Excitons are electron-hole composite states that are coupled together by Coulomb attraction. The mathematics used to describe an exciton is identical to our model for the hydrogen atom. We can therefore predict from first principles a Bohr radius for the ground state of the exciton corresponding to the critical length scale for confinement effects. In terms of the electron and the hole that comprise the exciton, the Bohr radius can be thought of as the typical separation distance. In silicon, the exciton Bohr radius is $\sim$4.9 nm, a fairly small number among semiconductor quantum dots because of the relatively large effective mass of the charge carriers in silicon. This tells us that we can expect to observe quantum confinement effects in silicon nanocrystals that are smaller than approximately 5 nm in diameter.

As anticipated by our consideration of the particle in a box problem, the energy of

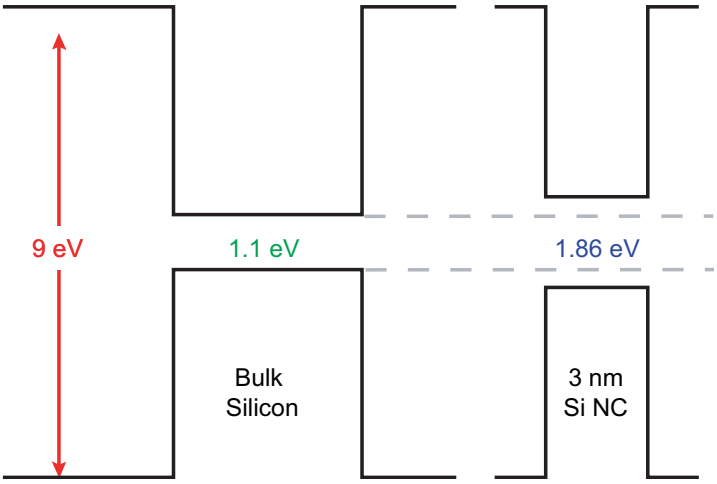

Figure 1.5. Quantum confinement increases the effective bandgap of a silicon nanocrystal with a diameter that is smaller than the exciton Bohr radius (∼5 nm). The bandgaps of bulk silicon and SiO_2 are drawn to scale.

the ground state exciton increases with increasing confinement. A simple analytic model predicts that this size-dependent effective bandgap varies according to:

$$E_{g,NC} = E_{g,bulk} - \frac{1.8q_e^2}{\epsilon R} + \frac{\hbar^2\pi^2}{2\mu R^2} + O\left(\frac{1}{R^3}\right)$$

where $E_{g,NC}$ is the lowest eigenvalue for the confined exciton, $E_{g,bulk}$ is the bulk material bandgap, μ is the reduced mass of the electron-hole pair, and R is the radius of the nanocrystal [39, 40]. The factor 1.8 that appears in Coulomb attraction term accounts for the overlap of electron and hole wavefunctions. Figure 1.5 shows the scale of the change in effective bandgap for a nanocrystal that is ∼3 nm in diameter. More rigorous treatments that include exchange and spin-orbit terms show essentially the same trend [41, 42], and the aggregated experimental data for silicon is well fit by the model for nanocrystals with diameters larger than ∼3 nm [41–51]. Poor agreement is typically found for smaller silicon nanocrystals and is commonly attributed to silicon oxygen double bond defect states at the surface of the nanocrystal that can capture and localize the exciton [52–54]. Figure 1.6 shows the size-dependent silicon nanocrystal bandgap plotted according to a phenomenological model given by Ledoux [55], along with the surface defect related sub-bandgap energy levels for one and multiple silicon-oxygen double bonds [53]. It is worth noting that native surface oxides on silicon are typically ∼2 nm thick. Therefore a silicon nanocrystal is essentially

"all surface" and might be expected to be very sensitive to surface chemistry. Theoretical and experimental evidence for these oxygen bond trap states has generally convinced the silicon nanocrystal research community that blue emission from quantum confined excitons is unlikely to be achieved from nanocrystals embedded in silicon oxide environments. This is one reason why attention has shifted more recently to silicon nanocrystals in silicon nitride materials [56, 57].

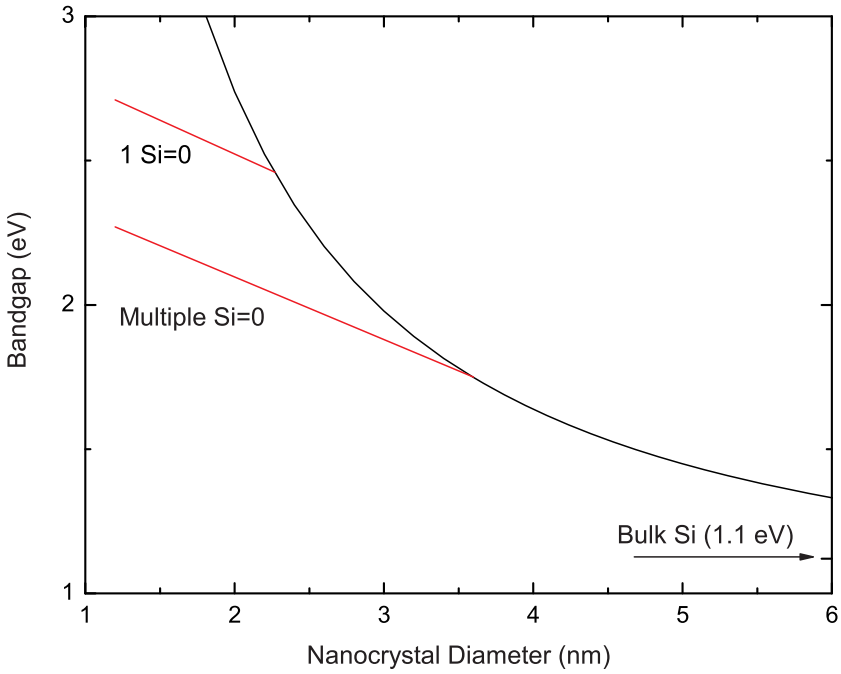

Figure 1.6. The bandgap of a silicon nanocrystal increases with decreasing nanocrystal size due to quantum confinement, but surface defect states related to oxygen bonds dominate at small diameters.

In addition to causing the blue shift of the silicon band edge emission into the near infrared or red spectral range, quantum confinement in silicon nanocrystals results in orders of magnitude brighter emission than is observed from bulk silicon. The brighter emission must be explained by some combination of enhancement in the absorption cross section and radiative recombination rate and decrease in the rate of nonradiative recombination. Experiments suggest that the absorption cross section in silicon nanocrystals shows little or no enhancement over bulk silicon on a per-atom basis. Of the remaining two factors, most of the improvement in radiative recombination efficiency comes from a dramatic decrease

in the nonradiative recombination rate.

Nonradiative exciton recombination in bulk silicon is typically dominated by Shockley-Hall-Read recombination at mid gap defect states corresponding to defects and impurities in the crystal [58, 59]. In nanocrystals that are small enough to show quantum confinement effects, such defects are thermodynamically unfavorable and tend to grow out of the quantum dot. Two other recombination mechanisms that contribute to the inefficiency of light emission in bulk silicon are recombination at surface defects and Auger recombination, in which the energy of the exciton is transferred to a third charge carrier. Both of these mechanisms can be worse in silicon nanocrystals than in bulk silicon, to the extent that a single surface defect or a single extra free charge carrier can effectively switch a silicon nanocrystal into a "dark" state, in which radiative recombination is very unlikely [60]. The enhanced sensitivity to surface recombination can be understood by noting the high surface-to-volume ratio, while the rapid Auger recombination rate in charged nanocrystals results from the large effective carrier concentration that a single carrier represents in the small nanocrystal volume. In many experiments we have only indirect access to this population of "dark" nanocrystals via internanocrystal energy transfer processes which makes the active fraction of silicon nanocrystals in any given ensemble difficult to determine.

There are two factors that contribute to improvement in the radiative recombination rate in silicon nanocrystals. The first can be understood in the context of Fermi's Golden Rule for quantum mechanical transitions, which can be derived using time dependent perturbation theory. In the formalism of Fermi's Golden Rule, the rate of an optical dipole transition is proportional to the magnitude of an off-diagonal matrix element calculated by evaluating an overlap integral that connects the electron and hole wavefunctions together through the dipole operator. Because the nanocrystal forms a potential well that confines the electron and the hole spatially, these wavefunctions overlap more in position space and the matrix element, or oscillator strength, for the transition increases [61].

At the same time, the uncertainty in momentum space that confinement introduces relaxes the momentum conservation rule and allows a greater proportion of the phonon density of states to assist in the indirect band-to-band transition [62]. This effect is thought to be insufficient to make the bandgap of silicon nanocrystals direct but the optical transitions in small nanocrystals might possibly be described as quasidirect. Reports claiming direct gap transitions in silicon nanocrystals at blue emission wavelengths on the basis of

decay rate measurements are likely to correspond to misattributed radiative emission from oxide defect centers or to fast nonradiative recombination [63–65]. Results describing the radiative rate of silicon nanocrystals as a function of decreasing nanocrystal diameter would be difficult to interpret because of internanocrystal energy exchange processes and the unknown role of surface defect states, both of which become more increasingly prevalent as the nanocrystals becomes smaller. A comprehensive and quantitative understanding of size dependent trends for the exciton oscillator strength in silicon nanocrystals remains an open experiment in the field.

1.5 Applications for Silicon Nanocrystals

Despite the advantages that nanostructured silicon offers in comparison to bulk silicon, it is still a relatively poor optical material in comparison to direct gap III–V semiconductors. The radiative rate, which ultimately limits the optical power that can be radiated by a volume of material, is perhaps one or two orders of magnitude faster than bulk silicon at ∼10 kHz. However it is four orders of magnitude slower than the ∼1 GHz emission rates found in materials such as GaAs. While the radiative recombination efficiency is high, the insulating matrix that surrounds and defines the quantum dot complicates the electrical injection of carriers. The emission wavelengths are always blue shifted by confinement with respect to the bulk silicon bandgap at 1.1 μm and can therefore be absorbed by bulk silicon. The emission is also far from the 1.3 μm and 1.5 μm telecommunications spectral windows, in which silica fibers have a transmission maximum, making silicon nanocrystals less attractive for data transfer applications, including optical interconnects.

While gain has been demonstrated in silicon nanocrystals, it seems to require a very high concentration of excitons in each nanocrystal to manifest [66–69]. This can be understood in terms of competition between Auger recombination and stimulated emission, which is proportional to the density of the excited state population. All observations of gain have been made under intense pulsed laser excitation. While a silicon nanocrystal laser may someday be demonstrated in the laboratory following this approach, it seems unlikely that a practical electrically pumped silicon nanocrystal laser will be achieved.

In display applications, the blue shifted emission of silicon quantum dots is an advantage. Red and orange emission is fairly easy to attain in nanocrystals embedded in silicon oxide,

but blue and green luminescence is frustrated by the aforementioned oxygen double bond surface trap states. Silicon nitride based nanocrystalline systems may be able to overcome this limitation and provide all three primary additive colors [57]. However, concerns about the achievable brightness in a silicon nanocrystal based display remain because luminosity in the saturation regime is proportional to radiative rate, and the radiative rate of silicon nanocrystals is relatively low (∼1–10 kHz).

The slow radiative emission rate of silicon nanocrystals might be enhanced by engineering the local density of optical states at the site of the silicon nanocrystal. A four-fold increase in the radiative rate has been experimentally demonstrated through resonant coupling of a silicon nanocrystal to the local field of a surface plasmon mode near a metal nanoparticle [70]. Finite difference simulations suggest that this approach could enhance the emission rate by several orders of magnitude in an optimized geometry. If this can be accomplished in practice, silicon nanocrystals could become attractive for luminescent displays.

However, practical devices must be electrically pumped. Traditional light emitting diodes (LEDs) work by injecting minority charge carriers into complementarily doped regions across the depletion width of a semiconductor *pn*–junction in forward bias. The minority carriers form excitons with majority carriers and can recombine to emit light. This process requires a current to flow through the device which consumes energy in Joule heating in proportion to the resistance of the diode. Because silicon nanocrystals must be embedded in an insulating matrix, an LED made out of nanocrystal doped material would have a low conductivity and resistive heating would limit the electroluminescence power efficiency. Inadvertently doping the silicon nanocrystals could also be problematic. A single donor or acceptor in a nanocrystal creates a degenerate free carrier concentration that turns on strong nonradiative Auger quenching of any injected excitons [71–73].

Instead, electrically pumped light emitting devices have been made with intrinsic silicon nanocrystals. These designs rely on impact ionization to create excitons. The process is the inverse of Auger recombination: an injected carrier with excess thermal energy relaxes to the band minimum by promoting an electron from the valence band into the conduction band of the quantum dot. Impact ionization requires relatively large voltages in order to create the electric fields that induce carriers to tunnel through the insulating barrier to the nanocrystal. Excitation is more efficient with highly energetic “hot” carriers, but this process can damage

the quality of the insulating matrix over time and reduce device longevity [74]. Some reports claim that impact ionization can be achieved without introducing "hot" carriers. In the best reported devices, the internal electroluminescence efficiency has not yet exceeded 1%. An alternative approach to carrier injection may be necessary to make further progress.

While silicon nanocrystals alone cannot emit light in the infrared telecom bands, they can be coupled to the emission of erbium ions to create a promising hybrid optical material [75–80]. When incorporated in silicon oxide, Er^{3+} ions exhibit a weakly allowed atomic transmission at $\sim$1.5 μm that is well aligned with the transmission maxima in optical fiber. For this reason erbium doped fiber amplifiers are commonly used in long distance telecommunications to restore the intensity of optical signals. Because the transition is an atomic dipole, the cross section for the optical excitation of an erbium ion is very small ($\sim 10^{-21}$ cm^2) and further requires that the exciting wavelength be resonant with another atomic transition of the ion. In contrast, the excitation cross section for silicon nanocrystals is nearly five orders of magnitude larger and nanocrystals can be excited by photons of any energy above the confined bandgap. Because the radiative rate of silicon nanocrystals is fairly low, nonradiative near field energy transfer to erbium ions placed in close proximity to the nanocrystal can be the dominant recombination pathway for excitons. In this way, silicon nanocrystals have been shown to be effective sensitizers for erbium ions in optically pumped waveguide amplifiers.

1.6 Outline of This Thesis

This thesis presents experimental work developing silicon nanocrystals as an optical material for silicon photonics. The chapters are organized as follows:

In chapter 2, we discuss the design, fabrication, and characterization of silicon nanocrystal layers made by ion implantation. In collaboration with Intel Corporation, we show that dense silicon nanocrystal layers can be created in a production silicon microprocessor fab on 300 mm substrates using established ion implantation and thermal annealing processes. From photoluminescence and ellipsometry measurements we are able to correlate distributions of nanocrystals to calculated implantation profiles and simulations of nanocrystal formation. Finally we measure the average internal quantum efficiency of silicon nanocrystals in dense ensembles using an intensity invariant technique that relies on the

proportionality of radiative recombination to the local density of optical states.

Chapter 3 describes test devices that allow simultaneous optical and electrical access to silicon nanocrystals. These devices are silicon nanocrystal floating gate transistors designed to facilitate experiments correlating the optical properties of silicon nanocrystals to the average charge state of the nanocrystal ensemble. We present design and fabrication details and structural characterization. It is shown that these devices can function as all-optical memory elements at room temperature. Charge can be stored on the nanocrystals that comprise the floating gate of the transistor by electrical injection under a gate bias. In charged silicon nanocrystals, photoexcited excitons preferentially decay through Auger recombination, allowing the charge state of the memory to be read optically in the intensity of photoluminescence. We further show that internal photoemission can be used to optically erase the memory. We demonstrate the switching speed of such an optical memory is limited by the radiative rate of the silicon nanocrystals.

Chapter 4 presents a novel electroluminescence mechanism called *field effect electroluminescence*. We demonstrate that excitons can be created in silicon nanocrystals by the sequential injection of complementary charge carriers from a semiconductor channel. In contrast to previously reported light emitting diodes, a field-effect light emitting device (FELED) is excited by an alternating gate voltage. Electroluminescence is observed at transitions in gate bias. This approach offers a new conceptual paradigm for electrical excitation in quantum dots.

Chapter 5 discusses initial work on hybrid field-effect light emitting devices designed to operate at optical telecommunications wavelengths. We first discuss photoluminescence from erbium ions that are coupled to silicon nanocrystals by energy transfer processes and show that silicon nanocrystal sensitized erbium can be fabricated by the coimplantation of erbium and silicon. We then describe experiments with FELED samples that are additionally implanted with erbium ions. We also fabricate FELEDs designed to allow near field coupling between silicon nanocrystals and solution fabricated lead selenide (PbSe) quantum dots using focused ion beam milling.

Finally we discuss future directions for research in field-effect electroluminescence and present a brief outlook for silicon nanocrystals in silicon photonics.

Chapter 2

Silicon Nanocrystals

2.1 Introduction

In this chapter, we discuss the design, fabrication, and characterization of the silicon nanocrystals studied throughout this thesis. In collaboration with Intel, we show that layers containing silicon nanocrystals can be formed in a production silicon fab on 300 mm substrates via ion implantation and thermal annealing. This unequivocally establishes the CMOS compatibility of silicon nanocrystal layers in front end (high temperature) semiconductor processing. From photoluminescence and ellipsometry measurements we are able to correlate distributions of nanocrystals to simulated implantation profiles. Finally we measure the average internal quantum efficiency of silicon nanocrystals in dense ensembles by observing changes in the photoluminescence decay rate with variation in the local density of optical states.

2.2 Fabrication via Ion Implantation

Silicon nanocrystals can be fabricated through a variety of techniques including ion implantation [23–27], aerosol synthesis [28, 29], ion beam co-sputtering [30, 31], chemical vapor deposition [33, 34], and reactive evaporation of silicon-rich oxides [35, 36]. All of these methods rely on the low mobility of silicon in silicon dioxide [33] and the equilibrium phase separation of Si from SiO_2 in silicon-rich oxide layers at high temperatures [81].

Among these processes, we use ion implantation and thermal annealing to create silicon nanocrystals for our experiments and devices. This technique was selected primarily for compatibility with CMOS processing; ion implantation is already commonly used in silicon microelectronics to create doped regions in circuits. In the ion implantation procedure, ions are extracted from a plasma and accelerated by an electric field to the sample. The ions

impact with sufficient energy to travel some distance into the sample before they come to rest. The total dose of implanted ions is controlled by monitoring the integrated current as the ion beam is rastered over the sample. In this way an implanted layer can be created with good uniformity across large substrates. Ion implantation is available as a contract service from several vendors, including Kroko Implant Services in Tustin, California, and Implant Sciences Corporation in Wakefield, Massachusetts. We have also had some samples implanted at Intel Corporation's D1-C and RP-1 fab lines in Hillsboro, Oregon, during the course of our collaboration.

Sample preparation begins with the thermal oxidation of a silicon substrate. The resulting oxide layer is then implanted with $^{28}Si^{+}$ ions to create a silicon-rich zone within the oxide. The implantation dose is typically designed to increase the peak atomic percent excess silicon concentration by 5% to 25% at the intended position for the nanocrystal layer (corresponding to peak stoichiometries of $Si_{1.15-2}O_2$). High implantation doses can be correlated to larger nanocrystals, but several other factors are important, including oxidation effects, substrate proximity, and annealing conditions [82–84]. When implanting silicon into thin oxide films, losses due to sputtering during the implantation process should also be considered.

The distribution of the implanted silicon ions can be calculated using the SRIM code developed by Ziegler [85]. This code uses universal stopping potentials that can predict the implantation distribution with an average accuracy of about 5% [86]. As shown in figure 2.1, there is a strong correlation between the implantation depth and the width, or "straggle", of the ion distribution. In order to have a well defined silicon nanocrystal layer for device applications, it is desirable to implant silicon ions at low energy to achieve a narrow implantation zone [87]. However, the ion beam current that can be extracted from the source plasma decreases rapidly at low ion beam energies, proportionately increasing the implantation time and the cost of implanting the desired stoichiometric excess of silicon in the oxide layer. Most of the samples prepared for this thesis were implanted with 5 keV silicon ions, an energy selected to balance implantation depth, straggle in the depth distribution, and sample preparation cost. Figure 2.2 shows the implanted distribution of 5 keV Si ions as predicted by Monte-Carlo simulation with the SRIM code. A 20% peak atomic percentage excess corresponding to a peak stoichiometry of $Si_{1.75}O_2$ can be reached with an implantation fluence of 1.27×10^{16} ions/cm^2. The sputtering rate is difficult to predict

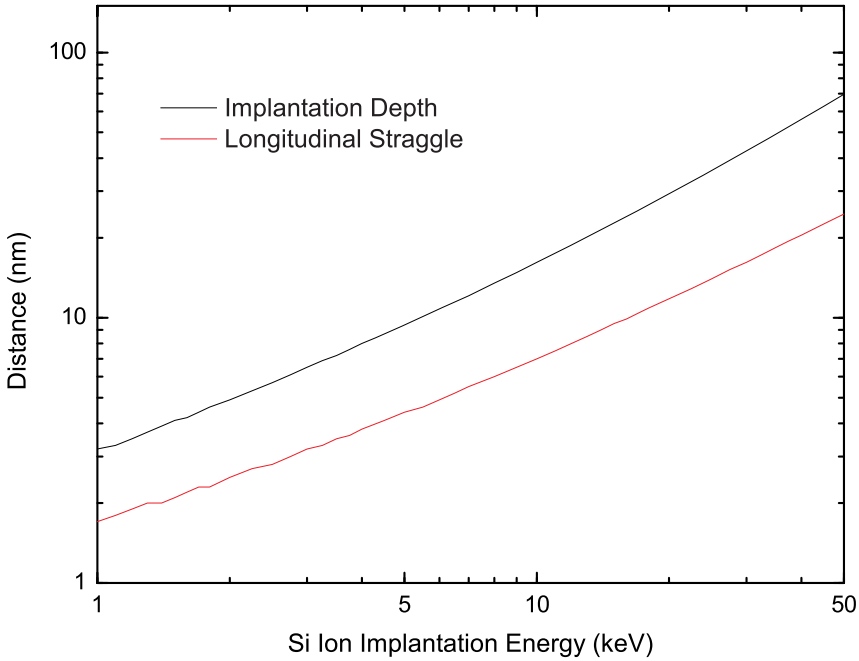

Figure 2.1. The calculated implantation range of Si ions into SiO_2 as a function of impact energy.

accurately, but may be expected to increase the effective dose by up to a few percent atomic excess by preferentially removing oxygen from the SiO_2 layer.

After the silicon-rich layer is formed, the samples are annealed at high temperature to phase separate silicon from the supersaturated solid solution. The redistribution rate of the silicon depends exponentially on the annealing temperature and linearly on the annealing time. This can provide another limited method for controlling the size distribution of the silicon nanocrystals that precipitate. Annealing for longer times at higher temperatures tends to result in larger nanocrystals. This is usually attributed to the Ostwald ripening mechanism, in which a constant probability of escaping from an interface favors the growth of larger nanocrystals at the expense of small conglomerates [88]. Typically silicon nanocrystal samples are annealed between 900 °C and 1100 °C for 10 to 30 minutes in a tube furnace. It is important to control the ambient oxygen partial pressure during the annealing step in order to avoid consuming the implanted silicon in oxide growth, but a slight background oxygen pressure can be used to suppress preferential oxygen desorption [89]. Samples fabricated at Intel were annealed in a Rapid Thermal Annealing (RTA) furnace, which uses intense illumination to heat the surface layer of a sample rapidly. This tool is

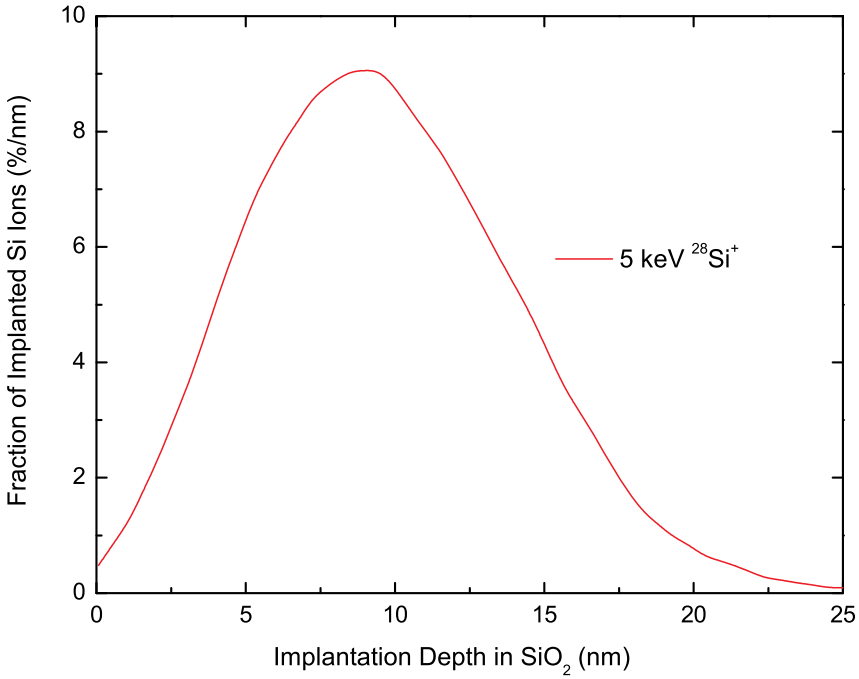

Figure 2.2. The simulated depth distribution of Si ions implanted into SiO_2 at 5 keV.

typically used in a silicon fab to activate dopants by short duration "spike" annealing treatments. Because of tool safety concerns, our samples could be annealed for only 5 minutes at a temperature of 1080 °C in the RTA. However, we found that this short annealing time was sufficient to form a dense layer of optically active silicon nanocrystals. It is apparent that ion implantation can be used to create nanocrystals across a wide processing window. Unfortunately the robustness of the fabrication method also tends to limit the changes that processing conditions can make in the nanocrystal size distribution or the density of the nanocrystals. While the ion implantation fabrication method has proven sufficient for our experiments and proof of concept devices, it is likely that improvements could be made using an alternative fabrication method that offers more precise control over the nanocrystal geometry.

When the implanted Si ions enter the oxide layer, they impart momentum to atoms in the silica matrix. These atoms recoil and are reincorporated at new locations in the SiO_2 matrix. This mixing process results in significant damage in the form of dangling bonds and vacancies within the amorphous oxide matrix in the vicinity of the silicon nanocrystals. These defects can be observed in photoluminescence measurements [90] and can reduce the internal radiative quantum efficiency of the silicon nanocrystals by introducing non-

radiative recombination relaxation pathways. Some of the damage is repaired during the high temperature nanocrystal formation anneal, but it is common to additionally anneal silicon nanocrystal samples in a hydrogen-rich atmosphere in an attempt to passivate any remaining dangling bonds. The photoluminescence intensity typically increases by a factor between 2 and 10 following hydrogen passivation. Many of our samples are annealed in a "forming gas" ambient of 10% H_2:N_2 at 450 °C for ~30 minutes for this purpose.

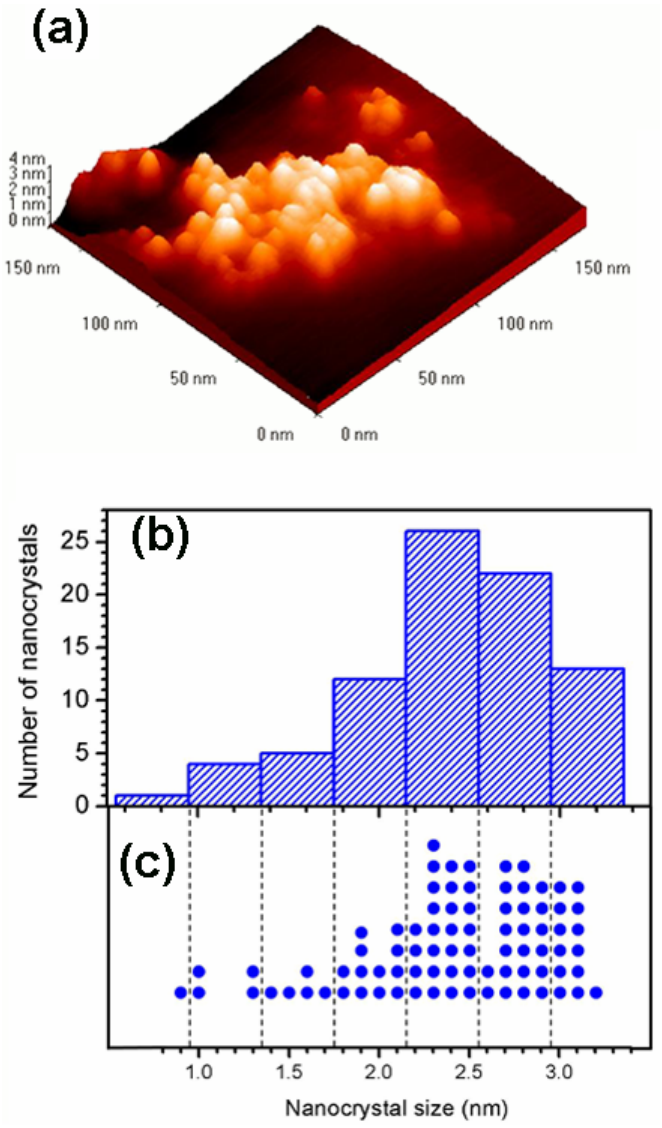

Figure 2.3. The size distribution of Si nanocrystals fabricated by our fully CMOS compatible ion implantation process is determined using vacuum noncontact AFM measurements (a). (b) and (c) are the histogram and distribution, respectively, of Si nanocrystal sizes based on the measurements of the 83 Si nanocrystals in (a) [95].

The structural characterization of silicon nanocrystal distributions fabricated by ion implantation can be accomplished using transmission electron microscopy (TEM) [91–94], but the small atomic number difference between silicon and oxygen atoms makes such measurements difficult without the use of an energy filter to enhance the contrast. Tao Feng has recently demonstrated an alternative approach to structural characterization in his thesis work [95, 96] using a combination of scanning probe measurements and reflection high energy electron diffraction (RHEED). His experiments were conducted using the same sample set we use in the optoelectronic experiments described in this thesis, allowing us to make direct use of his results. These samples were fabricated during our collaboration with Intel on 300 mm substrates by implantation with 5 keV Si^+ ions to a total fluence of 1.27×10^{16} cm^{-2} and were annealed in an RTA furnace at 1080 °C for 5 minutes in an atmosphere containing 2% oxygen. His measurements show that the nanocrystals fabricated by this procedure are crystalline and that they are distributed in an approximate monolayer within the oxide layer. He estimates the areal density of nanocrystals in the samples to be $\sim 4 \times 10^{12}$ cm^{-2}. Figure 2.3 is reproduced from Feng's thesis, and shows a measurement of the distribution of silicon nanocrystal diameters that suggests a mean diameter of ∼2.5 nm. This size is somewhat too small to correspond to the photoluminescence spectra we measure, and probably implies a decrease in diameter during the etching procedure used to separate the nanocrystals from the oxide matrix prior to the vacuum atomic force microscopy measurement. A distribution of nanocrystal diameters centered at 2.5 nm would imply that ∼26% of the implanted silicon contributes to nanocrystal formation. If the etching procedure has reduced the average diameter from ∼4 nm, as may be more consistent with the range of observed photoluminescence wavelengths, ∼82% of the implanted silicon contributes to nanocrystal formation. The remainder of the implanted silicon could be incorporated into the substrate during the nanocrystal formation process, adding ∼1 nm of silicon to the interface. Alternatively, the implanted silicon could be incorporated in the oxide or present in agglomerates that are too small to observe using vacuum AFM.

2.3 Photoluminescence Properties

The spectral photoluminescence properties of silicon nanocrystals have been extensively studied for many years and are generally well understood [27, 52, 97–111]. The photolu-

minescence spectrum of a sample fabricated at Intel during our collaboration is shown in figure 2.4. This spectrum is entirely consistent with previously reported silicon nanocrystal photoluminescence results. It is now well established that the characteristic near-infrared photoluminescence, typically observed in the range from ∼650 nm to ∼950 nm, originates from the band-to-band recombination of quantum confined excitons [52]. Interface states involving oxygen bonds are thought to play an important role in smaller nanocrystals, which emit photons at lower energies than predicted by theory [112]. Reports of silicon nanocrystal photoluminescence at green or blue wavelengths in oxide matrices tend to be met with skepticism, and are commonly assumed to be misinterpretations of defect luminescence within the oxide matrix [24]. Within the near-infrared emission band, the emission wavelength can be tuned by controlling the diameter of the silicon nanocrystals [104]. While the strength of band-to-band radiative recombination increases with decreasing nanocrystal size over this spectral range, a transition to a direct gap band structure has not been observed. It has been proposed that the oxygen bond related interface states dominate the recombination for small nanocrystals that might otherwise show direct gap behavior [52]. For this reason, silicon nanocrystals embedded in nonoxide matrices such as Si_3N_4 have recently attracted attention [57]. However, the radiative quantum efficiency of silicon nanocrystals embedded in silicon nitride may be lower than the quantum efficiency of nanocrystals in SiO_2.

The absorption characteristics of silicon nanocrystals can be measured directly by transmission measurements, but these experiments may be effected by absorption that is essentially unrelated to the excitation of quantum confined excitons in silicon nanocrystals. A preferred approach is to perform photoluminescence excitation (PLE) experiments, in which the emission spectrum is monitored as the excitation wavelength is changed. These measurements primarily show that the average absorption in silicon nanocrystal ensembles closely resembles absorption in bulk silicon (i.e., it is essentially featureless and generally increases into the UV) [80]. This is perhaps unsurprising as typical ∼3–4 nm diameter silicon nanocrystals contain order 10^3 silicon atoms and likely have a continuum of conduction band states available to absorb light at UV wavelengths. Electron energy loss spectroscopy (EELS) measurements also suggest that the conduction band is bulk-like in silicon nanocrystals. [113]

Despite being bright in relation to bulk silicon, single nanocrystals are still feeble light emitters (<300 fW) and so the vast majority of reported experiments have been studies of

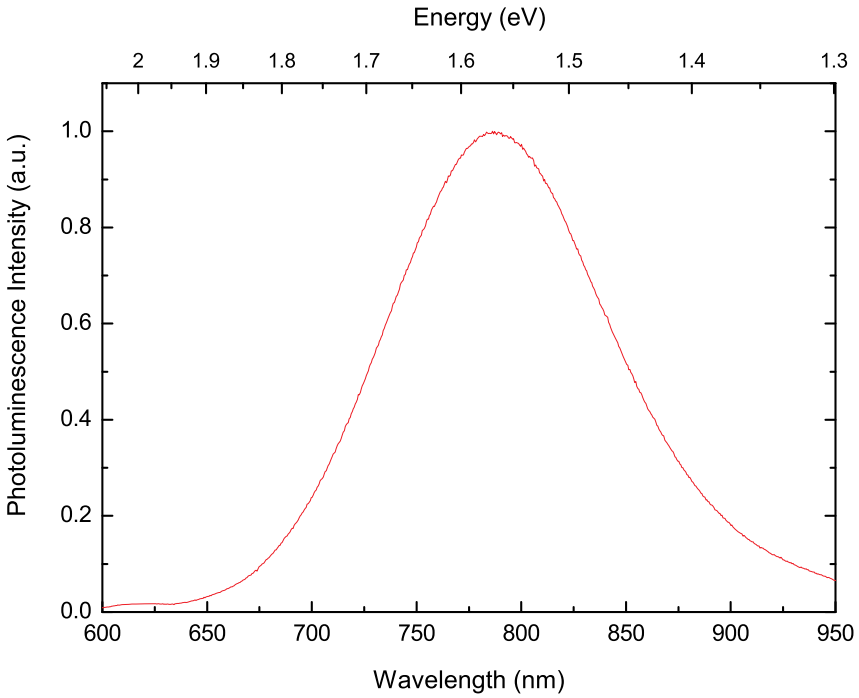

Figure 2.4. A photoluminescence spectrum for silicon nanocrystals fabricated during our collaboration with Intel Corporation. The nanocrystals are excited by ∼50 W/cm^2 pump illumination at 457.9 nm.

large ensembles of nanocrystals. Ensembles of nanocrystals are complicated optical systems that can exhibit different photoluminescence properties than isolated nanocrystals. For example, ensemble photoluminescence spectra are usually quite broad as a consequence of nanocrystal size inhomogeneity while single nanocrystal measurements made at low temperature show narrow (∼2–20 meV) homogeneous spectra [114]. The single nanocrystal measurements tend to vary widely from nanocrystal to nanocrystal, suggesting that photoluminescence is sensitive to small changes in nanocrystal composition or environment that are averaged out in ensemble measurements. These experiments also provide evidence for the excitation of complicated phonon modes that suggest that the shape of a nanocrystal may be important in addition to the size. Single nanocrystal photoluminescence measurements made at room temperature show that the homogeneous spectra broaden considerably to ∼120–150 meV [115]. To our knowledge, no PLE or recombination scale time-resolved photoluminescence experiments on single nanocrystals have yet been reported.

Other known photoluminescence properties of interest for silicon nanocrystals in silicon

oxide include the optical excitation cross section ($\sim 6 \times 10^{16}$ cm^2 at 488 nm) [80] and the single-triplet exchange energy gap for excitons ($\sim$10 meV) [116]. The exchange splitting explains the temperature dependence of silicon nanocrystal photoluminescence intensity in terms of a slow recombination rate for the parity forbidden triplet-to-ground state transitions ($\sim$0.1–0.3% of the singlet-to-ground transition rate) and the probability that the exciton will be found in the more optically active singlet state in thermal equilibrium.

2.4 Optical Characterization of Depth Distribution

The simulated ion implantation profile shown in figure 2.2 gives a coarse indication of the postanneal location of the silicon nanocrystal layer. In order to study the details of the nanocrystal formation process and to better understand the layer geometry in view of device applications, we examined the differential photoluminescence of the implanted oxide. This project was inspired by a paper of Brongersma et al., [117] which provides a detailed report of the silicon nanocrystal depth distribution for samples formed by ion implantation at 35 keV (projected range 50 nm). This previous work used a combination of transmission electron microscopy (TEM), Rutherford backscattering spectroscopy (RBS), and photoluminescence measurements to show that silicon nanocrystals are found only in the region of the implantation. Larger nanocrystals are primarily located at the center of the implanted profile, where the initial concentration of silicon is highest, and smaller nanocrystals appear to be more prevalent in the shoulders of the implanted ion profile.

Our samples are approximately an order of magnitude thinner than those studied by Brongersma ($\sim$15 nm vs. 110 nm) and therefore the depth resolution that we require is much higher. The best resolution that can be achieved using RBS measurements ($\sim$10 nm) is not sufficient. It is possible to examine low implantation energy silicon nanocrystal depth distributions through careful TEM measurements [84]. However, our photoluminescence-based technique directly measures the distribution of optically active nanocrystals, which may differ from the depth distribution identified in TEM. We estimate that our depth characterization technique is sensitive to changes in the optically active nanocrystal population at the level of $\sim$3 nm, which is approximately one typical nanocrystal diameter.

Optical characterization of the spatial distribution is accomplished by destructively etching away the sample while monitoring the photoluminescence spectrum. A 20:1 aqueous

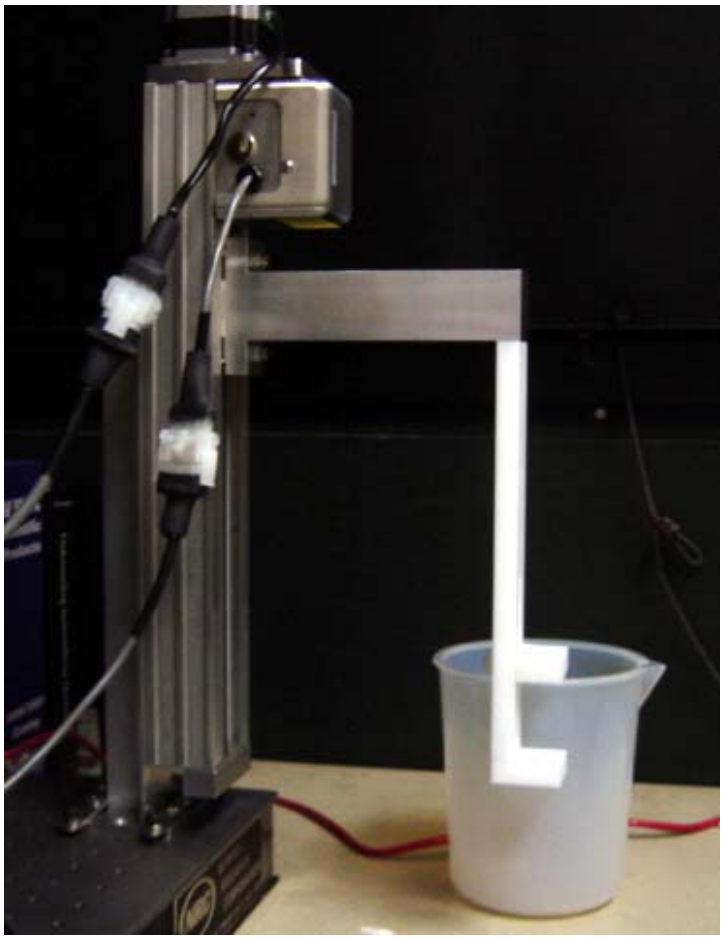

Figure 2.5. The custom-built dipping apparatus used to etch gradient profiles in oxide samples.

dilution of 48% hydrofluoric acid etches silicon dioxide at a rate of $\sim$2.5 Å s^{-1} [118]. This rate is slow enough to allow the immersion time to be used to control the removal of the oxide layer containing the silicon nanocrystals. After etching in the HF solution, spectroscopic ellipsometry measurements can be used to determine the remaining oxide thickness. Rather than measure one sample in many incremental cycles (etch oxide, measure remaining oxide thickness, measure photoluminescence, repeat), we instead begin with a long and narrow sample ($\sim$1 cm $\times$ $\sim$10 cm) and etch a gradient in the oxide layer, effectively creating many samples simultaneously on the same substrate. We have designed and built a custom "dipping" apparatus for this purpose, shown in figure 2.5. The sample is held vertically by a Teflon arm that can be raised or lowered under computer control. The immersion time is controlled to etch the desired "staircase" pattern into the sample. The precision of the

etched profile is limited only by the translation speed of the stepping motor and the etch rate of the solution. It is important to ensure that the acid solution is well mixed and to consider buffering the acid when etching at fast rates in more concentrated solutions. We have also sometimes encountered a gas phase or meniscus etching effect that tends to limit the thickness gradient that can be achieved between adjacent steps.

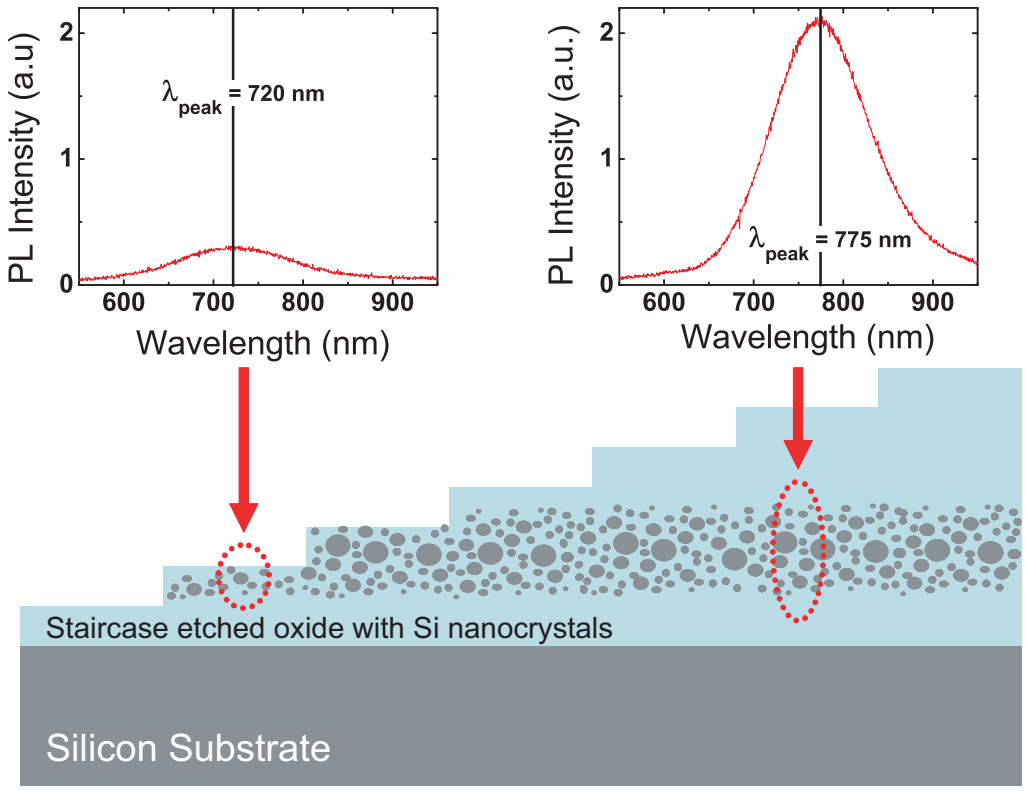

Figure 2.6. Two photoluminescence spectra collected at different positions along a staircase-etched sample. The nanocrystals are excited by ~1 W/cm^2 pump illumination at 457.9 nm.

Figure 2.6 shows a schematic diagram of our optical depth profiling experiment. The implanted distribution of silicon nanocrystals is partially removed at each etch depth along the staircase sample. At each measurement position, the photoluminescence spectrum of the remaining nanocrystals shows a shift in intensity and in peak wavelength (figure 2.6 inset). The sample was cut from a large 300 mm wafer processed at Intel. The nanocrystals were fabricated by ion implantation (5 keV; 9.5×10^{15} ions/cm^2 or 15% peak atomic excess Si) into an oxide layer that was grown to a thickness of ~15 nm. The nanocrystal formation anneal was performed in an RTA furnace at 1080 °C for 5 minutes. The calculated diffusion

length for implanted Si ions during the formation anneal is ∼1.5 nm [33]. This sample was not annealed in forming gas.

Photoluminescence data is collected while translating the sample through the focal point of a spectroscopy system, consisting of a grating spectrometer and a cryogenically cooled CCD camera. The samples are pumped with the 457.9 nm line of an argon laser at ∼1 W/cm^2. The recorded photoluminescence data are then matched to the corresponding thickness map of the sample, which is collected in a similar automated fashion by translating the sample under a spectroscopic ellipsometer. It is straightforward to collect hundreds of data points (spectra vs. oxide thickness) in a matter of minutes using this technique.

Spectroscopic ellipsometry (over the range 300 nm to 850 nm) cannot be expected to distinguish between pure SiO_2 and SiO_2 that is embedded with silicon nanocrystals in the very thin layers that we wish to study. We instead model the spectroscopic ellipsometry data by assuming that the oxide layer consists of pure SiO_2. While this model fits the ellipsometry data perfectly, we know that the nanocrystals should modify the effective index of refraction within the oxide layer. In principle the ellipsometry data could be corrected using the Maxwell-Garnet effective medium model for inclusions (i.e., silicon nanocrystals) in a host matrix of SiO_2. Unfortunately we can imagine many different mechanisms that could change the index profile or even the thickness of the implanted oxide layer. We instead show our photoluminescence data in figure 2.7 and figure 2.8 as a function of the equivalent pure SiO_2 layer thickness that we directly measure.

If we assume that all of the implanted silicon ions are incorporated in the oxide matrix in silicon inclusions (including nanocrystals), we find that the initially 15 nm oxide layer should expand by ∼2.5 nm to incorporate the extra material. The added silicon content will then increase the index of refraction enough to make the layer appear another ∼2 nm thick when applying the pure SiO_2 equivalent thickness model. In fact we see that our initially 15 nm thick oxide layer appears to be ∼20 nm thick after the nanocrystal fabrication process. However, this could easily be a coincidence. Sputtering during the ion implantation could erode the oxide layer by a few nanometers. Oxide regrowth might increase the layer thickness while decreasing the silicon content. Such regrowth might preferentially occur near the substrate, as in the "anomalous swelling" effect observed in other work after ion implantation [84], or it could occur near the surface of the oxide layer. Due to extensive mixing near the interface, we might expect a large number of the implanted ions to be

incorporated into the substrate or a uniform background concentration of silicon throughout the layer. Finally, amorphous silicon clusters might account for a large fraction of the implanted silicon inclusions without contributing to the photoluminescence signal.

A separate issue is the possibility of native oxide regrowth that might thicken the remaining layer after the etching procedure and lead us to overestimate the remaining equivalent thickness at each etch step. This is apparent for samples that are completely etched down to the substrate that show no photoluminescence, for which we measure a native oxide thickness of ∼3 nm. The data points recorded for very thin oxide layers might be less reliable for this reason. We can also speculate that the etching process could damage a greater fraction of the nanocrystal distribution than the physically remaining oxide thickness reflects. This would also tend to cause an overestimate of the remaining equivalent oxide thickness at any given etch depth. These effects could cause an artificial narrowing or shift in the distribution we find for optically active nanocrystals.

In spite of these difficulties, we estimate that the equivalent oxide thickness data can provide an accurate measure of the remaining physical layer thickness to within ∼3 nm. Note that the precision of our measurement is higher (∼1 nm) and therefore relative distances should have better than 3 nm accuracy. We are able to draw several important qualitative conclusions about the distribution of optically active nanocrystals from the optical characterization procedure.

Figure 2.7 shows the peak photoluminescence intensity, which is a measure of the integrated photoluminescence over the fraction of the depth distribution that remains at each equivalent oxide thickness. The drawn red line is the calculated differential photoluminescence intensity, which we interpret as a measurement of the optically active nanocrystal population depth distribution. Within our estimated ∼3 nm thickness error, we see excellent agreement between the peak in the nanocrystal distribution and the simulated implantation depth. Notably, the width of the nanocrystal distribution is quite narrow in comparison to the implantation profile shown in figure 2.2.

We have plotted the peak wavelength of the photoluminescence spectra as a function of the remaining equivalent oxide thickness in figure 2.8. The data suggest that the large nanocrystals are centrally located within the depth distribution and that smaller nanocrystals are more prevalent in the shoulders of the implanted distribution. We have included a scale bar indicating the corresponding nanocrystal sizes according to a phenomenological model

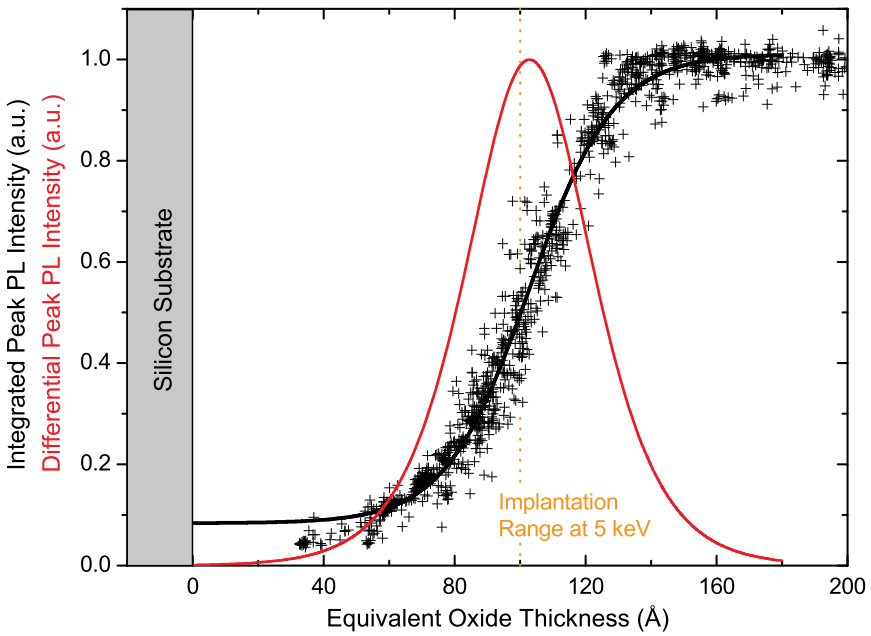

Figure 2.7. The depth-resolved differential peak photoluminescence intensity (drawn in red) suggests that the optically active nanocrystals are distributed in a region that is narrow in comparison to the implantation profile.

given by Ledoux [55]. Note that the spectra do not show a shift to shorter wavelengths until after the large nanocrystals at the peak of the distribution have been removed. The dashed line is drawn to suggest the actual depth distribution for nanocrystal diameters which may be symmetrical.

This optical characterization technique could easily be used in a comprehensive experiment correlating implantation or annealing conditions to the nanocrystal depth distribution or applied in the study of nanocrystals fabricated in thin films by other methods. Improvements that could be made include the use of ultraviolet ellipsometry that might allow the silicon concentration to be detected or the use of improved surface chemistry to limit possible oxide regrowth after the staircase etching procedure.

2.5 Photoluminescence Time Dynamics

The time dynamics of photoluminescence in silicon nanocrystals are fairly well known experimentally. Photoluminescence is characterized by $1/e$ decay rates in the range of 1–100 kHz, depending primarily on sample quality and nanocrystal density. This stands in

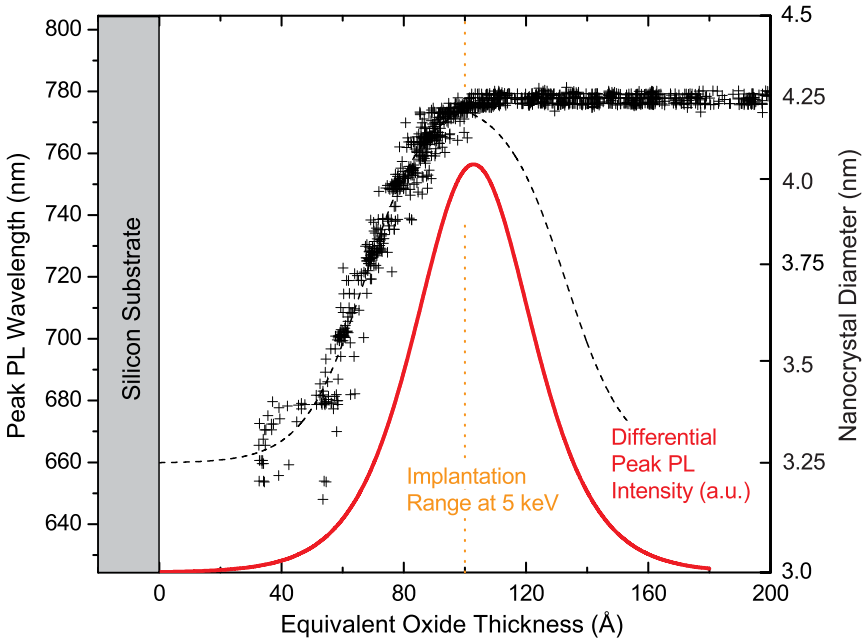

Figure 2.8. The peak wavelength for photoluminescence as a function of remaining oxide thickness suggests a depth distribution for the average nanocrystal size created by ion implantation. The wavelength shifts after the peak of the differential photoluminescence intensity (red curve) is etched away. The dashed curve shows the nanocrystal size distribution suggested by the wavelength data [55].

contrast to much faster photoluminescence decay rates associated with oxide defects states (∼10–100 MHz) and can provide strong supporting evidence when attempting to identify nanocrystal luminescence against a background signal. At much slower time scales, it is possible to observe "blinking" effects in single nanocrystal measurements, in which the nanocrystal switches between dark and emitting states [115]. The blinking phenomena is believed to be caused by the intermittent trapping of an electron or hole from a photoexcited nanocrystal within the surrounding oxide matrix. The charge remaining behind completely quenches photoluminescence through Auger recombination until the trapped carrier returns to the nanocrystal [110]. The time scale for Auger recombination is assumed to be several orders of magnitude faster than radiative recombination, but to our knowledge has not been quantitatively measured in silicon nanocrystals [119]. Under intense pulsed excitation in dense nanocrystal ensembles, it is additionally possible to observe stimulated emission processes on nanosecond time scales in silicon nanocrystals [66–69].

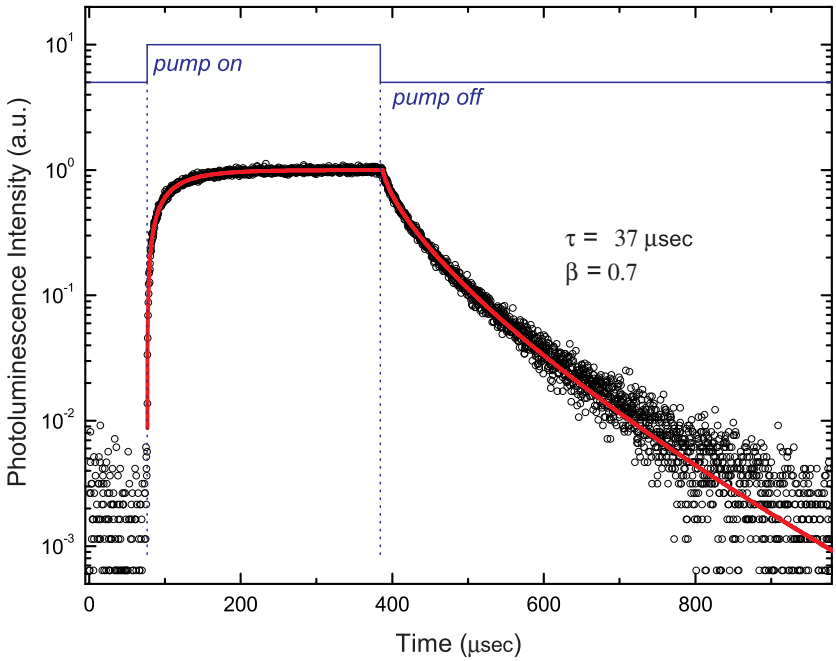

Figure 2.9. A typical time resolved photoluminescence measurement for silicon nanocrystals recorded at an emission wavelength of 750 nm. The pump beam (488 nm; ∼100 W/cm^2) is abruptly turned off in ∼10 ns using an acousto-optic modulator. The excited population of nanocrystals decays with a characteristic microsecond scale time constant.

Figure 2.9 shows a typical example of a time-resolved photoluminescence measurement for silicon nanocrystals formed by ion implantation. The data correspond to a sample in which a 100 nm thick oxide layer was implanted at 5 keV to a total implanted fluence of 1.2×10^{16} ions/cm^2, corresponding to a 20% atomic excess Si concentration at the peak of the implanted ion distribution. This sample was annealed in a tube furnace at Caltech once to form nanocrystals (1100 °C; 10 min; 2000 ppm O_2:Ar) and again to passivate implantation damage (450 °C; 30 min; 10% H_2:N_2). The data clearly show the characteristic microsecond time scale for photoluminescence decay in silicon nanocrystals. The drawn line is the least-squares best fit to the "stretched exponential" or Kohlrausch decay equation,

$$I(t) = I_0 e^{-\left(\frac{t}{\tau}\right)^{\beta}},$$

where the photoluminescence intensity $I(t)$ decays from an initial value I_0, τ is the $1/e$ experimental decay time, and the dimensionless parameter β is an ideality factor that accounts

for deviation from the single exponential decay curves ($\beta = 1$) that would be expected for an isolated two-level optical system. The stretched exponential decay function is nearly universally used to report photoluminescence decay measurements for silicon nanocrystal ensembles. Our data are well fit by a stretched exponential with $\beta = 0.7$, a typical value for ion implanted silicon nanocrystals.

Despite the widespread use of the stretched exponential function in reports of time-resolved silicon nanocrystal photoluminescence decay, the underlying physical mechanism is not well understood. Measurements of samples with varying nanocrystal density strongly suggest that concentration effects involving internanocrystal interactions are responsible for the "stretched" decay behavior [27, 100]. The β parameter tends to be closest to unity in sparse ensembles at low emission energies (long wavelengths) that correspond to large nanocrystals [109]. This suggests that the shape of the decay is related to energy transfer relaxation processes, which require the nanocrystals to be in close proximity and are most pronounced for small nanocrystals that are "uphill" in the energy landscape of the ensemble. However, a consensus model for this phenomenon has not yet emerged.

Recently it has been proposed that the decay should be expressed as a distribution of single exponential decay components [120]. This decomposition procedure is essentially equivalent to transforming the decay data from the time domain into the Laplace domain and adds little in the way of new physical insight by itself. However, one can propose that energy transfer causes the deviation from single exponential decay by introducing a distribution of additive decay paths to the ensemble. In this case, the distribution of single exponential decay is caused by the distribution of energy transfer rates. The average rate found in the calculated distribution should be interpreted as the most likely total decay rate, rather than be associated directly with the radiative decay component. Mathematically, the exact transform of the stretched exponential must include decay rate components that are arbitrarily slow, and the average decay rate is undefined [121]. This underscores the importance of considering the stretched exponential decay as a phenomenological description of silicon nanocrystal photoluminescence.

We would like to be able to determine the radiative rate for spontaneous emission from our ensemble decay measurement. The radiative rate effectively sets a lower bound on the decay dynamics because any additional decay pathways can only increase the overall decay rate. Therefore the radiative rate for isolated nanocrystals must be identified with the

slowest single exponential rate that appears in the calculated distribution. However, the slow-process shoulder of the calculated rate distribution is very sensitive to noise from an experimental standpoint when we attempt to directly transform our data. This should be expected because the stretched exponential equation fits the experimental data very well and yet has no slowest rate. In order to relate the radiative recombination rate to the $1/e$ decay rate of an ensemble measurement, we are forced to model the energy transfer process and predict the shape of the distribution for energy transfer rates. This is problematic because the energy transfer process is not well understood, and many different models correspond to the available data.

Some insight into the difficulty of modeling the energy transfer contribution to photoluminescence decay in dense ensembles can be gained by considering the simple rate equation that describes a two level optical system:

$$\frac{\mathrm{d}}{\mathrm{d}t}N^{*}\left(t\right)=\sigma\cdot\phi\cdot\left(N_{total}-N^{*}\left(t\right)\right)-\Gamma_{decay}\cdot N^{*}\left(t\right), \tag{2.1}$$

where $N^{*}\left(t\right)$ and N_{total} are the excited state and total nanocrystal populations, σ is the cross section for excitation, ϕ is the incident pump photon flux, Γ_{decay} is the total relaxation rate, typically taken to be the sum of radiative and nonradiative contributions. In order to model nonsingle exponential decay we must add physically meaningful complexity to this equation. It is reasonable to adjust the nonradiative decay component to reflect a concentration dependent energy transfer process:

$$\Gamma_{decay}\left(N^{*}\right)=\Gamma_{radiative}+\Gamma_{nonradiative}+\Upsilon\left(N_{total}-N^{*}\right),$$

where Υ describes a energy transfer decay component that is explicitly dependent on the population of ground state nanocrystals and the time dependence of the excited state nanocrystal population has been suppressed for clarity. Applying this modification to equation (2.1) immediately results in complicated nonlinear system dynamics.

Following the method of Inokuti and Hirayama [122] we can introduce a simplifying assumption that the energy transfer decay component is independent of the excited state population and instead assume that each arrangement of nanocrystals in the ensemble can

be described independently:

$$\{\Gamma_{decay}\}_i = \Gamma_{radiative} + \Gamma_{nonradiative} + \Upsilon\left(N_{total}\right)_i,$$

leading to an expression for the decay of each individual nanocrystal arrangement from steady state when the pump is turned off:

$$\begin{aligned}\{N^*(t)\}_i &= {N^*}_{steady-state,i} \cdot e^{-t\left(\Gamma_{radiative}+\Gamma_{nonradiative}+\Upsilon(N_{total})_i\right)} \\ &= {N^*}_{steady-state,i} \cdot e^{-t(\Gamma_{radiative}+\Gamma_{nonradiative})} \cdot e^{-t\Upsilon(N_{total})_i},\end{aligned}$$

where the linear decay components have been separated from the energy transfer term. In our experiments we measure the ensemble average decay curve:

$$\langle N^*(t)\rangle = \langle {N^*}_{steady-state}\rangle \cdot e^{-t(\Gamma_{radiative}+\Gamma_{nonradiative})} \cdot \left\langle e^{-t\Upsilon(N_{total})_i}\right\rangle,$$

in which the ensemble average energy transfer decay component $\left\langle e^{-t\Upsilon(N_{total})_i}\right\rangle$ must be evaluated by assuming a particular model for the energy transfer rate as a function of nanocrystal separation distance, $\Gamma(r)$, and the distribution of nanocrystal separation distances in the sample. By assuming that the nanocrystal locations are random and uncorrelated and that the energy transfer rate is a decreasing function of separation distance we find:

$$\left\langle e^{-t\Upsilon(N_{total})_i}\right\rangle = \lim_{V_{sphere}(r)=\frac{4\pi}{3}r^3\to\infty} \frac{4\pi}{V}\int_0^r e^{-t\Gamma(r)} r^2 \mathrm{d}r.$$

This expression can be evaluated numerically for several different energy transfer models, including the exponentially varying exchange mechanism described by Dexter [123], dipole–dipole interaction described by Förster [124], and higher-order electromagnetic couplings (dipole-quadrupole, quadrupole-quadrupole, etc.) [122]. The decay dynamics are sufficiently rich to fit silicon nanocrystal photoluminescence decay curves that are more commonly reported in terms of the stretched exponential function.

The important result of this model is the prediction of a slowest decay rate that we can associate with the radiative emission of an isolated nanocrystal. Stretched exponential decay curves with $\beta = 0.7$ can be fit using several different expressions for the transfer rate $\Gamma(r)$. For the case of dipole-dipole energy transfer ($\Gamma(r) \propto 1/r^6$)), we find that our data are

well fit by assuming the stretched exponential decay rate is ∼2.8 times faster than the single nanocrystal radiative rate and that the characteristic distance scale for the energy transfer is ∼3.3 nm. The dipole-dipole model predicts very fast energy transfer for nanocrystals that are separated by less than this critical distance. We can get equally reasonable fits by assuming that energy transfer occurs by an exchange mechanism. In this case, the best fit to Inokuti's model yields an ensemble rate that is ∼3.6 times faster than the suggested radiative recombination rate. Energy transfer occurs at a critical length scale of ∼3.8 nm and remains an ∼1 μs process even for closely spaced nanocrystals. These model predictions match well with experimental evidence suggesting that the stretched exponential decay rate for a well passivated dense ensemble is ∼3 times faster than the single exponential decay rate observed at the same wavelength in sparse nanocrystal samples [27, 100].

This model has many apparent weaknesses and the decay dynamics for silicon nanocrystals in ensembles should be considered an open problem. The assumed uniform separation distance probability distribution fails to properly consider the characteristic separation distances that should arise during the nanocrystal formation anneal as a consequence of the Ostwald ripening process. The size distribution of the silicon nanocrystals in the ensemble is ignored, as is the dependence of the energy transfer rate on the size of the donor and acceptor nanocrystals. The probability that the acceptor nanocrystal is already in the excited state is not included, although this should be less important in the low pump power regime. Perhaps most importantly, the model predicts that energy transfer is more likely than radiative decay, but fails to properly account for energy transfer as an excitation mechanism.

2.6 Internal Quantum Efficiency

We have studied changes in the photoluminescence decay rate of silicon nanocrystals that are caused by the geometry of the sample in order to determine the internal quantum efficiency of photoluminescence. The basis of the experiment is the modification of the spontaneous emission rate of a dipole emitter in proportion to the local density of optical states (LDOS) [125–129]. In contrast to methods that are more commonly used to determine the quantum efficiency through the ratio of output power to input power, this technique does not require the use of a reference sample or the estimation of excitation or collection

efficiency. The samples we use consist of identical ensembles of silicon nanocrystals embedded in oxide layers of differing thickness on a silicon substrate. The photoluminescence decay rate of the nanocrystals varies with the changing LDOS as the separation distance between the ensemble and the silicon substrate is altered. The quantum efficiency and the decay rates are found by comparing the magnitude of the decay rate modification to a calculation of the LDOS. This approach allows rates to be independently determined for both the radiative and the nonradiative decay components. During this experiment, we also found a power-dependent component of the measured nanocrystal decay rate, which is indicative of complex photocarrier dynamics and interactions among nanocrystals under intense excitation.

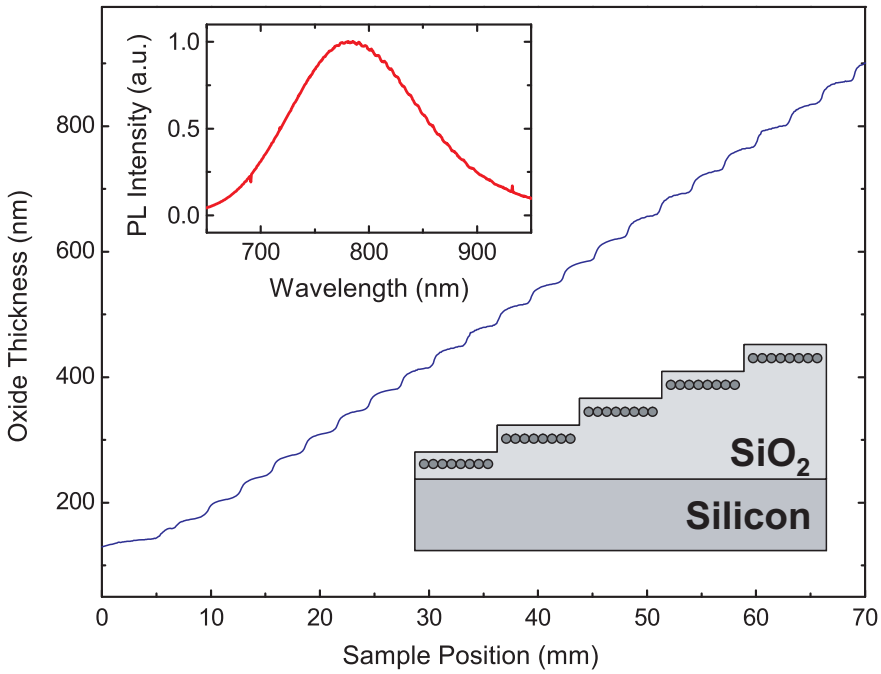

Figure 2.10. Oxide thickness along a staircase-etched sample as measured with spectroscopic ellipsometry. The silicon nanocrystals form near the SiO_2-to-air interface as indicated schematically (inset, lower right). A representative nanocrystal photoluminescence spectrum shows typical near-infrared emission (inset, top left).

2.6.1 Method

Two samples were prepared via computer controlled immersion of an SiO_2 layer into a buffered HF solution (see figure 2.10). Sample A was fabricated from an initially 1 μm thick SiO_2 layer grown by wet thermal oxidation at an etch rate of 1 nm/s (1:4 48% HF:H_2O), while sample B was etched at a rate of 0.25 nm/s (1:20 48% HF:H_2O) from an initially 105 nm thick oxide grown by dry oxidation. A photograph of sample A is shown in figure 2.11. The resulting thickness profiles were measured using spatially resolved spectroscopic ellipsometry (shown for sample A in figure 2.10). Both samples were implanted with $^{28}Si^{+}$ ions at 5 keV to a fluence of 1.2×10^{16} ions/cm^2. The resulting silicon depth profile, as obtained by a Monte-Carlo simulation using SRIM [85], peaks at a depth of 10 nm with a predicted 20% atomic excess Si concentration and 3 nm full width at half maximum. The two samples were annealed simultaneously in a tube furnace (1100 °C; 10 min; 2000 ppm O_2:Ar) in order to precipitate nanocrystals from the supersaturated solution. This process was followed by a second annealing step to passivate surface defects (450 °C; 30 min; 10% H_2:N_2).

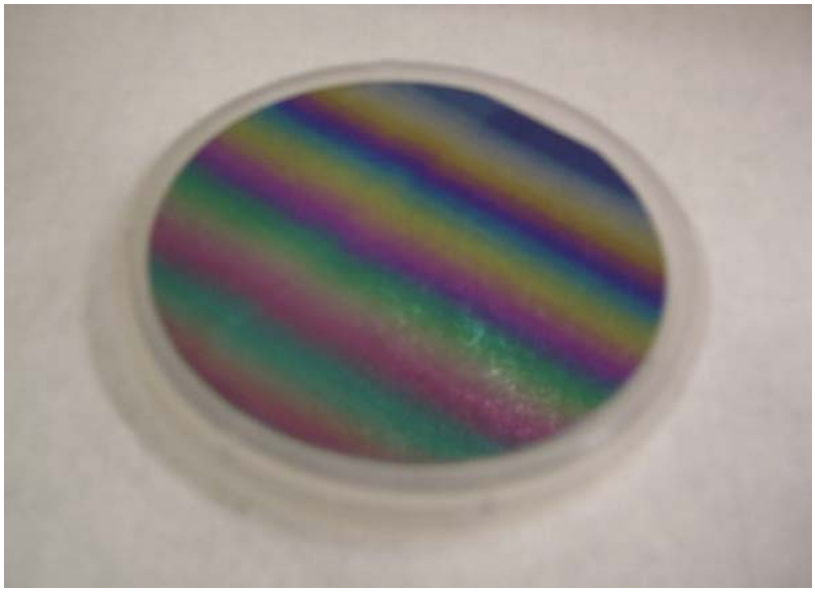

Figure 2.11. A staircase-etched oxide sample prepared for our internal quantum efficiency experiment from a 100 mm silicon wafer with an initially 1 μm thick SiO_2 layer grown by wet thermal oxidation.

After the nanocrystal fabrication, the thickness profile of each sample was again mea-

sured using spectroscopic ellipsometry. The ellipsometry data can be fit using a Bruggeman effective medium approximation, but covariance precludes a unique value for the nanocrystal array depth. We have therefore assumed that the nanocrystal array is located at the simulated implantation depth of 10 nm and allowed a relative error of ±5 nm in our data analysis.

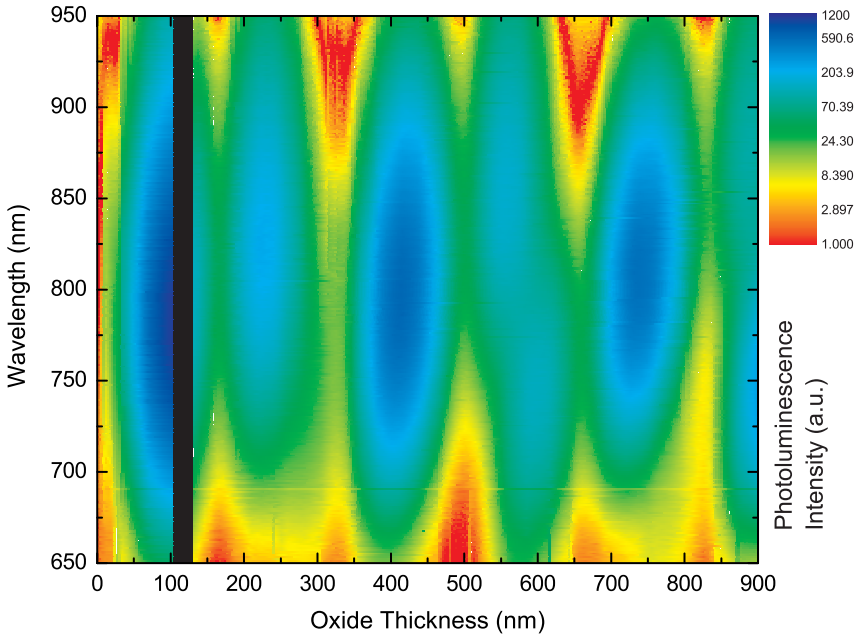

Figure 2.12. Experimental map of the spectral variation in the photoluminescence intensity as the oxide layer thickness below the nanocrystal ensemble changes. The data exhibit periodicities associated with both the silicon nanocrystal emission spectrum and the pump wavelength (488 nm).

Silicon nanocrystal photoluminescence spectra were measured at different positions along the sample at room temperature. The 488 nm line of an Ar^+ ion laser, focused to a 300 μm diameter spot, was used to excite the nanocrystals at normal incidence. Photoluminescence spectra were collected using a spectrograph equipped with a CCD array detector. A representative photoluminescence spectrum measured for nanocrystals embedded in a 105 nm thick oxide layer (sample B) shows broad near-infrared emission (figure 2.10 inset), typical of silicon nanocrystal ensembles. A photoluminescence map of data from both samples is shown in figure 2.12. Spectral modulation is observed that can be attributed to interference effects at both the excitation and emission wavelengths [130–132]. When

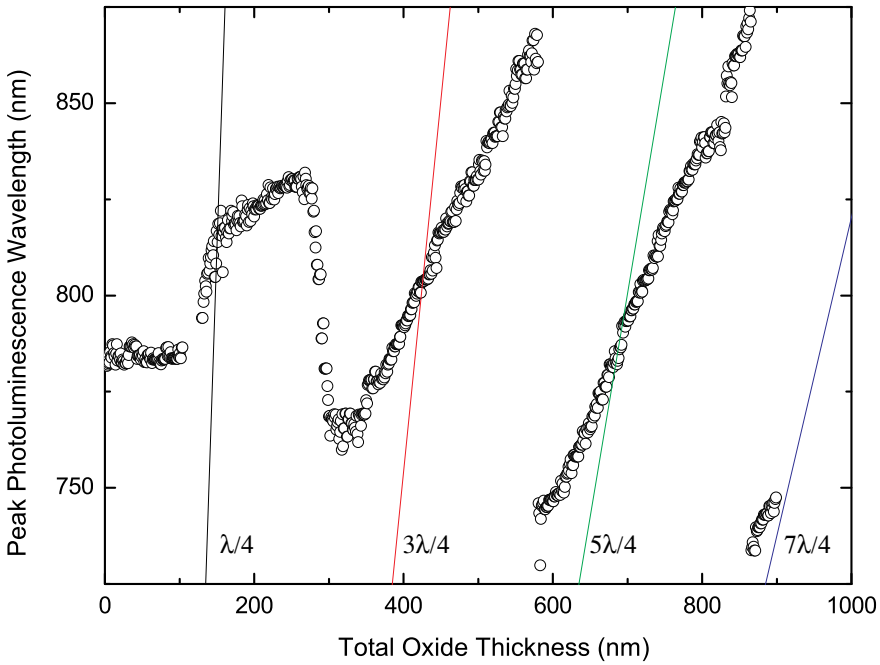

Figure 2.13. The peak silicon nanocrystal photoluminescence wavelength observed at each oxide layer thickness.

the photoluminescence map is normalized, a clear trend in peak emission wavelength can be identified (figure 2.13). The drawn lines shown in figure 2.13 represent the constructive interference modes at each wavelength assuming normal incidence interference in the SiO_2 film. This simple model can provide a useful qualitative explanation for the peak wavelength data. A more accurate model would need to account for the size distribution of the nanocrystals, wavelength dependent changes in the radiative rate and quantum efficiency, and the actual cavity resonances in the film at our off normal collection angle [133].

Time-resolved data were collected with a thermo-electrically cooled photomultiplier tube with photon counting electronics using an acousto-optic modulator to modulate the pump beam. Under high excitation power (100 W/cm^2), sufficient statistics were collected after a few minutes of signal integration. At low excitation power (1$-$10 W/cm^2), it was necessary to collect data for up to one hour at each oxide thickness.

2.6.2 Photoluminescence Decay Modeling

The decay of silicon nanocrystals in a dense ensemble is commonly described by a stretched exponential or Kohlrausch decay of the form:

$$I(t) = I_0 \exp\{-(\Gamma_K\, t)^{\beta}\},$$

where Γ_K is the ensemble average $1/e$ photoluminescence decay rate [134]. The value of β is typically near 0.7 for dense ensembles, while near single-exponential behavior ($\beta = 1.0$) is found in low-density ensembles [104, 109]. All our data are well fit using a fixed value of $\beta = 0.7$. This suggests that energy transfer between neighboring nanocrystals contributes significantly to the decay rates we observe. Laplace transformation of the stretched exponential function with $\beta = 0.7$ results in an underlying distribution of single exponential emitters that peaks at a decay rate of $0.435\,\Gamma_K$. Unfortunately, the precise nature of the energy transfer process is still unknown and complicates the interpretation of Γ_K as a measure of single exponential decay processes in the ensemble.

A model [122] that assumes that an excited nanocrystal acts as a donor and transfers its energy to neighboring acceptor nanocrystals can be used to describe the Kohlrausch decay. This model takes the statistical average of the decay rate of the donors, using a distance dependent energy transfer rate $\eta(r)$. Assuming a uniform distribution of acceptors, the single exponential decay rate Γ_0 for an isolated donor can be calculated, yielding $\Gamma_0 = 0.36\,\Gamma_K$ for dipole-dipole transfer ($\eta(r) \propto 1/r^6$) between nanocrystals and $\Gamma_0 = 0.30\,\Gamma_K$ when a exponentially decreasing transfer mechanism is assumed. A change in Γ_0 shifts the distribution in such a way that Γ_K is always proportional to the intrinsic single exponential decay rate Γ_0. Consequently the relative change in Γ_K is equal to the relative change in Γ_0, regardless of the transfer mechanism.

2.6.3 Experiment

Figures 2.14 and 2.19 show Γ_K measured at 750 ± 5 nm for high and low pump powers respectively. Both data sets show periodic variation in the decay rate as function of the oxide layer thickness. At high pump power (figure 2.14, symbols), the dominant variations match the periodicity expected for the interference pattern of the normal incidence 488 nm pump beam inside the oxide film (index of refraction $n = 1.48$). It is apparent that Γ_K

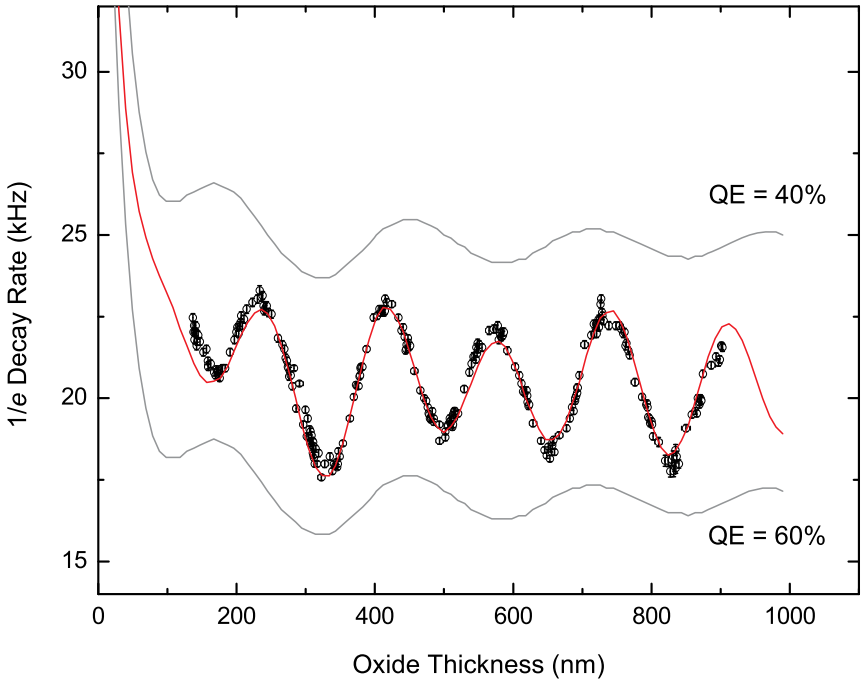

Figure 2.14. Variation of Kohlrausch $1/e$ decay rate Γ_K with oxide thickness at an emission wavelength of 750 nm under constant, high power pump conditions (symbols). The periodicity in the data is explained by additional decay that is proportional to the local pump power (solid line). The grey drawn lines show bounding quantum efficiencies of 40% and 60% (see section 2.6.5).

depends on the pump intensity. The solid line through the data is obtained by adding an additional decay component caused by the local pump intensity inside the SiO_2 film, to the low-power data shown in figure 2.19. The pump beam interference pattern can be used to verify the oxide thicknesses measured by spectroscopic ellipsometry and the best-fit phase shift (9 ± 3 nm) provides a verification of the assumed nanocrystal implantation depth.

The extra decay component we observe seems to vary linearly with the logarithm of the pump power for all wavelengths, as shown in figure 2.15. Figure 2.16 shows the residual power dependent decay component as function of the measured count rate (a measure of the local pump power) for emission at 750 nm. The origin of this additional decay component is unknown. An earlier report of pump power dependence in the photoluminescence decay rate of sparse Si nanocrystal ensembles proposed a model of biexciton formation followed by Auger recombination [109]. We speculate that pump power dependence in the internanocrystal nonradiative decay processes may also be important in these dense

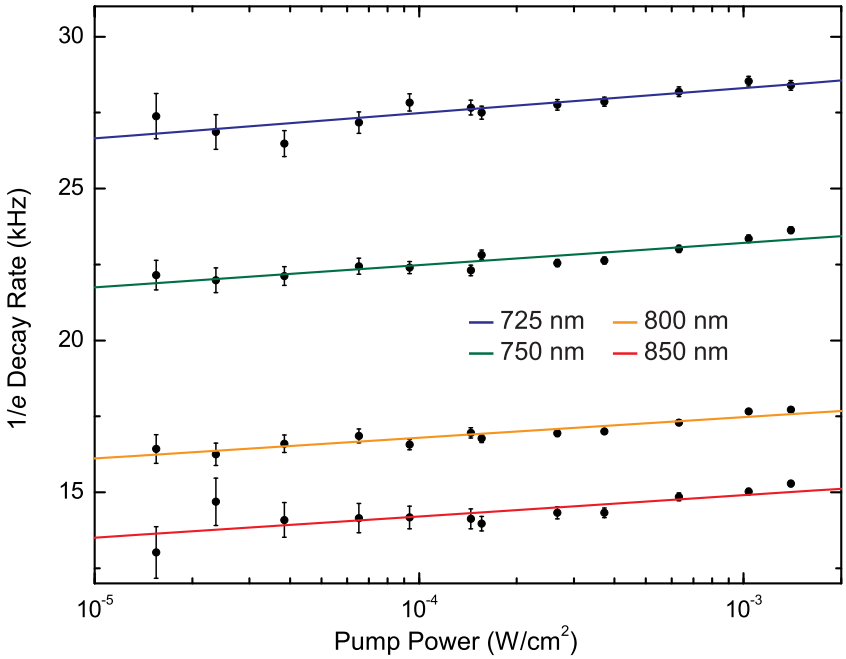

Figure 2.15. A power dependent contribution to the decay rate of the silicon nanocrystal ensemble is observed. The effect appears to vary linearly with the logarithm of the excitation power.

ensembles [110]. Photoionization associated with photoluminescence intermittence ("blinking") may also contribute [135]. In this model, the population of nanocrystals that become charged by photoionization would introduce slow nonradiative decay paths for nearby nanocrystals. Because of the limited range of the effect, the overall dependence on the pump power might correspond to the logarithmic dependence we observe.

At low excitation powers the decay rate is almost independent of pump power and a variation that depends on emission wavelength dominates. The interference pattern of the 488 nm pump beam makes constant-power illumination an experimentally inefficient approach to maintaining low-power excitation conditions. Instead, a feedback system was implemented on the pump laser intensity to maintain a roughly constant detection rate below 0.25 peak counts per second.

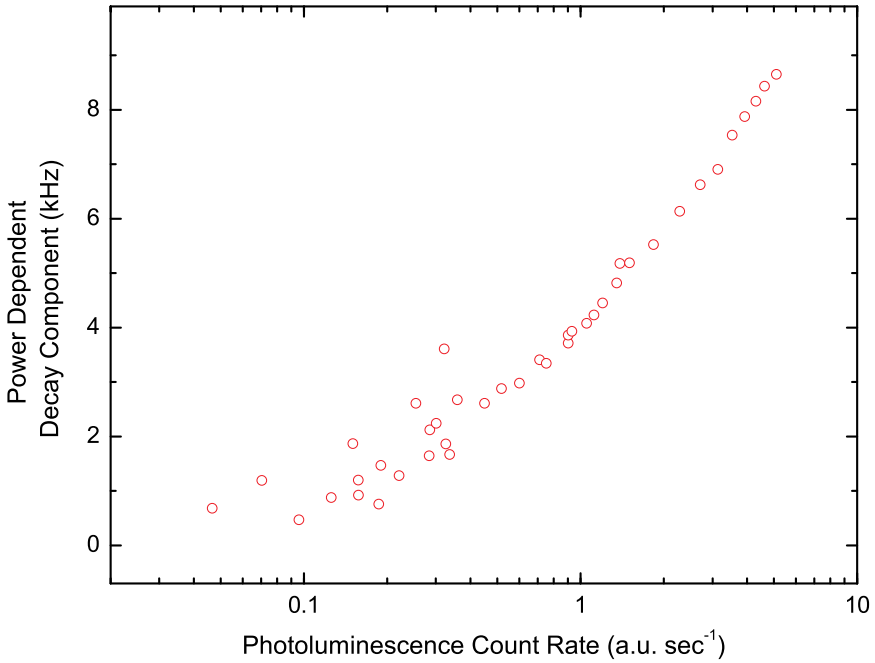

Figure 2.16. The power dependent contribution to the decay rate of the silicon nanocrystal ensemble at 750 nm. The count rate of the signal is used as a measure of the local pump power.

2.6.4 The Local Density of Optical States

The measured variation in the Kohlrausch decay rate Γ_K can be described at low pump power by:

$$\Gamma_K = \Gamma_{\text{LDOS}} \cdot \rho(\omega, z) + \Gamma_{\text{nonLDOS}}, \tag{2.2}$$

where $\rho(\omega, z)$ is the LDOS at the position z of the nanocrystal ensemble, and ω is the emission frequency. The decay rate component that does not depend on the local density of states Γ_{nonLDOS} may include energy transfer and nonradiative decay components, but is independent of the oxide thickness. nonradiative recombination is thought to depend primarily on the passivation quality at the nanocrystal-to-oxide interface, while energy transfer processes likely depend on the average arrangement of nanocrystals. This microscopic interfacial environment could vary from sample to sample (e.g., with changes in oxide quality or fabrication process) leading to differences in the intrinsic radiative rate or quantum efficiency.

To calculate the LDOS $\rho(\omega, z)$ that describes the position dependent spontaneous emission rate we employ Fermi's Golden Rule to describe the coupling between the nanocrystal

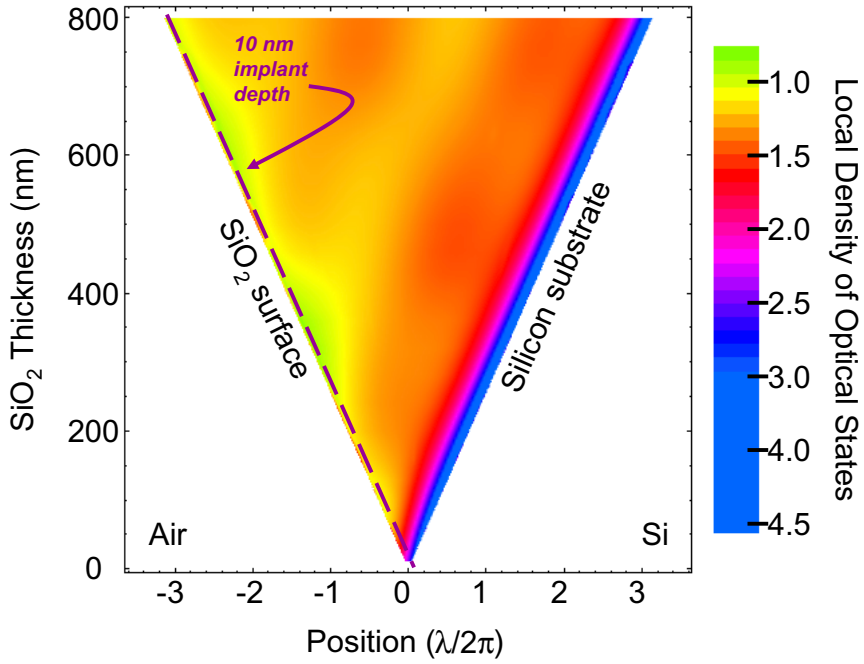

Figure 2.17. The local density of optical states inside an oxide layer on silicon varies between 0.8 and 4.4 of the value calculated for free space. The optical constants used in the calculation correspond to 800 nm light. The cut line indicated in the figure shows the location of the implanted silicon nanocrystal layer prepared for our internal quantum efficiency measurements.

and the radiation field [125, 128, 136]. We use $|i\rangle = |b\rangle \otimes |E_i\rangle$ and $|f\rangle = |a\rangle \otimes |E_f\rangle$ with energies $\hbar\omega_{i,f}$ as the initial and final states of the combined nanocrystal-radiation system of a nanocrystal with an excited state $|b\rangle$ and ground state $|a\rangle$. For the energy range of interest, the nanocrystal emission originates from recombination of quantum confined excitons in the dipole allowed singlet state [52, 137]. We therefore apply the electrical dipole approximation interaction Hamiltonian given by $\hat{H}_{int} = -\hat{\mu} \cdot \hat{E}(\vec{r})$ where $\hat{\mu}$ is the dipole operator and $\hat{E}(\vec{r})$ is the electrical field operator at the position of the nanocrystal. The decay rate can then be written as:

$$\begin{aligned} \Gamma(\vec{r}) &= D_{ab}^2 \sum_{\{n\}} \langle 0| \hat{E}(\vec{r})^\dagger |n\rangle \langle n| \hat{E}(\vec{r}) |0\rangle \delta(\omega - \omega_n) \\ &\equiv D_{ab}^2 \frac{\hbar\omega}{2} \rho(\omega, \vec{r}), \end{aligned}$$

where $D_{ab}^2 = \frac{2\pi}{\hbar^2} |\langle a| \hat{\mu} |b\rangle|^2$ is the oscillator strength for the transition. The quantity $\rho(\omega, \vec{r})$

is the radiative LDOS and is calculated by quantizing the radiation field according to

$$\hat{E}\left(\vec{r}\right)=\sum_{\{j\}}\left\{\frac{\hbar\omega_j}{2\varepsilon\left(\vec{r}\right)}ia_j^{\dagger}\varphi_j\left(\vec{r}\right)+h.c.\right\},$$

where $a_j^{\dagger}$ is the creation operator of the mode $|\varphi_j\left(\vec{r}\right)\rangle$ [128, 136]. The calculation of $\rho\left(\omega,\vec{r}\right)$ sums a complete set of normalized plane waves at a single frequency for each polarization. The radiative mode functions $\varphi_j\left(\vec{r}\right)$ contain both a propagating plane wave and a standing wave component dictated by the Fresnel coefficients of the two interfaces and the SiO_2 film thickness. Guided modes are absent in our case as the refractive index of the SiO_2 layer is lower than that of the silicon substrate.

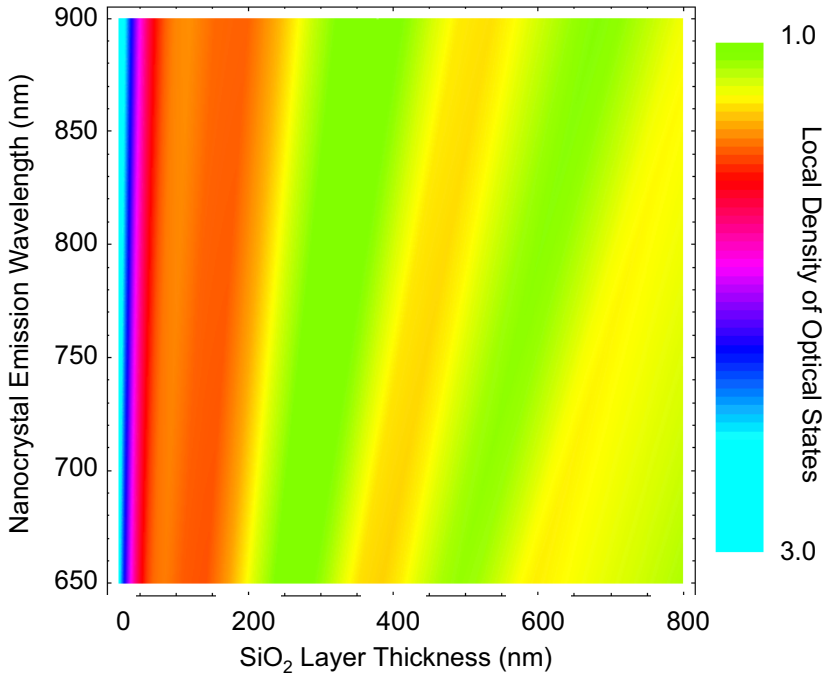

Figure 2.18. This map shows the variation in the local density of optical states at the nanocrystal position for each emission wavelength as a function of the staircase oxide thickness in our sample.

We use an isotropic combination of dipole orientations to calculate the LDOS at a constant distance of 10 nm from the SiO_2-to-air interface corresponding to the position of the nanocrystals. This is justified as the photoluminescence is unpolarized and both the luminescence and measured decay are independent of the pump beam polarization. The result

of this calculation is shown in figure 2.17 at positions inside an SiO_2 layer on a silicon substrate. A cut line through this map at the implantation depth of 10 nm allows us to calculate the LDOS curves shown in figure 2.18. The curves resemble those of earlier work with atoms close to a metal mirror [138]. This is not surprising as the silicon substrate reflects light efficiently at nanocrystal emission wavelengths [139]. In our calculation we have neglected the effects of absorption and homogeneous broadening. An equivalent classical electromagnetic calculation of the loss rate of a dipole antenna [125] that includes absorption differs from the above analysis by less than 2% at distances of <10 nm from the silicon substrate while perfect agreement is found at larger distances. Homogeneous broadening can be accounted for by averaging the calculated LDOS over a range of transition frequencies. This leads to a stronger damping of the modulation amplitude in the calculated emission rate as function of oxide thickness. For oxide thinner than one micron and a typical line-width of order 100 meV at room temperature [115, 140] the effect was found to be negligibly small.

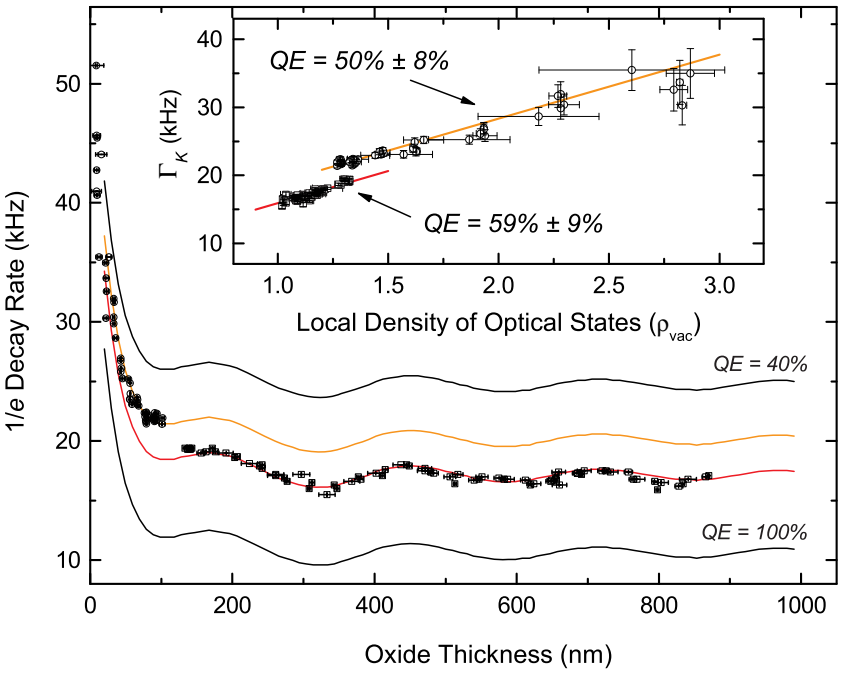

Figure 2.19. The Kohlrausch $1/e$ decay rate of silicon nanocrystals at 750 nm varies with oxide thickness in good agreement with a calculation of the local density of optical states at low pump power. The ensemble radiative decay rate (9.4 ± 1.3 kHz) and quantum efficiencies for two samples are determined by a least squares fit to the linearized data (inset).

2.6.5 Calculation of the Internal Quantum Efficiency

The drawn black lines shown in figure 2.19 give the calculated total decay rate for silicon nanocrystals emitting at 750 nm for different values of an internal quantum efficiency $QE = \Gamma_{\text{LDOS}}/(\Gamma_{\text{LDOS}} + \Gamma_{\text{nonLDOS}})$. The grey lines drawn through the data in figure 2.19 correspond to a best fit of equation (2.2) using the LDOS calculated as a function of the total oxide thickness. The best fit lines shown assume a common slope (local density of states dependent decay rate) Γ_{LDOS} of 9.4 ± 1.3 kHz corresponding to quantum efficiencies of 59 ± 9% and 50 ± 8% for samples A and B respectively. If sample variation in Γ_{LDOS} is allowed between samples A and B, perhaps due to changes in the local dielectric environment, rates of 10.7 ± 0.4 kHz and 7.5 ± 0.4 kHz are found. The corresponding quantum efficiencies for the two samples are then 38 ± 3% and 68 ± 4%.

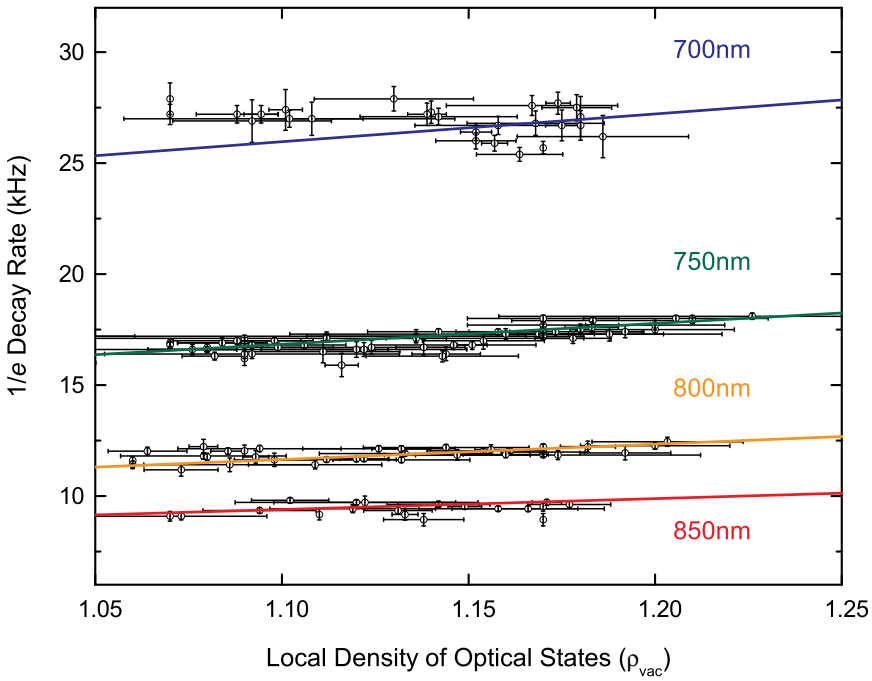

Figure 2.20. The measured total decay rate is resolved as function of the local density of optical states at different wavelengths. The drawn lines are the least squares best fit lines when the slopes are constrained to vary according to an effective mass model (see text).

We must consider two different energy transfer scenarios when connecting our measured internal quantum efficiency to the quantum efficiency for radiation. If the energy transfer mechanism scales linearly with the local density of optical states, as may be the case for the

dipole-dipole mechanism [141], the energy transfer decay component will contribute to the slope of equation (2.2) when fitting to the data in figure 2.20 rather than to the intercept. The internal quantum efficiency we measure, $QE = \Gamma_{\text{LDOS}}/(\Gamma_{\text{LDOS}} + \Gamma_{\text{nonLDOS}})$, is then the ratio of radiative recombination *and* energy transfer decay to the total decay. The radiative quantum efficiencies can then be calculated by accounting for the energy transfer decay component as indicated in figure 2.21. Here we have relied on experimental data showing that silicon nanocrystal decay at 950 nm is single exponential regardless of density, and that stretched exponential decay in dense ensembles is ∼3 times faster than single exponential decay in sparse nanocrystal ensembles at 700 nm [100].

On the other hand, if the energy transfer process is not proportional to the local density of states but is still the cause of the stretched exponential decay, it should contribute only to the intercept in equation (2.2). In this case, the values we measure are incompatible with the energy transfer rate being faster than ∼0.7 times the radiative decay rate. For an average energy transfer rate that is ∼3 times faster than the radiative decay rate at 700 nm (as suggested by both the Inokuti model and experiment), the maximum quantum efficiency $QE = \Gamma_{\text{LDOS}}/(\Gamma_{\text{LDOS}} + \Gamma_{\text{nonLDOS}})$ that we should measure is ∼25%. Our measurement of an internal quantum efficiency of ∼50% at 700 nm suggests that the energy transfer mechanism is not independent of the local density of optical states.

Our decay rate data are best compared to equation (2.2) when plotted against a linearized ordinate axis (shown inset in figure 2.19). The data are well fit by assuming a linear dependence on the local density of optical states. However, the internanocrystal energy transfer processes may still depend on the local density of optical states in a weakly nonlinear way [142]. An improved understanding of the physical mechanism behind energy transfer and the stretched exponential decay in silicon nanocrystal ensembles will be essential in resolving these concerns. It will also be important to consider whether or not the energy transfer process conserves energy when extrapolating from these measurements to an overall external power efficiency for photoluminescence.

We attribute the difference in quantum efficiency between samples A and B to sample-to-sample variation in the nonradiative decay rate. For comparison, the calculated total decay rates for quantum efficiency values of 40% and 100% are shown (black lines). The best fit LDOS dependent rate Γ_{LDOS} implies an intrinsic radiative rate Γ_0 of 5.0 ± 0.7 kHz for an isolated Si nanocrystal emitting at 750 nm in an ($n = 1.45$) infinite oxide matrix

assuming that dipole–dipole energy transfer is responsible for the nonexponential decay. This value is in good agreement with total decay rate values reported (∼6.5 kHz) for sparse nanocrystal ensembles of unknown quantum efficiency [109].

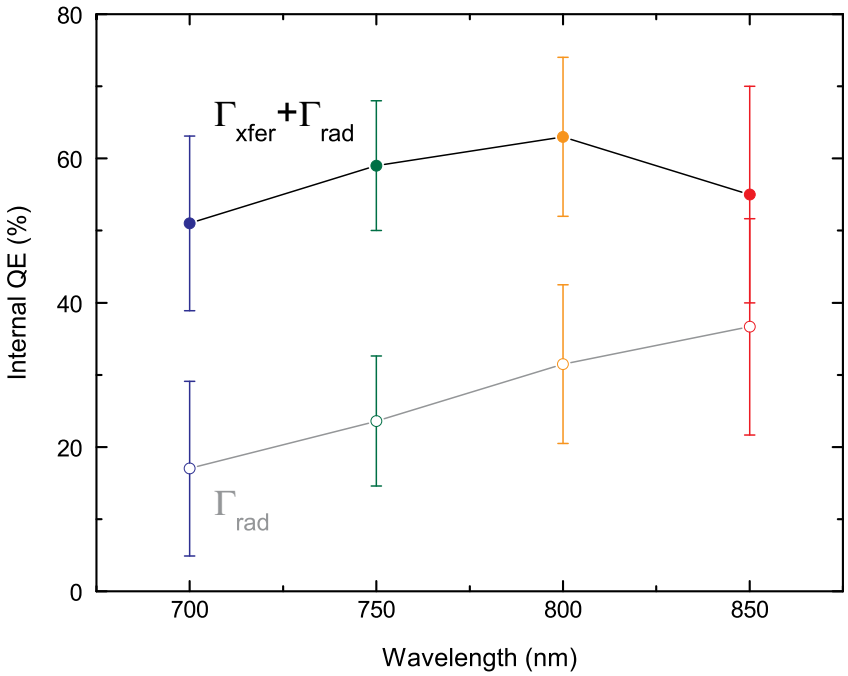

Figure 2.21. The calculated internal quantum efficiency is different at each emission wavelength. If the energy transfer mechanism varies in proportion to the local density of states, the larger values will represent the combined efficiency of energy transfer and radiative recombination. In this case, the smaller values provide an estimate of the quantum efficiency for photoluminescence.

The experiment can be repeated at other wavelengths to measure variation in both the intrinsic spontaneous emission rate and the quantum efficiency with nanocrystal size [143]. However, the measured signal level decreases substantially away from 750 nm due to decreasing detector sensitivity and nanocrystal photoluminescence yield. Doubling the integration time to 2 hours enabled measurements of the total decay rate over a limited range of LDOS values at other wavelengths. These data are plotted in figure 2.20. In order to determine quantum efficiency values from these measurements we assume that the intrinsic radiative rate of silicon nanocrystals varies according to an effective mass model appropriate to the size regime of the nanocrystals in this experiment [144]. This allows us to scale Γ_{LDOS}

as measured at 750 nm to other wavelengths while determining the corresponding $\Gamma_{\mathrm{nonLDOS}}$ experimentally. Figure 2.21 shows the results of this calculation, suggesting the existence of an optimum in the internal photoluminescence quantum efficiency for nanocrystals that emit near 800 nm [145].

Finally, we note that the quantum efficiency values we have calculated pertain only to the optically active fraction of nanocrystals in the ensemble that contributes to the photoluminescence signal.

2.7 Conclusion

Silicon nanocrystals can be created by the ion implantation method in dense ensembles through completely CMOS compatible processes. We have successfully used this technique to fabricate high quality layers of silicon nanocrystals in thin oxide layers on 300 mm substrates. The optically active nanocrystals form in a narrow region about the peak of the implanted silicon concentration, with the larger nanocrystals being concentrated in the center of the distribution. Although internanocrystal energy transfer processes are active in the silicon nanocrystal layers we fabricate, the nanocrystals emit light with high radiative quantum efficiency. For these reasons, ion implantation is a suitable process for the fabrication of silicon nanocrystal layers in optoelectronic devices.

Chapter 3

Silicon Nanocrystal Optical Memory

3.1 Introduction

In this chapter, we describe devices that allow simultaneous optical and electrical access to a dense ensemble of silicon nanocrystals. The nanocrystals comprise a floating gate layer embedded in the gate stack of a transistor. By monitoring the shift in the threshold gate voltage required to turn on the source to drain current, we can measure the quantity of charge stored in the nanocrystal ensemble. We simultaneously monitor the photoluminescence signal to determine the charge-dependent emission properties of the nanocrystals.

We show that these devices can function as optical memory elements at room temperature. The state of the memory is represented by the amount of charge stored in the nanocrystal ensemble, which is optically read by measuring the intensity of the photoluminescence signal. We are able to program and erase the memory electrically through charge injection, and optically through internal photoemission processes.

Excitons in charged silicon nanocrystals preferentially decay through Auger recombination, causing the photoluminescence signal to decrease in proportion to the charge stored in the nanocrystal. We also show that the residual photoluminescence decay lifetime decreases when the ensemble is charged as a result of internanocrystal energy transfer processes. Finally we demonstrate that the switching speed of our optical memory is ultimately limited by the decay rate of the silicon nanocrystal ensemble.

3.2 Optical Memory

An optical memory is a device that allows optical information content to be stored or retrieved without conversion between light and electrical signals [147, 148]. Ideally the device should not reduce the power of the optical data signal or would even provide signal gain.

A technologically useful device would have to offer some performance improvement over existing solutions that convert the optical signal to an electrical current for storage and regenerate the light for readout. The improved performance might be in data storage density, power efficiency, or in the read or write speed. A successful optical memory technology could be a useful replacement for the optoelectronic data buffers used in optical communication systems.

Conceptually, a single nanocrystal could function as an optical memory device for light at a single wavelength. As shown schematically in figure 3.1, a nanocrystal in the ground state could absorb an incident "write" photon. The exciton would effectively store the light for some time until it was lost to spontaneous emission. Within this retention time window, a second "read" photon could induce stimulated emission. The stored optical information encoded by the presence or absence of the "write" photon could be retrieved in the gain or loss of the "read" signal. The device would be naturally reset to the ground state by spontaneous emission and could then be rewritten with new optical information.

In practice this scheme would be extremely inefficient, because the probability of the incident photons interacting with the nanocrystal is small. The "read" photon might also be absorbed as a second exciton in the nanocrystal rather than cause stimulated emission, because the ground state of the nanocrystal will be at least two-fold spin degenerate (barring the possibility of lifting the degeneracy through the Zeeman effect or some other mechanism). The photon could be absorbed by the confined carriers that make up the exciton if higher energy states are available in the conduction or valence bands. Additionally, the retention time would be limited to a fraction of the spontaneous emission lifetime.

A more practical alternative design can be developed by allowing the "write," "read," and "signal" photons to be at different wavelengths. As depicted in figure 3.2, a high energy "write" photon could be used to photoionize a nanocrystal, leaving it in a charged state. A somewhat less energetic "read" photon is later used to pump the nanocrystal, allowing the state of the memory to be determined by the presence or absence of a "signal" photon emitted in photoluminescence. Charged nanocrystals would not emit photoluminescence, because of efficient Auger recombination processes that cause the excitons to recombine without emitting light. The optical memory devices we have fabricated for our experiments operate according to this mechanism, although we read and write a large ensemble of silicon nanocrystals simultaneously. We also electrically program the memory by injected charge

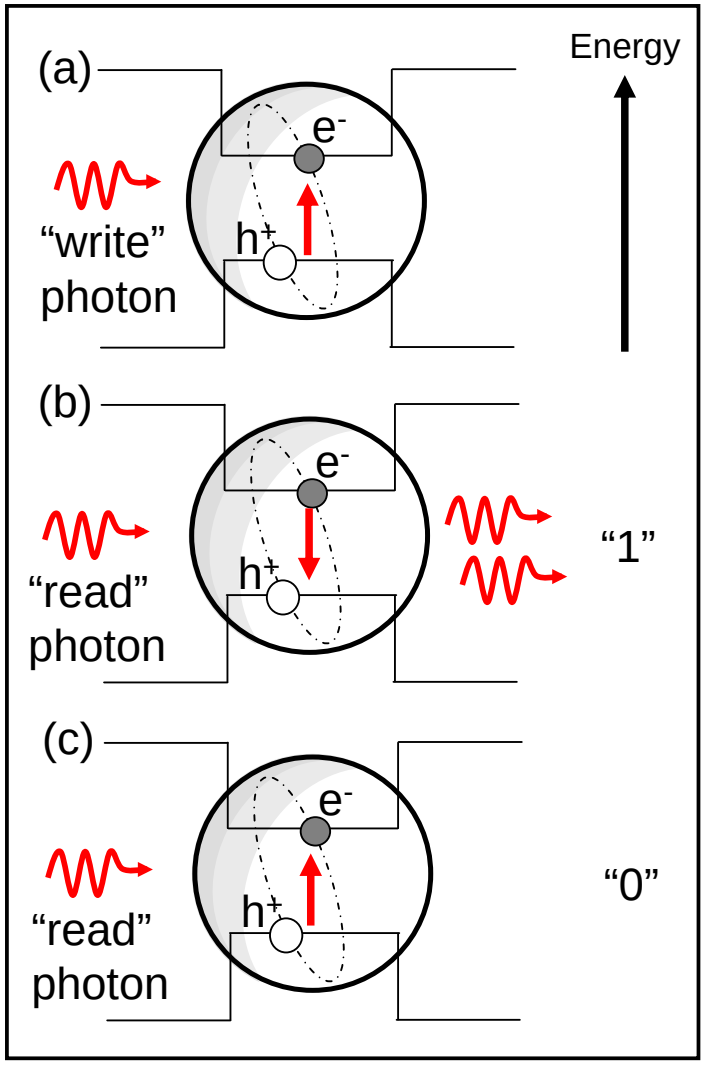

Figure 3.1. In principle a single nanocrystal could function as an optical memory device with signal gain. (a) The memory is written by either exciting an exciton or leaving the nanocrystal in the ground state. (b) If the nanocrystal contains an exciton (state "1"), the read photon is amplified by stimulated emission. (c) If the exciton was not written, the read photon is absorbed by the nanocrystal (state "0"). The memory is reset by spontaneous emission.

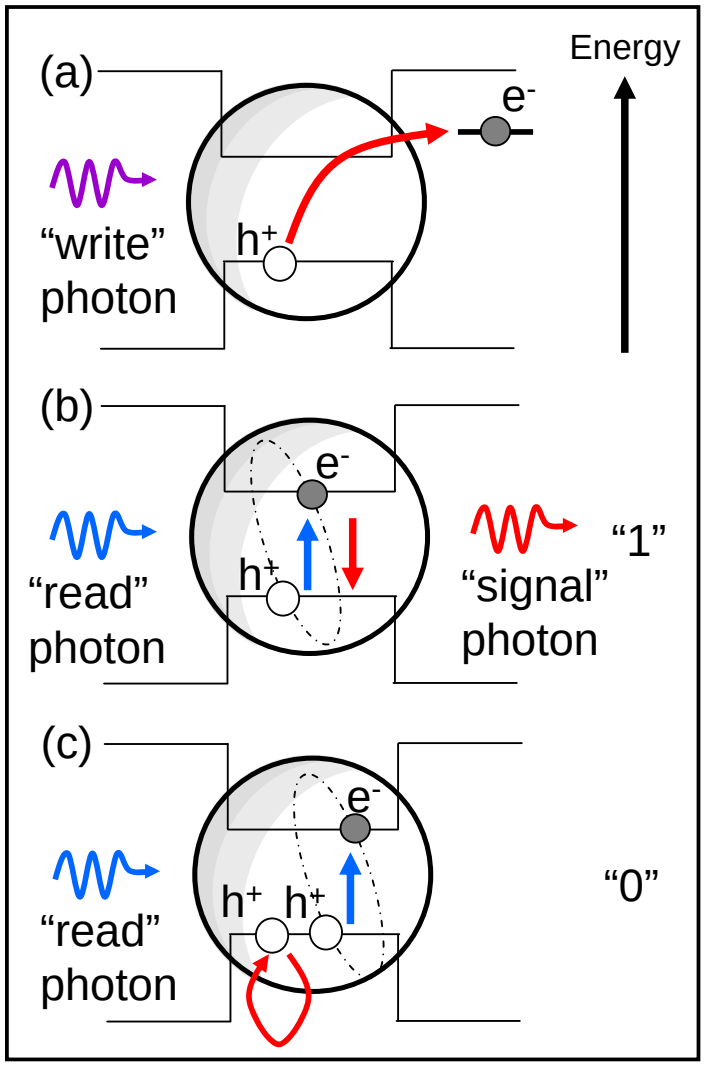

Figure 3.2. A more practical optical memory mechanism that does not preserve wavelength. (a) The memory is written by the photoionization of the nanocrystal by a high energy photon. (b) The photoluminescence of an exciton excited by the "read" photon is detected if the nanocrystal is neutral (state "1"). (c) Photoluminescence is quenched in a charged nanocrystal by Auger recombination (state "0"). Erasure occurs when the nanocrystal is neutralized by thermal processes.

into the nanocrystals. In this kind of device, the retention time is limited by thermally activated charge leakage processes that eventually neutralize the charged nanocrystals. In similar electrical memory devices, data can routinely be stored for many years.

Optical memory devices have also been reported in III–V quantum dot systems [149, 150]. These devices are written optically with "write" photons that are more energetic than the emitted "signal" photons, and readout is triggered electrically using a pulse of current. Because the carriers are confined in relatively shallow potential wells, these devices require cryogenic temperatures to operate. Additionally, the III–V materials used are not considered CMOS compatible. In contrast, our silicon nanocrystal based optical memory works at room temperature and is fabricated at Intel in the same facility used to produce Pentium processors.

3.3 Nanocrystal Floating Gate Memory

Our optoelectronic devices are electrically similar to nanocrystal-based memory designs first proposed as a replacement technology for "FLASH" electrically erasable programmable read-only memory (EEPROM) devices about ten years ago [151, 152]. figure 3.3 shows a schematic of a nanocrystal floating gate transistor. The basic idea is to discretize the floating gate where the recorded charge is stored so that the device is less sensitive to weak points in the insulating tunnel oxide. A good analogy is to imagine storing a quantity of water in many small buckets instead of in one large bathtub; if there is a leak in the bathtub all of the water will drain out, but a hole in one or two of the buckets will result in only a small volume of lost water. The greater resilience of a nanocrystal memory then allows one to consider tradeoffs in which the tunnel oxide of the device is more aggressively scaled to allow faster programming without compromising the expected information retention time.

Silicon nanocrystal floating gate memory technology was pursued for several years by Motorola and 4 Mbit prototype devices were eventually reported [153, 154]. However it now appears that these devices will probably not be commercialized. The reason for this is that scaling in the years since the devices were first proposed has reduced the size of floating gate FLASH transistors so much that the statistical (Poisson) distribution of the number of nanocrystals in each nanocrystal floating gate memory has become a concern. It is important from a circuit standpoint for each bit in the memory array to have identical

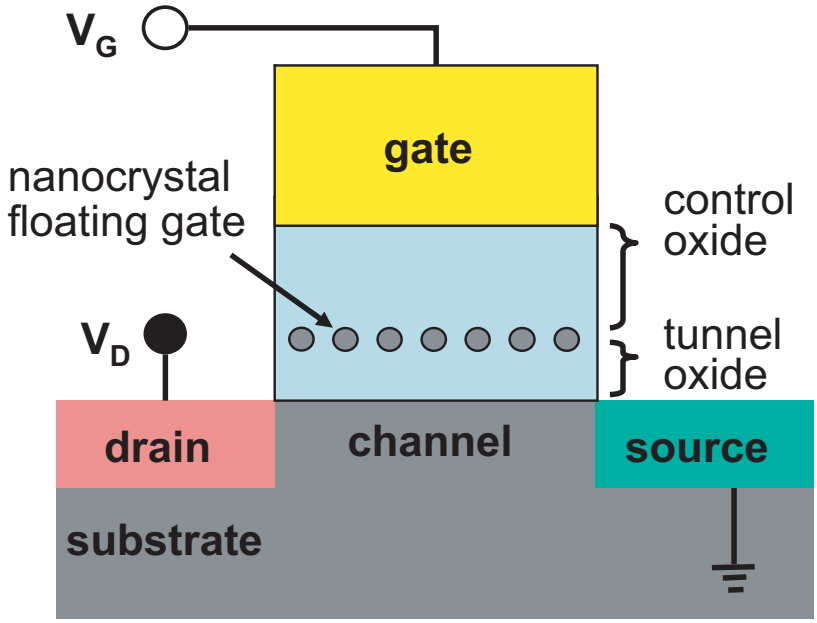

Figure 3.3. A schematic diagram of an electrical silicon nanocrystal floating gate transistor memory.

electrical properties. To reduce this problem, one might consider decreasing the size of the silicon nanocrystals and increasing the nanocrystal density to limit the statistical variation between transistors. However, this will increase the quantum confinement effect and therefore reduce the depth of the nanocrystal energy well that stores the charge. In the small nanocrystal device regime, metal nanoparticles that do not show quantum confinement effects may instead be preferred [155]. The reduced capacitance of smaller nanocrystals will also increase the Coulomb barrier effect and limit the total charge that can be stored on each nanocrystal. This will decrease the change in threshold gate voltage used to record the state of the memory electrically. Finally, increasing the nanocrystal density will increase the rate of energy transfer processes and reduce the isolation between individual nanocrystals that is responsible for the improved retention performance.

3.4 Device Fabrication

We have adapted the silicon nanocrystal floating gate transistor electrical memory design shown in figure 3.3 to make optical memory structures. In order to address the optical memory using free space optics, the transistors are intentionally made very large. We

fabricate 48 test structures in the same wafer area that is filled with ∼230 million transistors when Intel makes a state-of-the-art CPU. The field is repeated many times on each 300 mm substrate wafer, as shown in figure 3.4. In order to move our wafers more quickly through the fab at Intel, we used a single reticle process to define simple ring gate transistors. The field mask we designed for this purpose is shown in figure 3.5.

Figure 3.4. Silicon nanocrystal optical memory test devices fabricated on a 300 mm substrate at Intel.

Each device field provides a number of different transistor geometries designed to separate perimeter and area effects. According to the naming convention defined in figure 3.6, series A transistors scale with constant transistor channel width-to-length ratio (3), series B transistors have constant channel length and variable width, and series C transistors have the most symmetrical gates. Series R devices are meander resistors that allow us to determine the gate polysilicon resistivity. Series S defines capacitor structures. Tables 3.1, 3.2, and 3.3 give the dimensions for each device in the field.

The most important difference between our transistors and electrical nanocrystal floating gate memory is that our transistor gate layers are designed to be optically semitransparent. We attempted to balance the conductivity of the gate electrode with optical absorption by keeping the gate contact thickness as low as possible and by doping the gate contact at a reduced dopant concentration. The absorption of a 40 nm thick polysilicon layer is ∼50% at the blue argon ion laser wavelengths (457.9 nm, 476.5 nm, 488 nm) that are typically

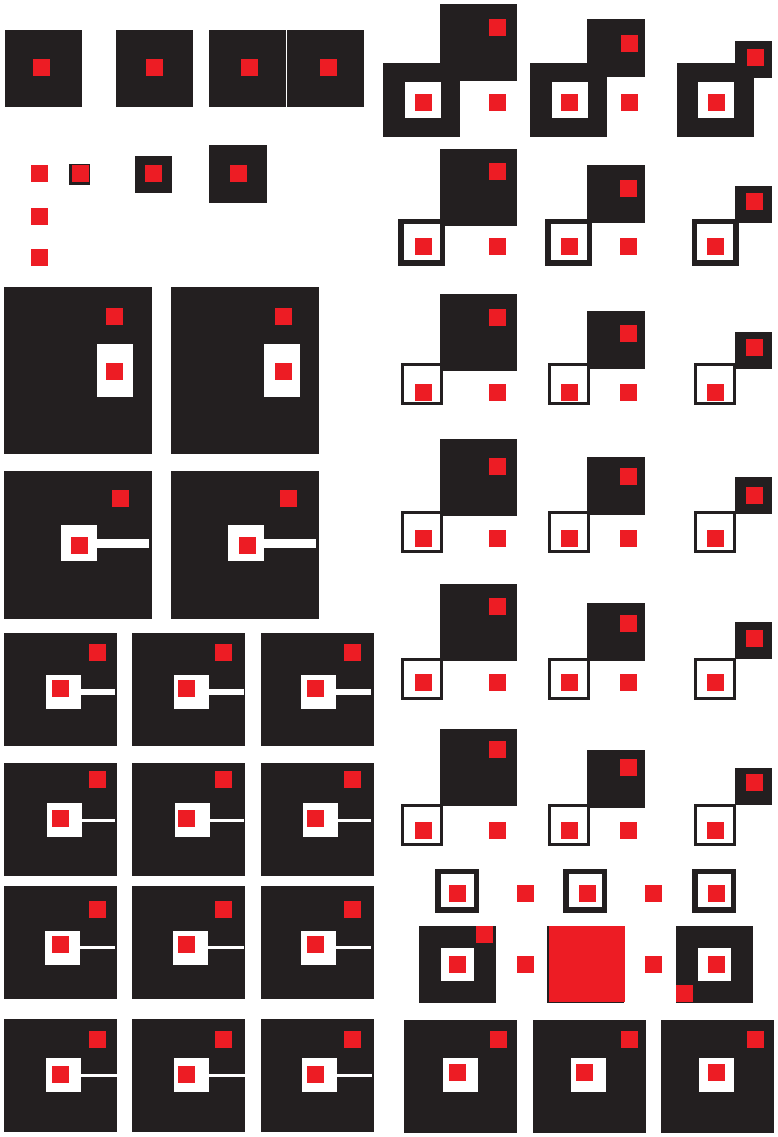

Figure 3.5. The field photolithography masks used to fabricate our ring gate optical memory structures. The black pattern was used at Intel to define test structures with ∼1 μm minimum feature sizes. The red pattern was used at Caltech to define metal contact pads (∼10 μm minimum feature size). The overall field dimensions are 22 mm × 32 mm. Devices $S1$ and $C5$ are used for alignment purposes.

used to pump silicon nanocrystals. However, such a layer absorbs only a few percent of the light emitted by the silicon nanocrystals in the near infrared. We also fabricated devices with 20 nm thick gate layers, but encountered significant problems with pinholing in the deposited polysilicon layers.

Our device fabrication process started with a targeted threshold voltage adjustment

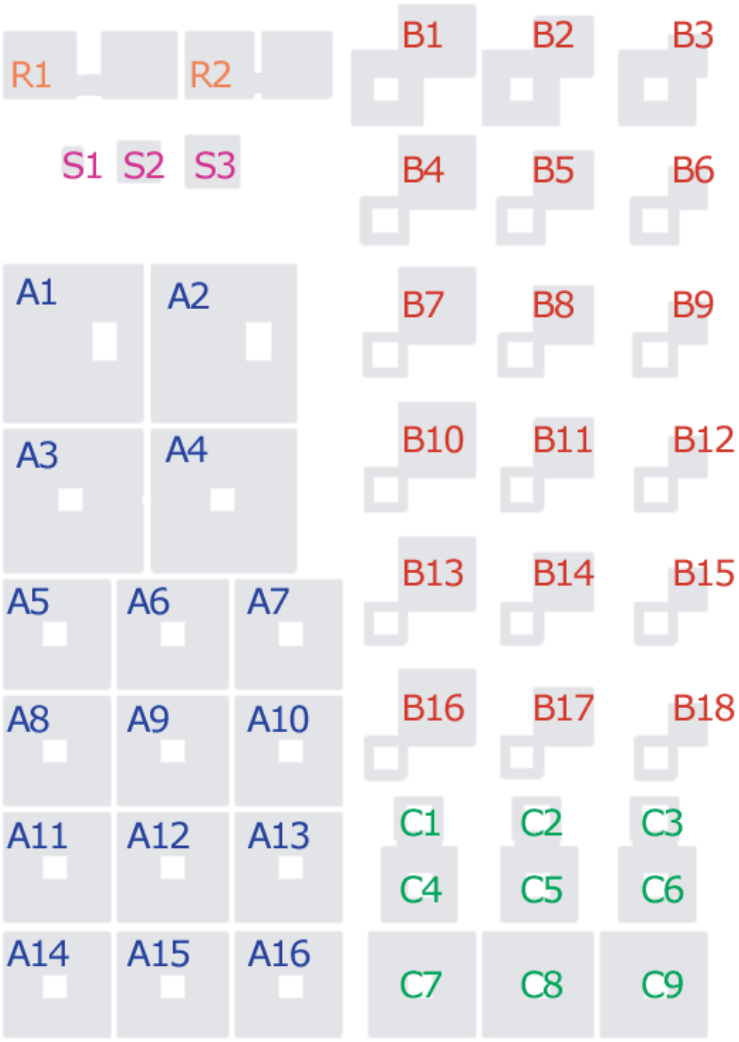

Figure 3.6. The naming convention adopted for our silicon nanocrystal optical memory structures.

implantation of boron (2×10^{13} cm^{-2} at 30 keV) into 300 mm p-type silicon wafers. Next a 15 nm dry thermal oxide layer was grown. The oxide layer was implanted with 1.27×10^{16} cm^{-2} $^{28}Si^{+}$ ions at an energy of 5 keV. This process produces a distribution of silicon rich oxide centered at a depth of 10 nm with a peak composition of $Si_{1.75}0_2$ as calculated using the TRIM code [85]. The wafers were then annealed in a rapid thermal annealing (RTA) furnace at 1080 °C for 5 minutes in an atmosphere containing 2% O_2 by partial pressure to precipitate nanocrystals out of the nonequilibrium solid solution. The background oxygen pressure was utilized to suppress changes in the stoichiometry of the gate

Table 3.1. Dimensions for the Si nanocrystal optical memory resistor devices named in figure 3.6

Resistors		
	Contact Pad Area (mm^2)	Meander Path (squares)
R1	4.000	500.000
R2	4.000	100.000

Table 3.2. Dimensions for the Si nanocrystal optical memory capacitor devices named in figure 3.6

Capacitors		
	Area (mm^2)	Perimeter (mm)
S1	0.250	2.000
S2	1.000	4.000
S3	2.250	6.000

oxide that could result from preferential oxygen desorption during the annealing process [89]. A 40 nm thick polysilicon layer was then deposited to form a semitransparent, conducting transistor gate layer for our devices. Subsequent photoresist patterning and etching was used to form the ring gate transistors and other devices shown in figure 3.5. Blanket implantations of $^{15}P^{+}$ (1×10^{16} cm^{-2} at 2 keV) and $^{33}As^{+}$ (1.6×10^{15} cm^{-2} at 12 keV) were made to simultaneously dope both the gate contact and the source drain regions. These implantations were carefully designed to avoid doping the silicon nanocrystals, which could result in a diminished radiative quantum efficiency. Finally, the devices were spike annealed in the RTA at 1080 °C for 2.5 seconds to activate the implanted dopant ions.

In order to provide reliable ohmic electrical contacts for our devices we developed a metallization process to add 100 μm × 100 μm gold contact pad patterns to individual fields diced from the 300 mm substrates after the initial fabrication steps had been completed in Intel's facilities. We followed the standard reference recipe for Microchem LOR3A lift-off resist using Shipley 1813 photoresist and a printed film negative mask (4000 dpi). The

Table 3.3. Dimensions for the Si nanocrystal optical memory transistor devices named in figure 3.6

Transistors						
	Gate Area (mm^2)	Gate to Source Perimeter (mm)	Gate to Drain Perimeter (mm)	Channel Length (mm)	Channel Width (mm)	Channel W:L Ratio
A1	16.500	5.000	17.000	0.500	1.500	3.000
A2	16.500	5.000	17.000	0.500	1.500	3.000
A3	14.580	6.800	16.000	0.100	0.300	3.000
A4	14.580	6.800	16.000	0.100	0.300	3.000
A5	7.858	5.900	12.000	0.050	0.150	3.000
A6	7.858	5.900	12.000	0.050	0.150	3.000
A7	7.858	5.900	12.000	0.050	0.150	3.000
A8	7.970	5.980	12.000	0.010	0.030	3.000
A9	7.970	5.980	12.000	0.010	0.030	3.000
A10	7.970	5.980	12.000	0.010	0.030	3.000
A11	7.985	5.990	12.000	0.005	0.015	3.000
A12	7.985	5.990	12.000	0.005	0.015	3.000
A13	7.985	5.990	12.000	0.005	0.015	3.000
A14	7.997	5.998	12.000	0.001	0.003	3.000
A15	7.997	5.998	12.000	0.001	0.003	3.000
A16	7.997	5.998	12.000	0.001	0.003	3.000
B1	6.750	4.000	14.000	0.500	4.000	8.000
B2	5.000	4.000	12.000	0.500	4.000	8.000
B3	3.750	4.000	10.000	0.500	4.000	8.000
B4	4.430	4.000	12.400	0.100	4.000	40.000
B5	2.680	4.000	10.400	0.100	4.000	40.000
B6	1.430	4.000	8.400	0.100	4.000	40.000
B7	4.208	4.000	12.200	0.050	4.000	80.000
B8	2.458	4.000	10.200	0.050	4.000	80.000
B9	1.208	4.000	8.200	0.050	4.000	80.000
B10	4.040	4.000	12.040	0.010	4.000	400.000
B11	2.290	4.000	10.040	0.010	4.000	400.000
B12	1.040	4.000	8.040	0.010	4.000	400.000
B13	4.020	4.000	12.020	0.005	4.000	800.000
B14	2.270	4.000	10.020	0.005	4.000	800.000
B15	1.020	4.000	8.020	0.005	4.000	800.000
B16	4.004	4.000	12.004	0.001	4.000	4000.000
B17	2.254	4.000	10.004	0.001	4.000	4000.000
B18	1.004	4.000	8.004	0.001	4.000	4000.000
C1	0.440	4.000	4.800	0.1	4.000	40.000
C2	0.440	4.000	4.800	0.100	4.000	40.000
C3	0.440	4.000	4.800	0.100	4.000	40.000
C4	3.000	4.000	8.000	0.500	4.000	8.000
C5	3.000	4.000	8.000	0.500	4.000	8.000
C6	3.000	4.000	8.000	0.500	4.000	8.000
C7	8.000	4.000	12.000	1.000	4.000	4.000
C8	8.000	4.000	12.000	1.000	4.000	4.000
C9	8.000	4.000	12.000	1.000	4.000	4.000

contact mask pattern is shown overlaid in red on the device field mask in figure 3.5. We used thermal evaporation to deposit a thin (few nm) wetting layer of chromium and ∼100 nm of gold. A physical mask was then used to deposit larger aluminum back contacts. The samples were finally annealed at ∼100 °C for ∼24 hours. A schematic drawing of a completed silicon nanocrystal floating gate transistor optical memory is shown in figure 3.7.

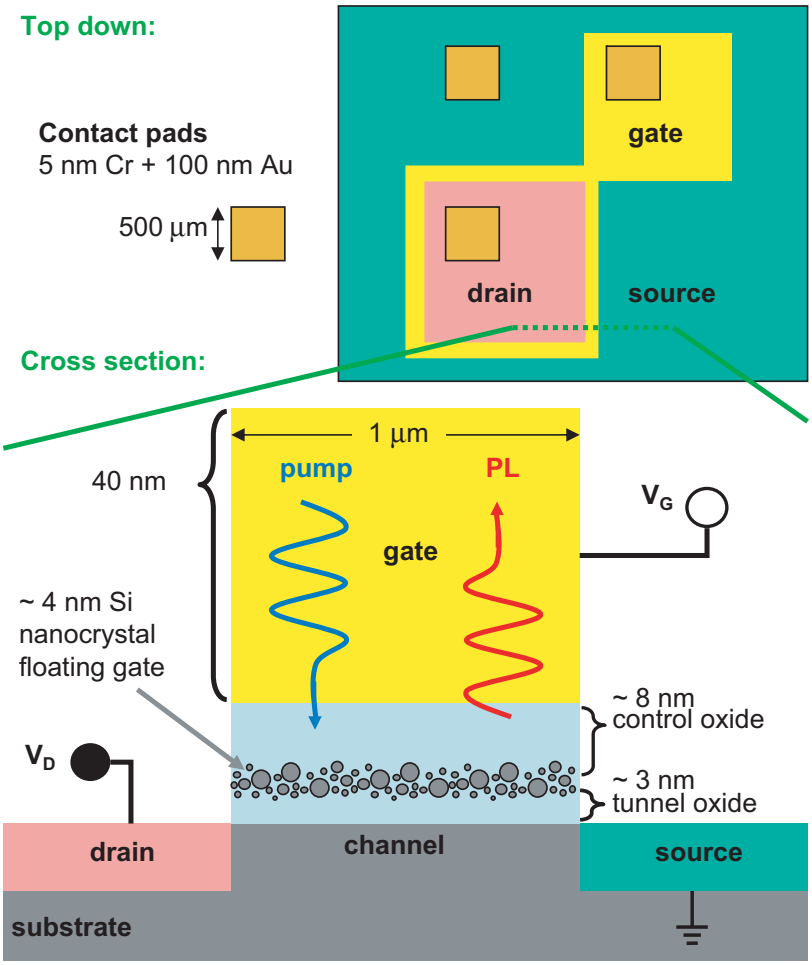

Figure 3.7. A schematic diagram of a silicon nanocrystal optical memory device.

For some experiments, we used tungsten probes to electrically contact the deposited metal pads. In other cases, we packaged the die in 40 pin ceramic dual inline packages using an ultrasonic wire bonder. A picture of a packaged device is shown in figure 3.8. We found that the ceramic packages would luminesce in the same spectral region as the silicon nanocrystals if illuminated by stray laser light, making them less attractive for our photoluminescence measurements.

High resolution transmission electron microscopy in cross section (figure 3.9) can used to confirm the dimensions of the gate stack, although individual nanocrystals are not resolved in the images. This may be attributed to low contrast between silicon and SiO_2 or to the high density of nanocrystals in the sample. The presence of Si nanocrystals in the oxide layer was independently verified using vacuum atomic force microscopy measurements on samples in which the oxide layer of the gate stack was partially removed with buffered

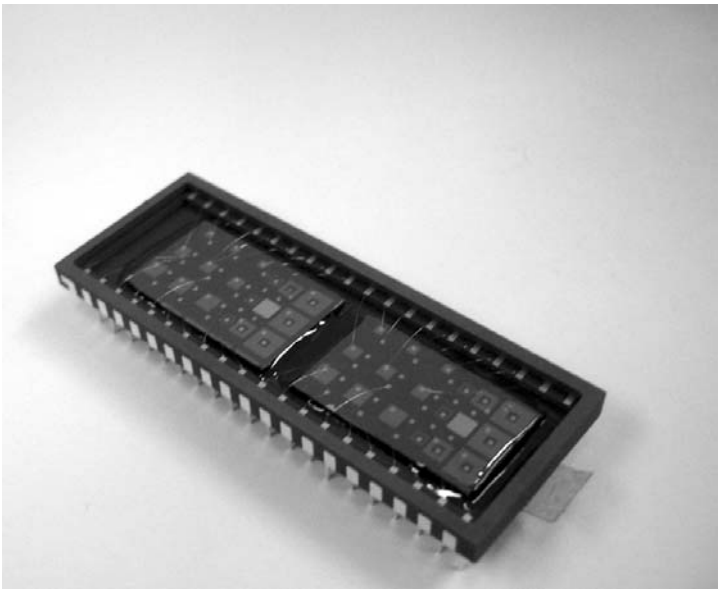

Figure 3.8. Two silicon nanocrystal optical memory die are packaged together in a 40 pin ceramic dual inline package. The devices are from series B and C (see figure 3.6).

HF. From these measurements, we estimate that the nanocrystals forming the floating gate array have an areal density of $\sim 4 \times 10^{12}$ cm^{-2} and are 2–4 nm in diameter. This areal density corresponds to a total silicon content of 20%–80% of the implanted Si dose. The low yield may correspond to a loss of implanted silicon to the substrate during the nanocrystal formation process, or suggest a large density of small agglomerates that are not detected in our measurements.

3.5 Electrical Characterization

We found that our polysilicon gate contacts have a sheet resistance of 182 Ω sq^{-1} which is somewhat higher than usual for CMOS devices ($\sim$33 Ω sq^{-1}) and is high in consideration of the implanted dose of dopant ions. We speculate that the low energy implantation used to avoid inadvertently implanting dopants in the nanocrystal layer may have resulted in an inhomogeneous and relatively shallow distribution of donors in the gate. The most ideal transistor performance characteristics were observed for structures with the smallest gate contact pads (1 mm^2). This might be attributed to perimeter leakage because our transistors do not have isolated gate contacts.

Figure 3.10 shows a typical I–V curve for one of our silicon nanocrystal floating gate

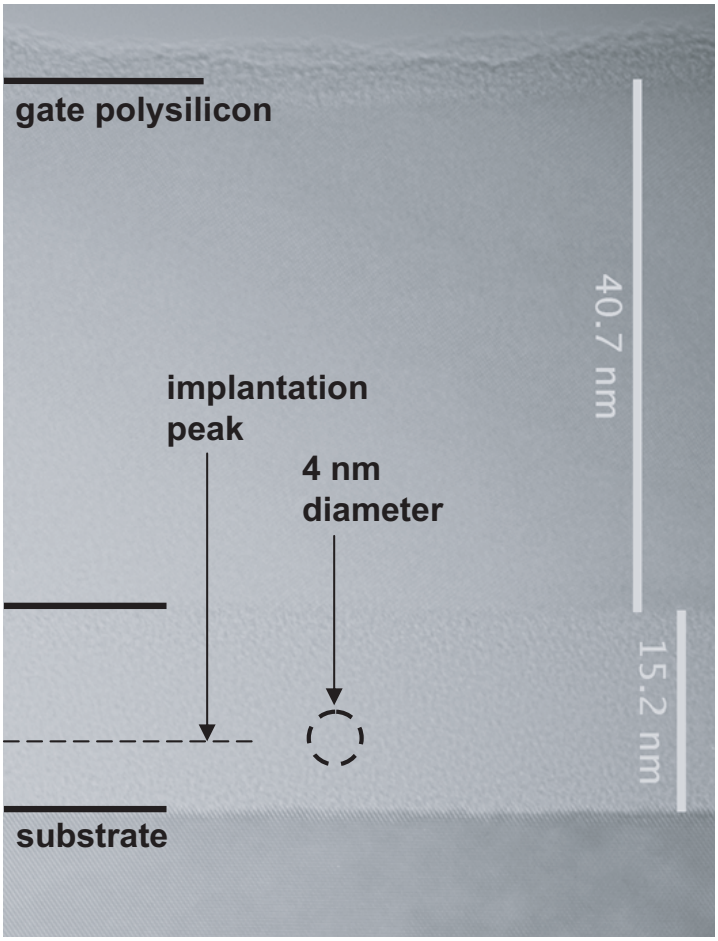

Figure 3.9. High resolution transmission electron microscopy image of the gate stack of silicon nanocrystal floating gate optical memory. Silicon nanocrystals cannot be resolved in the image.

transistors (*B*17). Because our transistors are fabricated on *p*-type substrates, holes gather in the channel under negative gate bias. Under this "accumulation" condition, the electrical connection between the source and the drain forms an *n*-*p*-*n* junction that will not pass a current. This corresponds to the off state of the transistor. At high gate bias, an electron "inversion" layer forms in the channel, turning the device on and allowing current to flow between the source and the drain. The source-to-drain current varies with the applied source-to-drain bias at any particular gate voltage and tends to saturate when the source-to-drain bias is ±2 V. In figure 3.10, the on/off current ratio of the device is $\sim 10^4$, but we have observed ratios in the range from 10^2 to 10^8 among our devices. The transistors seem to be relatively fragile, and the on/off ratio typically decreases after cycling the terminal voltages.

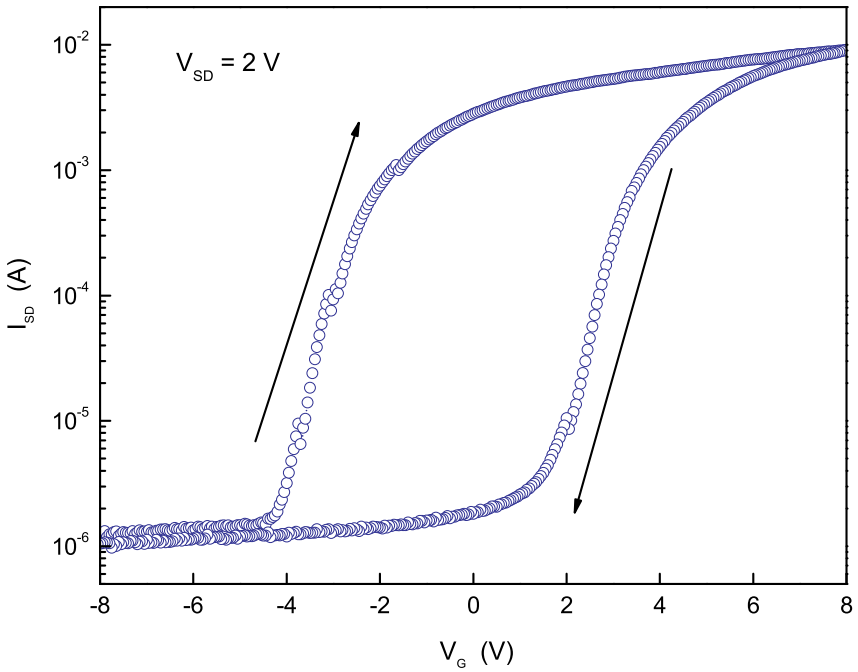

Figure 3.10. A typical transistor IV curve shows the source to drain current as a function of gate voltage for transistor $B17$. The large hysteresis in the measurement is the result of charge injection into the nanocrystal floating gate.

Typical gate leakage currents are on the order of 1 mA/cm^2. Irreversible breakdown of the gate oxide is common for gate voltages above ± 10 V and has been observed at levels as low as ± 7 V.

The steep transition zone between the on and off states of the transistor begins at the flatband voltage and ends at the threshold voltage, when the inversion layer becomes fully formed. We see a pronounced hysteresis in the threshold voltage of the I–V curves, indicating that a large amount of charge is stored in the gate stack of the transistor. The stored charge acts either to complement or to counteract the potential created by the applied gate bias at the surface of the transistor channel, which is why the charge storage reservoir in such a device is referred to as a "floating gate." In figure 3.10, the threshold voltage on the forward gate bias sweep is approximately -2 V. When the gate bias is returned to -8 V, the threshold voltage is observed at ~ 4 V. This is a consequence of the floating gate acquiring a negative net charge during the interval that the large positive gate bias was applied. The negative charge adds a negative bias at the surface of the channel, allowing an accumulation layer of holes to collect in the channel even at small positive gate biases.

The total threshold voltage shift indicated in figure 3.10 is ∼6 V, which is typical of our transistors.

In order to explore charge storage in the nanocrystal array we measure the change in the total capacitance of the gate stack as a function of the applied gate voltage [156]. Beginning in the accumulation regime at negative gate bias, we first measure a capacitance corresponding to the ∼15 nm thick gate oxide layer. We typically find this capacitance is ∼2–5 times smaller than what would be predicted using a simple parallel plate model for the gate oxide. Some fraction of this discrepancy could be related to series capacitance in the gate contact or substrate. As the gate bias is increased, we encounter a gate bias at which the potential at the surface of the channel matches the Fermi level of the substrate and the accumulation layer begins to give way to a depleted zone. The depletion width acts as a second capacitor in series with the gate oxide layer and the capacitance that we measure begins to drop. When the threshold voltage is reached, an inversion layer forms and the depletion width no longer grows. The capacitance stays constant if the gate bias is increased further.

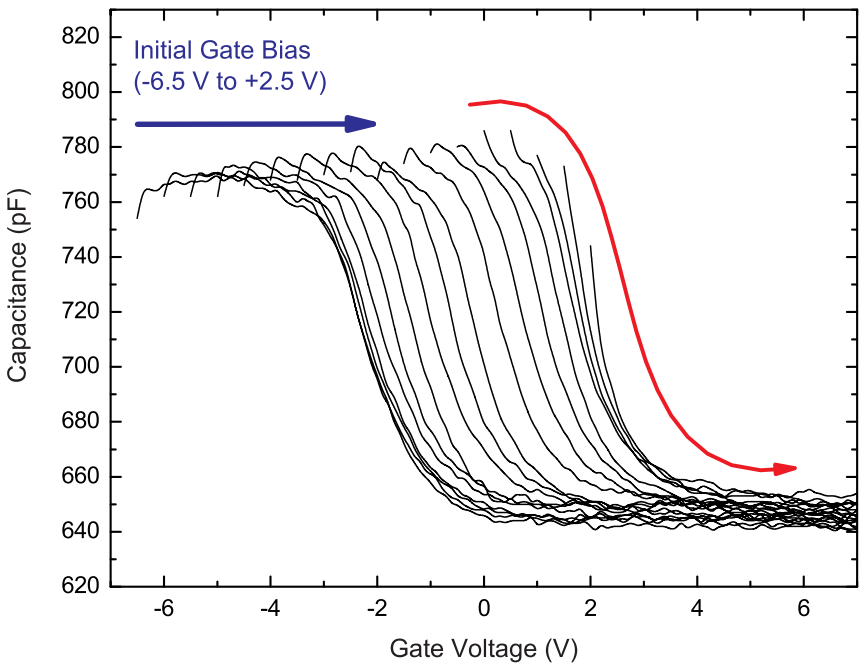

Figure 3.11. Gate capacitance response after programming the floating gate at various negative gates biases at 0.5 V intervals. This measurement demonstrates that the threshold voltage can be set within a broad programming window.

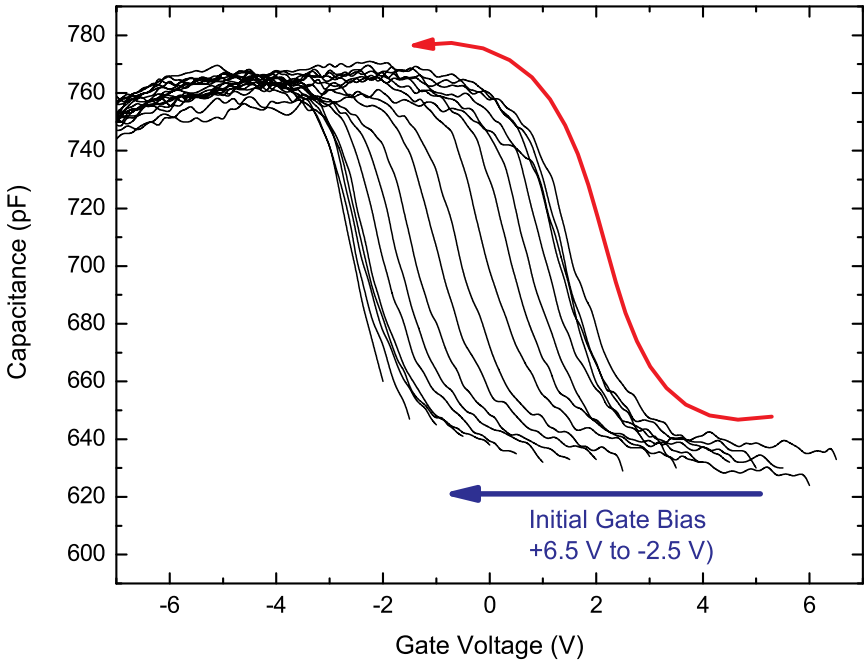

Figure 3.12. Gate capacitance response after programming the floating gate at various positive gate biases at 0.5 V intervals.

Figure 3.11 shows a family of such C–V curves, in which the gate voltage is swept from various negative initial gate bias levels to +7 V. The device is kept at the initial gate bias level for several seconds to allow the charge in the silicon nanocrystal floating gate to equilibrate before each trace is recorded. Note that for each initial gate voltage inside the programming window we observed in our I–V measurements (figure 3.10), we find a different threshold voltage. This confirms that we begin each trace after the charge stored on the nanocrystal floating gate has had time to equilibrate at the first gate bias level. Similar measurements made for initially positive gate voltages are shown in figure 3.12. These measurements demonstrate that the threshold voltage can be shifted continuously through a programming window between about -2 V and 4 V.

A simple delta-depletion model can be used to interpret C–V measurements. For example, the ratio of the accumulation capacitance to the inversion capacitance allows us determine the maximum depletion width. We find that the depletion width saturates at $\sim$50 nm, corresponding to our substrate dopant concentration of $\sim 2 \times 10^{18}$ cm^{-2}. Within this model, we find that a charge density of $\sim 2 \times 10^{12}$ cm^{-2} must be stored on the floating gate to change the threshold voltage by 1 V. We can therefore estimate a maximum

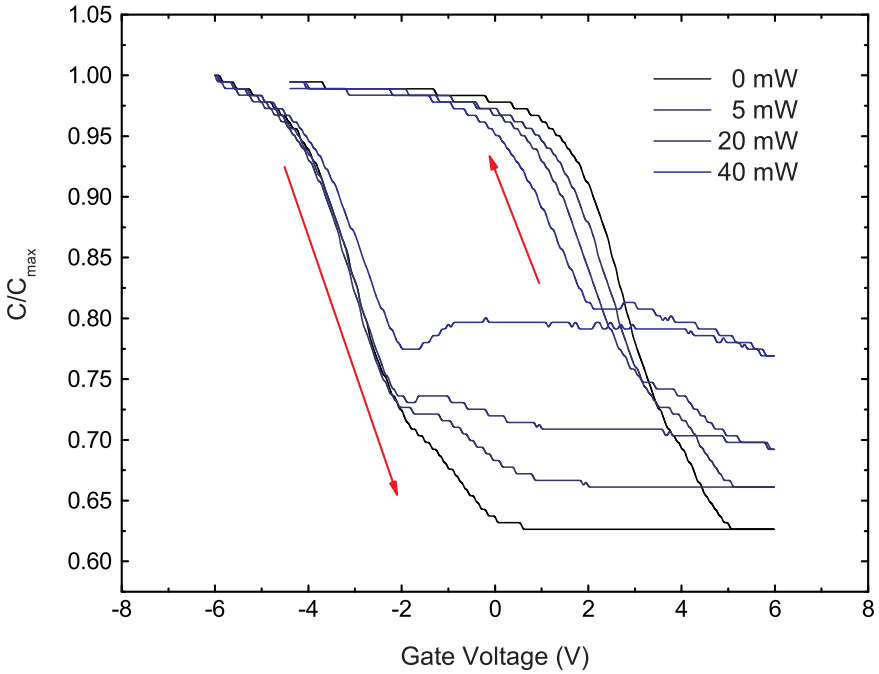

Figure 3.13. The gate capacitance is reduced for inversion conditions under illumination by photoexcited carriers in the substrate. These data are recorded at the same sweep rate as the data shown in figure 3.15.

charge carrier density of $\pm 6 \times 10^{12}$ cm^{-2} in the oxide at the extremes of the programming window. This is approximately equal to the estimated nanocrystal density in the floating gate, and suggests that each nanocrystal is at most singly charged. This corresponds to our expectation that multiple charging of nanocrystals is unlikely because of capacitive charging barriers. However, we cannot distinguish between charge storage on the optically active nanocrystals and charge storage elsewhere in the gate oxide by these electrical measurements.

Figure 3.13 shows hysteresis in the normalized capacitance of the gate stack when the device is illuminated at 457.9 nm by an Ar^+ ion laser during the gate voltage sweep. We can observe the effect of photoexcited carriers in the substrate in the decreasing depletion width capacitance under positive gate bias and strong illumination conditions [157, 158]. The width of the hysteresis loop appears to decrease as the intensity of the laser increases. This demonstrates that some fraction of the charge that is stored in the floating gate is more volitile when the device is illuminated. We suggest that this may correspond to the ejection of charge carriers from silicon nanocrystals by internal photoemission.

3.6 Gate Bias Dependent Photoluminescence

The state of our memory devices can be read optically by monitoring the photoluminescence intensity, which varies according to the average charge state of the nanocrystals embedded in the device. The suppression of photoluminescence in charged nanocrystals is a consequence of fast nonradiative Auger recombination paths by which photoexcited excitons recombine by energy transfer to nearby charge carriers. Auger recombination is thought to be a sub-nanosecond process in charged silicon nanocrystals, in contrast to the ∼10 μs time scale of radiative recombination. Previous observations of photoluminescence "blinking" in isolated CdSe nanocrystals [159] and experiments in chemical systems in which free charge is stored on II–VI nanocrystals via a change in solvent pH [160] confirm that photoluminescence can be suppressed in this way. While Auger recombination is usually considered an undesirable or performance limiting process in nanocrystal optoelectronics, we take advantage of the effect in our devices to intentionally modulate the photoluminescence.

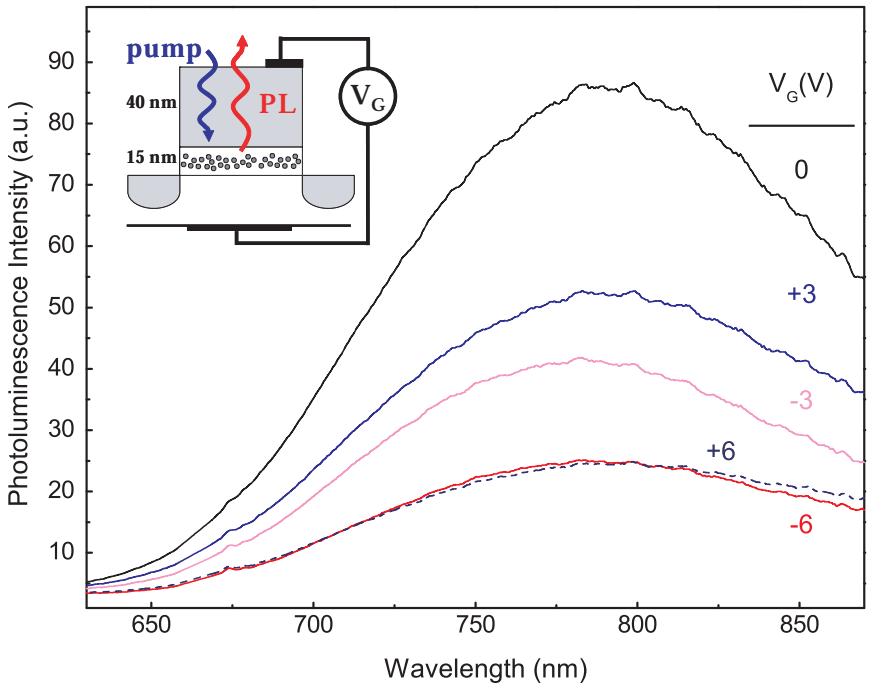

Figure 3.14. The steady state photoluminescence spectra measured at various applied gate biases. The inset shows a schematic of the device indicating the optical addressing of the nanocrystal floating gate through the semitransparent gate contact.

Figure 3.14 shows the steady state photoluminescence spectra of the nanocrystal ensem-

ble in our optical memory device under various applied gate biases. The nanocrystals are pumped using an Ar^+ ion laser at 457.9 nm focused to a $\sim$1 mm^2 spot. A cryogenically cooled CCD array and a grating spectrometer were used to collect the photoluminescence spectra, which were corrected for detector sensitivity, and stray light was removed by optical filters.

The spectra peak near 780 nm with a typical full width at half maximum of 160 nm, which we attribute to inhomogeneous broadening caused by the size distribution of silicon nanocrystals in the floating gate. The steady state intensity of the photoluminescence decreases for both positive and negative applied gate biases. The quenching effect is robust and reversible and we do not observe any change in the modulation amplitude after days of high intensity illumination and frequent voltage cycling. We attribute the suppression of photoluminescence to a decrease in the active fraction of silicon nanocrystals in the ensemble. The dark fraction of nanocrystals preferentially decay by nonradiative Auger recombination in the presence of an extra charge carrier either inside the nanocrystal or at a nearby localized defect trap state in the gate oxide.

At large magnitudes of applied bias, we observe a blueshift in the spectra. We interpret this in terms of the size distribution of nanocrystals within the gate oxide. The nanocrystals that remain uncharged in steady state are likely to be far from the channel where smaller nanocrystals are more numerous than large nanocrystals.

We observe hysteresis in the photoluminescence signal peak intensity at 780 nm that corresponds to the gate voltage range of the programming windows found in I–V and C–V measurements (figure 3.15). The presence of hysteresis in the photoluminescence trace is attributed to the persistent storage of charge in the nanocrystal ensemble. The decrease in photoluminescence is more pronounced for gate voltage sweeps that move from negative to positive bias. This demonstrates that holes are better retained by the silicon nanocrystals than electrons. We attribute this to the difference in confinement potential provided to stored holes and electrons by the valence and conduction band offsets between SiO_2 and silicon ($\sim$4.7 eV vs. $\sim$3.2 eV). The optical hysteresis loop is superimposed on a trend of photoluminescence quenching that is symmetric in gate bias. This component of the photoluminescence quenching is attributed to volatile charge stored in the floating gate on either the nanocrystal array or nearby defect centers that are able to quench photoluminescence.

It should be noted that the width of the hysteresis is diminished at high illumination

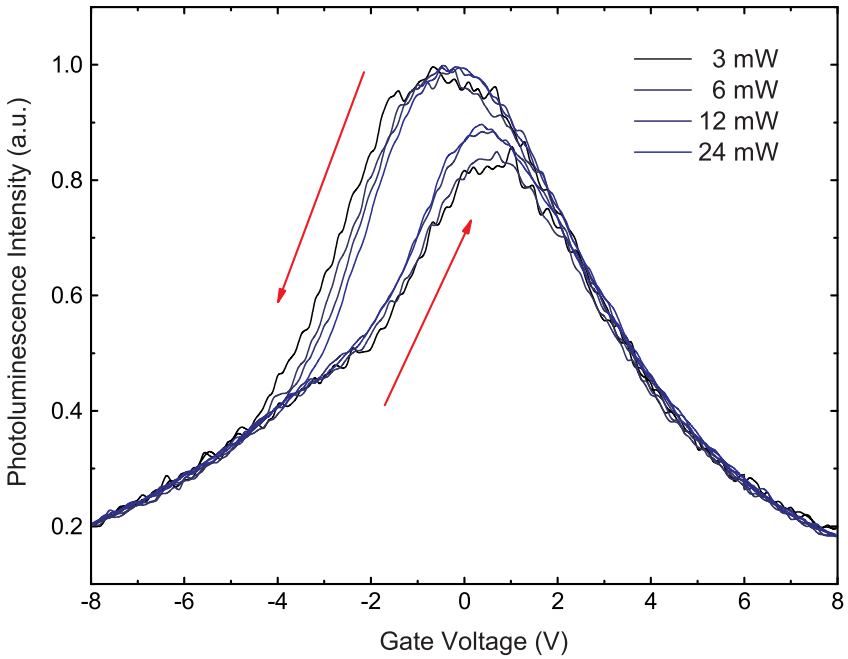

Figure 3.15. An intensity hysteresis loop measured for the peak photoluminescence at 780 nm can be measured at the same gate voltage sweep rate (50 mV/sec) used to collect the C–V traces shown in figure 3.13. The observation of hysteresis is a proof of concept demonstration of data retention in the device.

intensities, suggesting that charging and discharging times are reduced by the presence of light. This may indicate discharging of silicon nanocrystals through internal photoemission or a thermal process. The closure of the hysteresis loop therefore provides evidence for optically assisted programming of our silicon nanocrystal memory device.

We also measured photoluminescence decay at 780 nm for the ensemble of nanocrystals in our optical memory device under constant gate bias (figure 3.16. For these measurements, the nanocrystals were pumped to steady state by the 488 nm line of an Ar^+ ion laser at $\sim$10 W/cm^2. The laser was then abruptly turned off using an acousto-optic modulator. Photoluminescence was collected over a $\sim$50 nm passband using a grating spectrometer coupled to a thermoelectrically cooled photomultiplier tube. Each photoluminescence decay trace was fit to the stretched exponential or Kolrausch decay function (see chapter 2), yielding experimental decay lifetimes ranging from 4 to 9 µs with the β parameter held constant at 0.7. Here the photoluminescence data were recorded after the charge state of the nanocrystal ensemble reached equilibrium. Presumably the decay lifetime data would

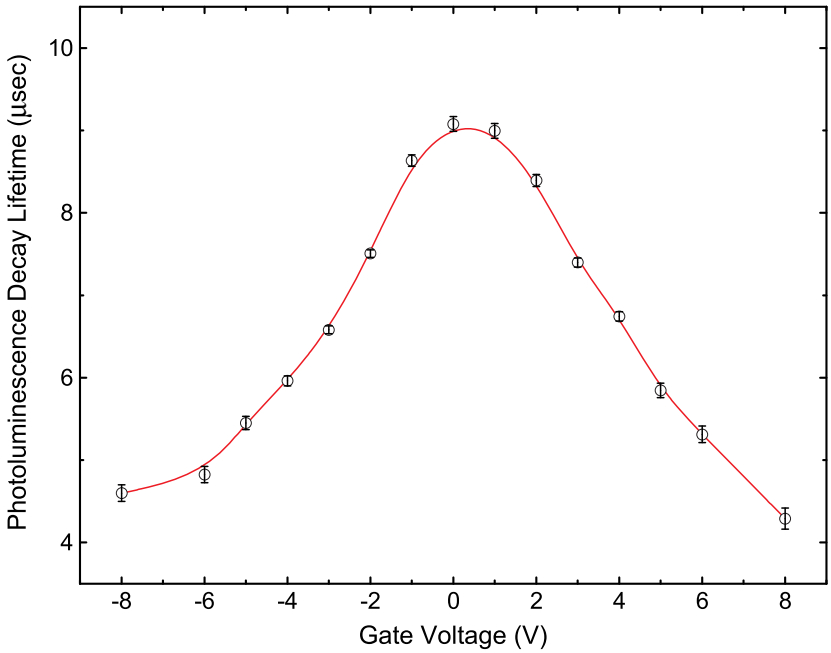

Figure 3.16. The steady state photoluminescence decay lifetime for the silicon nanocrystal ensemble in our optical memory decreases as a gate bias is applied to the device.

also show hysteresis if the gate bias voltage was swept rapidly.

The reduction in the decay lifetime in proportion to the gate bias may be a signature of energy exchange between nanocrystals. Charged nanocrystals rendered "dark" by Auger recombination do not contribute to the recorded photoluminescence decay lifetime traces directly, but may introduce indirect nonradiative recombination pathways to the ensemble by quenching any excitons that are transferred to them. In this model, indirect quenching through energy transfer becomes about as likely as radiative decay at the extremes of the applied gate bias, as the experimental photoluminescence decay lifetime is reduced by a factor of two.

3.7 Photoluminescence Transient Response

To further investigate the time scale of charge retention in our optical memory devices, we recorded photoluminescence transient response curves, in which the photoluminescence intensity is monitored at the peak of the spectrum at 3 second intervals, while the bias condition is stepped from 0 V to a particular gate bias for several minutes and then returned

to 0 V. Figure 3.17 shows a series of photoluminescence intensity data recorded for such an experiment over several hours. The transient response curves averaged over 10 measurements and normalized to the initial steady state photoluminescence intensity for clarity are shown in figure 3.18 at several illumination intensities.

Charge injection is abrupt on the time scale of our measurement (3 seconds) at gate biases other than -3 V. The slow injection of holes at this low negative gate voltage is correlated to the persistent decrease in photoluminescence seen in figure 3.15. The dependence of the photoluminescence quenching transient response on the illumination level suggests that the photoexcitation of carriers in the channel may assist in the hole injection process. When the gate bias is returned to 0 V, the photoluminescence intensity remains quenched longer if the memory is programmed using a negative gate bias. This is consistent with hole storage being less volatile than electron storage.

We can see from the transient response curves that illumination at high intensity reduces memory retention times. This effect is attributed to optical nanocrystal erasure via internal photoemission, as indicated in the inset band diagrams of figure 3.18. The efficiency of the photoemission erasure mechanism should increase with increasing excitation photon energy. Thus we would expect data retention to be maximized for the case of resonant excitation, which would be the least destructive read operation possible. Under low power illumination at 457.9 nm, a noticeable change in the photoluminescence intensity is retained for ∼10–100 seconds.

3.8 Photoluminescence Modulation

In our transient response measurements, we found that photoluminescence was abruptly quenched in response to an applied gate bias. We began a series of experiments designed to measure the response of our optical memory devices at much shorter time scales. In this case, we are interested in the possibility of creating an optical modulator that takes advantage of the rapid Auger recombination rate in charged nanocrystals.

We found that photoluminescence could be modulated at speeds up to a few 100 kHz (figure 3.19). The limiting time scale is the decay rate of the nanocrystals that are not charged by the applied gate bias. In an ideal device, all of the nanocrystals would be simultaneously charged and the fall time of the modulator would be determined by either

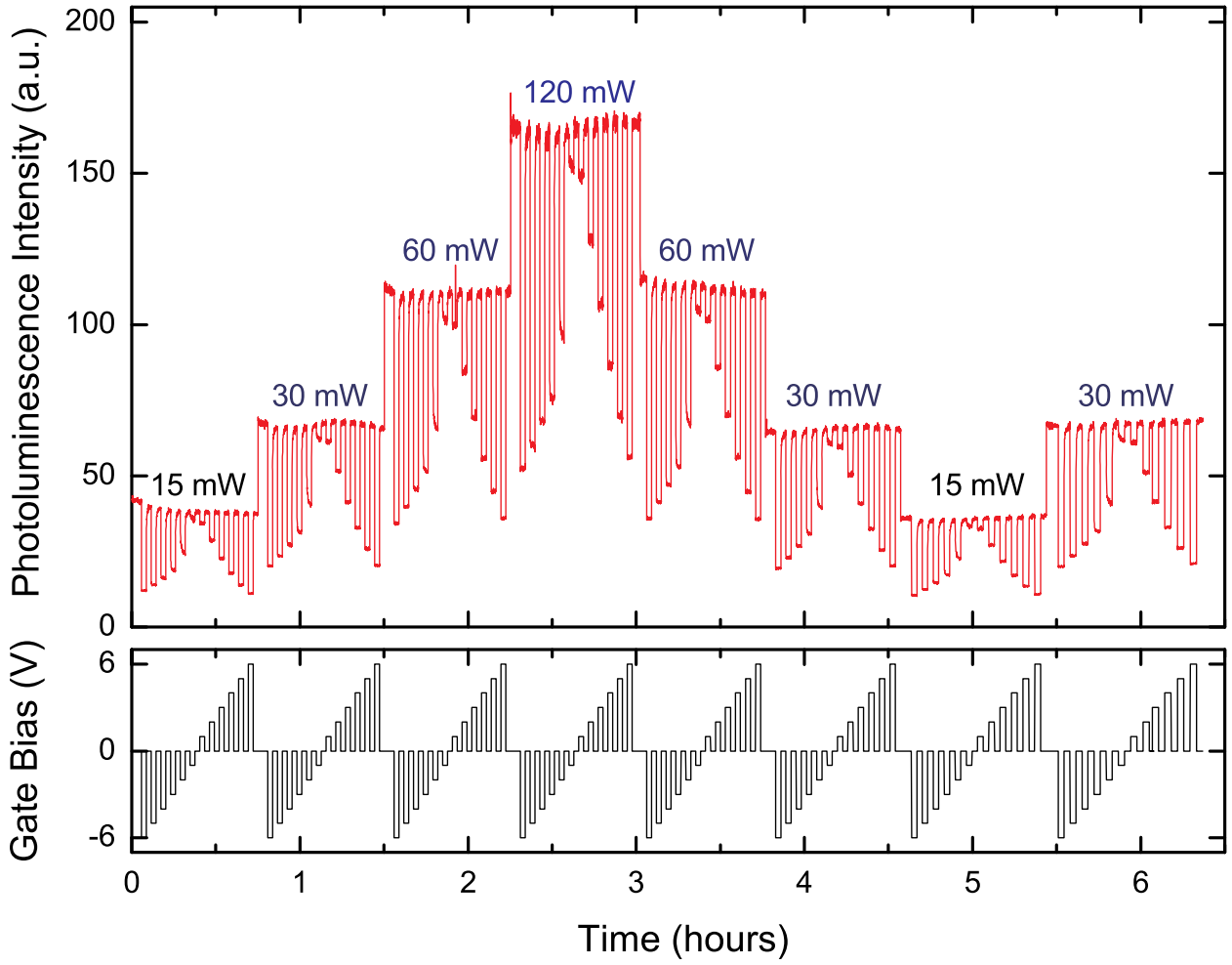

Figure 3.17. The transient response of the optical memory device to step input changes in voltage is monitored over long time scales in an automated measurement. Data are recorded at 3 second intervals.

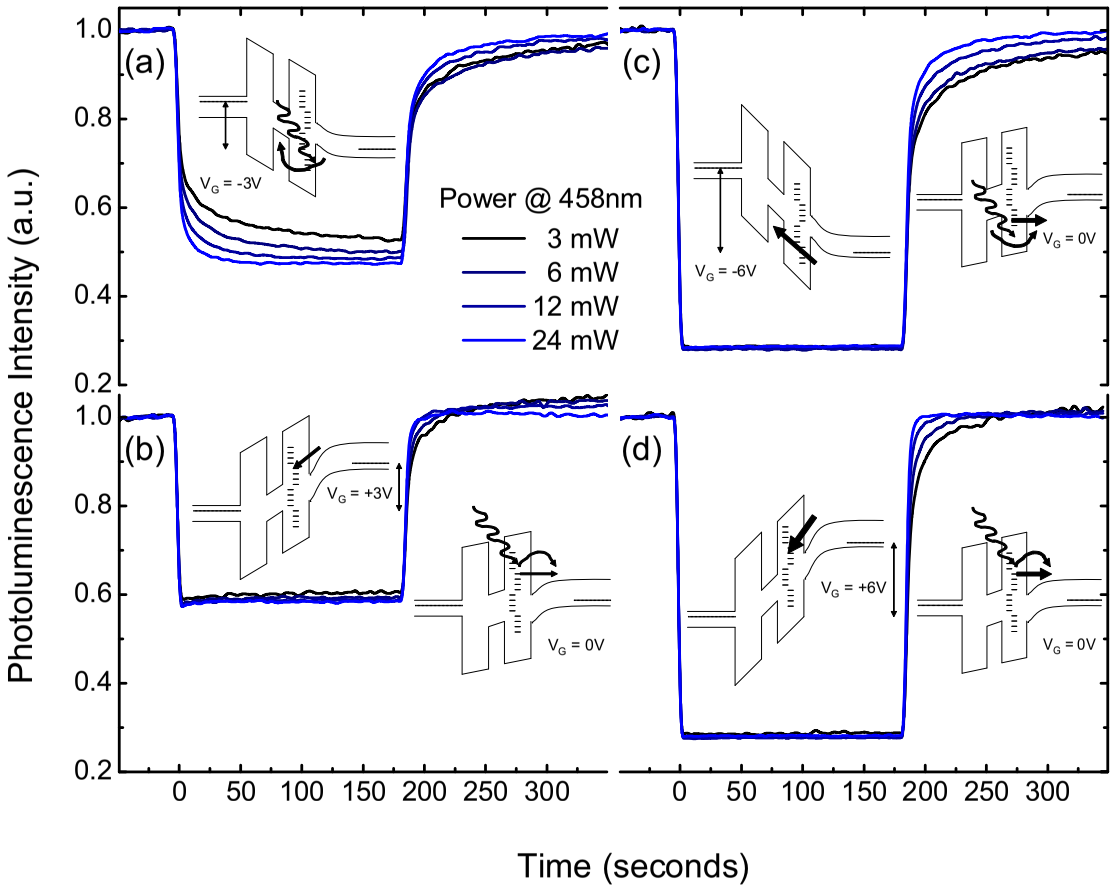

Figure 3.18. The transient photoluminescence intensity response to abrupt changes in gate bias at different excitation powers. The gate bias is switched off after 3 minutes and photoluminescence quenching persists for a characteristic retention time (∼10–100 seconds), depending on the optical excitation strength and the charging voltage. The inset band structures schematically illustrate relevant charge transfer processes.

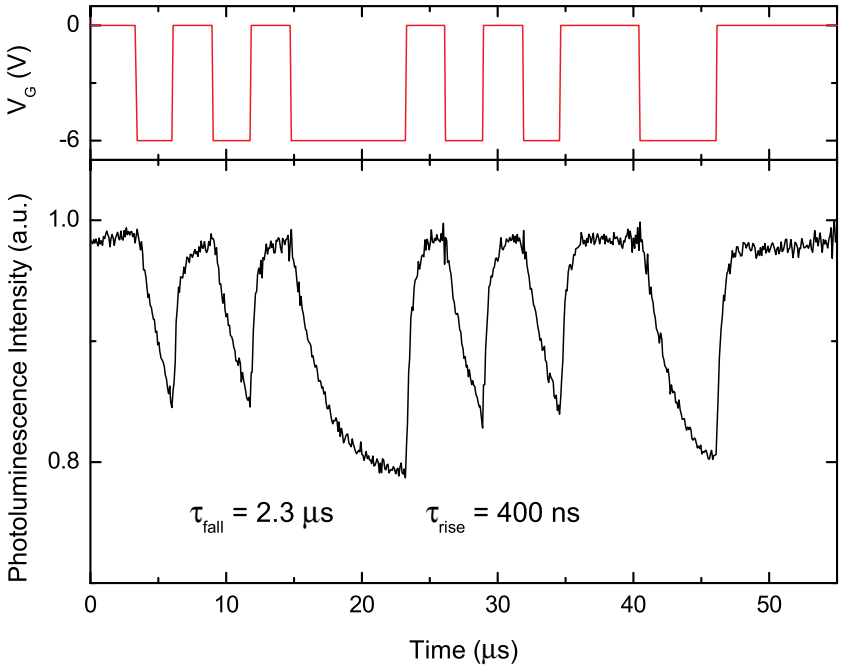

Figure 3.19. Si nanocrystal photoluminescence intensity response to high speed gate bias modulation.

the injection time for the charge carriers or the Auger recombination rate. The rise time would be limited by the time required to flush the stored charge from the floating gate of nanocrystals or by the excitation rate of the nanocrystals if the illumination intensity was limited.

Our investigation of the optical memory devices under rapid transitions in gate bias led to an unanticipated discovery. With the pump beam power decreased in an attempt to measure an excitation rate limited rise time, we were unable to satisfactorily normalize the photoluminescence data. An anomalous overshoot seemed to be present that had not been observed at higher pump intensities. During the effort to find the source of this unwanted signal so it could be eliminated, we finally tried turning the laser off for a portion of the photoluminescence trace and clearly observed electroluminescence for the first time (figure 3.20). The next chapter describes this phenomenon, which we call *field-effect electroluminescence*, in detail.

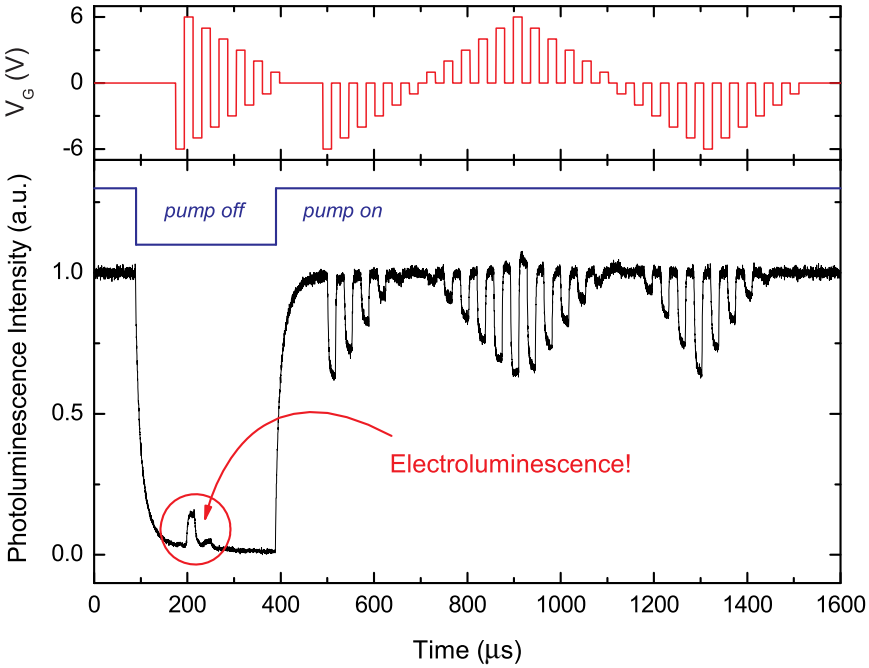

Figure 3.20. Our first observation of field-effect electroluminescence (measured at 740 nm). The photoluminescence signal is pumped by 458 nm light at ~100 W/cm^2.

3.9 Conclusion

In this chapter we described the fabrication and operation of a CMOS compatible optical memory device, in which a dense ensemble of silicon nanocrystals comprise a floating gate for a transistor. The programmed logic state of the device can be read optically by the detection of high or low photoluminescence intensity. We correlate the change in the silicon nanocrystal photoluminescence to the electrical characteristics of the device. The quenching of photoluminescence is attributed to the onset of nonradiative Auger recombination in the presence of free charge carriers injected into the floating gate. The device can be programmed and erased electrically via charge injection and optically via internal photoemission. Photoluminescence suppression of up to 80% is demonstrated with data retention times of order 100 seconds at room temperature.

Chapter 4

Field-Effect Electroluminescence

4.1 Introduction

This chapter presents evidence for a novel electroluminescence mechanism that we call *field-effect electroluminescence*. In this process, excitons are created in silicon nanocrystals by the sequential injection of complementary charge carriers from a semiconductor channel. In contrast to previously reported light emitting diodes, a *field-effect light emitting device* (FELED) is excited by an alternating gate voltage rather than a constant current through the device. Our approach offers a new conceptual paradigm for electrical excitation in quantum dots.

We demonstrate that the emission characteristics of our prototype devices are most likely limited by the charge injection processes that store first carriers in neutral nanocrystals. Using the observed experimental time constants, we are able to qualitatively reproduce field-effect electroluminescence using a coupled state master equation simulation. Finally, we discuss the anticipated performance limits for optimized field-effect light emitting devices.

4.2 Silicon Nanocrystal Electroluminescence

There is a widespread interest in silicon nanocrystals as an optoelectronic material system for light emitting devices [20]. In comparison to bulk silicon, nanocrystals exhibit a tunable emission energy and increased oscillator strength due to the quantum confinement of excitons. Low nonradiative recombination rates observed for well-passivated silicon nanocrystals embedded in silicon dioxide lead to a very high internal photoluminescence quantum efficiency in spite of the relatively slow radiative recombination rates [115]. In chapter 2 we have demonstrated that this desirable property is maintained in dense nanocrystal ensembles, suggesting that devices might operate at high output conditions without significantly

reduced efficiency.

However, the insulating matrix that defines a nanocrystal makes efficient electrical carrier injection challenging. Consequently, the operating efficiencies of previously reported electrically pumped silicon nanocrystal light-emitting devices have been relatively low [102, 161–166]. The development of more efficient electrical pumping methods is a critical challenge for the improvement of silicon nanocrystal based optoelectronic devices.

In this chapter, we describe a new class of field-effect light-emitting devices (FELEDs) that rely on the charge storage capability and optical emission properties of semiconductor nanocrystals. Under appropriate gate bias conditions, the nanocrystal array can be programmed with electrons from an inversion layer or with holes from the channel in accumulation. As shown schematically in figure 4.1, excitons can be formed by sequentially programming the nanocrystals with charge carriers of each sign, resulting in electroluminescence at transitions in gate bias. This approach is a departure from previous carrier injection schemes in which nanocrystals are excited by a constant electrical current.

FELEDs may offer significant advantages over diode-based designs for nanocrystal light sources by enabling precise control over carrier injection processes. For example, durability can be maintained by exciting nanocrystals without resorting to impact ionization processes, in which excess hot carrier energy can result in oxide wearout and eventual device failure [167]. It should also be possible to carefully balance the injection of electrons and holes in order to minimize wasted carrier transport energy. This offers the potential for power-efficient operation in an optimized FELED structure. The external power efficiency of our prototype devices has been limited by gate leakage currents, but this represents an engineering challenge rather than a fundamental limit for performance. Finally, lower voltage operation may be possible in comparison to devices that rely on current flow through a layer of oxide-embedded nanocrystals.

4.3 Field-Effect Light Emitting Device (FELED)

4.3.1 Device Fabrication

A detailed description of the fabrication process for our silicon nanocrystal optical memory devices is given in section 3.4. We use the silicon nanocrystal floating gate transistor devices from these samples for our electroluminescence experiments. Using the naming convention

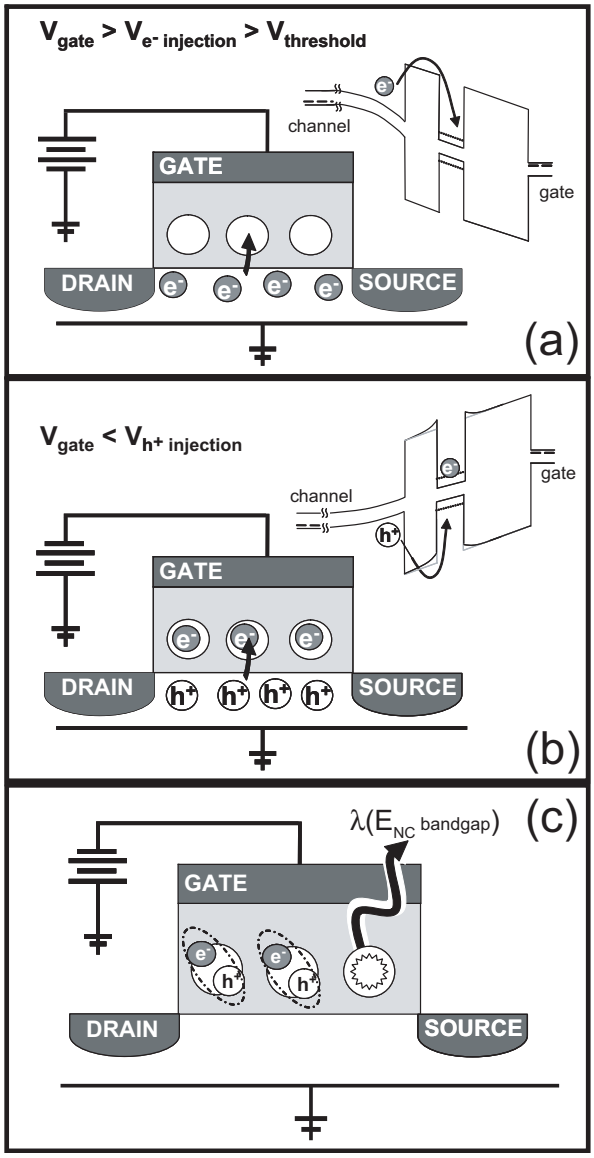

Figure 4.1. This schematic diagram shows the field-effect electroluminescence mechanism in a silicon nanocrystal floating gate transistor structure. Inset band diagrams depict the relevant injection processes. The array of silicon nanocrystals embedded in the gate oxide of the transistor is charged sequentially with electrons (a) and holes (b) to prepare excitons that radiatively recombine (c).

given in figure 3.6, the measurements presented in this chapter correspond to devices $B1$, $B2$, and $B3$.

A schematic of our light emitting device is shown in figure 3.7. The structure resembles a nanocrystal floating gate transistor memory with two important distinctions [152]. First, the floating gate array of silicon nanocrystals is formed from well-passivated silicon nanocrystals, which are small enough to have emission energies that are higher than the bulk silicon emission energy due to carrier confinement. Second, the gate contact has been designed to be substantially transparent at the emission wavelength of the device (∼780 nm) while providing a uniform potential for control of the transistor channel.

The majority of the sample fabrication was performed at a 300 mm wafer development facility at Intel Corporation. This required all processes used in the fabrication of our prototype devices to be selected first for CMOS compatibility. Therefore, an ion implantation based approach was chosen to prepare the silicon nanocrystal layer despite several known nonidealities that such a fabrication method introduces. These undesirable consequences include the inhomogeneous distribution of the nanocrystal sizes and positions within the gate stack and possible degradation of the tunnel oxide layer. Ion implantation damage can be substantially repaired by high-temperature annealing, however, both the duration and temperature of our nanocrystal-formation annealing step were limited by the constraints of the rapid thermal annealing (RTA) tool used in the fabrication process.

Some electroluminescence measurements were made using sample die that were mounted in a gold wire-bonded package, as shown in figure 3.8. We found that these ceramic dual-inline packages emit near-infrared photoluminescence in approximately the same wavelength range as silicon nanocrystals when excited by scattered pump light. This made the packaged devices less convenient for our photoluminescence experiments but did not affect the electroluminescence measurements.

4.3.2 Method

A 20 MHz arbitrary function generator with an output termination of 10 MΩ was used to electrically pump the packaged devices, while an Ar^+ ion laser operating at 457.9 nm was used for optical excitation. Spectra were collected by a grating spectrometer and a cryogenically cooled charge-coupled device (CCD) array. Stray light was removed by optical filters and all spectra were corrected for detector sensitivity. Time resolved electroluminescence

traces were collected with a thermo-electrically cooled photomultiplier tube and a grating spectrometer. The overall system time resolution was ∼10 ns. Time resolved signals are the integrated emission over a passband of approximately 50 nm centered at the emission peak of 780 nm.

4.3.3 Experiment

Figure 4.2 shows a comparison of the nanocrystal photoluminescence pumped through the semitransparent gate contact and nanocrystal electroluminescence excited through field-effect electroluminescence. We attribute these spectra to the radiative recombination of excitons within the silicon nanocrystals. Both the photoluminescence and the electroluminescence spectra peak near 780 nm with full width at half maximum of ∼160 nm. These emission spectra are typical for silicon nanocrystals fabricated by ion implantation. The width of the spectra is attributed to inhomogeneous broadening due to the size distribution of silicon nanocrystals in the array.

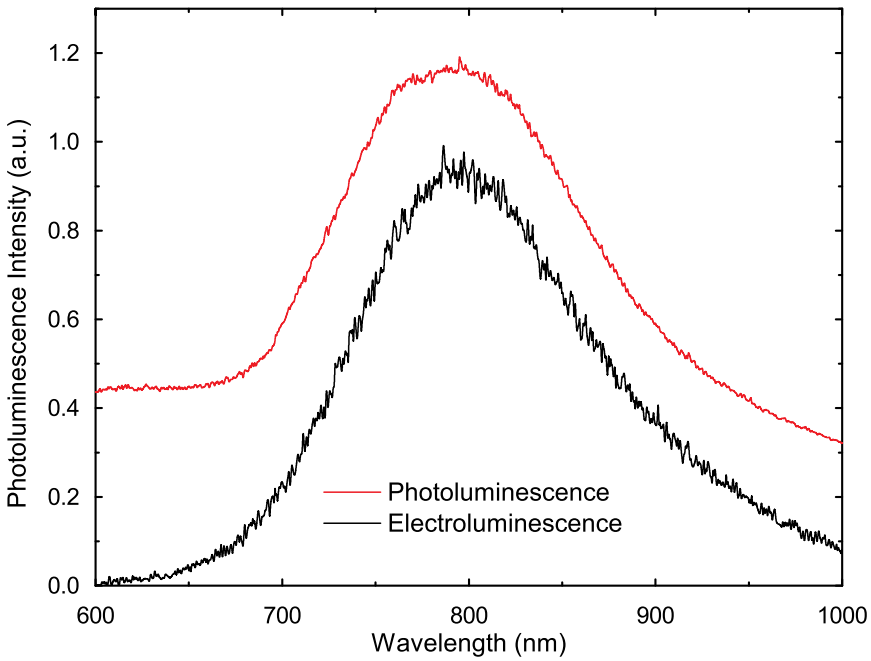

Figure 4.2. The spectra of the silicon nanocrystals are similar for electroluminescence (6 V_{RMS}, 10 kHz) and photoluminescence (457.9 nm, ∼50 W/cm^2; data are shown uniformly offset by 0.25). In both the cases, the output is attributed to the recombination of the confined excitons within the silicon nanocrystals of the active layer.

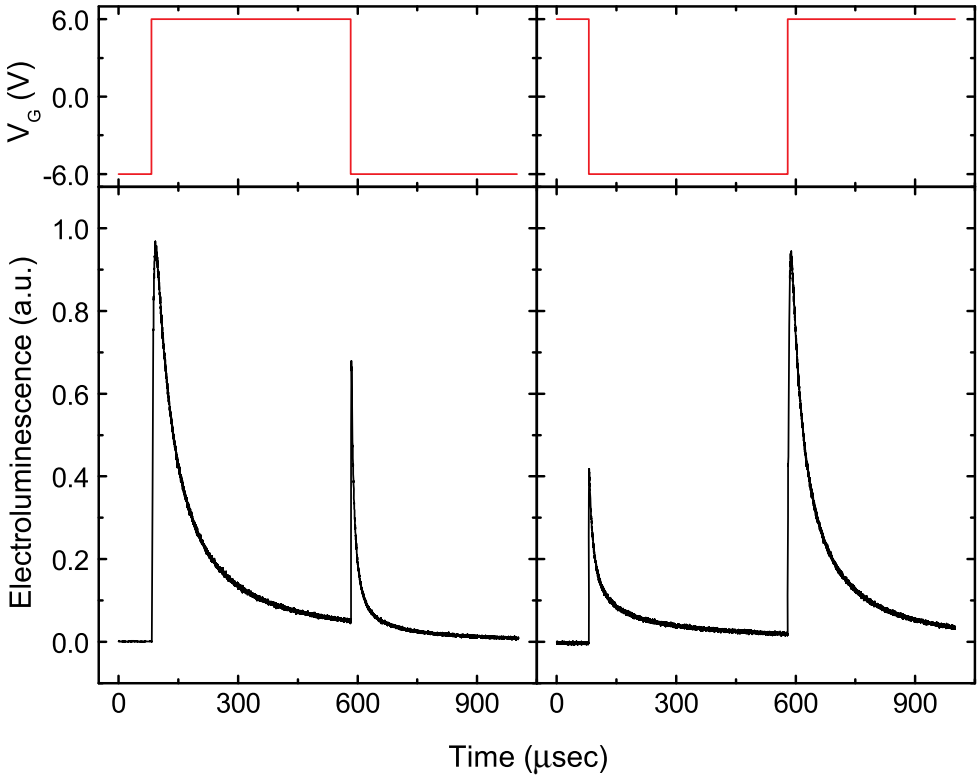

Figure 4.3. Time-resolved electroluminescence traces demonstrate the correlation between light emission and gate bias transitions that correspond to sequential programming events in a FELED.

The electrical excitation process can be understood in more detail by considering the time-resolved electroluminescence trace shown in figure 4.3. Under negative gate bias, the *p*-type channel is in strong accumulation. During this time, the nanocrystal array becomes charged with holes. When the gate bias is abruptly changed to a positive voltage above threshold, an electron inversion layer is formed. Electrons enter the hole charged nanocrystals via a Coulomb field-enhanced injection process, forming quantum-confined excitons that can recombine to emit light. The onset of electroluminescence is well fit by a single exponential rise ($\tau = 2.5$ μs) at the applied 6 V gate bias.

Note that the observation of electroluminescence necessarily implies that the holes that were previously injected into the nanocrystals have an emission time for returning to the channel that exceeds the Coulomb-enhanced injection time for electrons from the inversion layer. Electroluminescence also implies that most nanocrystals are charged with single carriers during the initial charge-injection process, because the presence of an additional

electron or an extra hole in an excited silicon nanocrystal would result in a rapid deexcitation through a nonradiative Auger process.

After the gate bias is switched from a negative to a positive level, the emission pulse rises to a peak value and then begins to decay as the previously injected holes are consumed by electrons in exciton formation and recombination. Some fraction of the stored holes may also be ejected from the nanocrystals before forming excitons. A stretched exponential with a time constant of approximately 30 μs ($\beta = 0.5$) can be used to describe the observed decay. This time constant is longer than the photoluminescence decay lifetimes observed for the samples under optical excitation at the same applied gate bias of 6 V ($\tau = 5$ μs, $\beta = 0.7$). The longer time scale for electroluminescence decay might reflect an absence of some nonradiative recombination paths that are present under illumination. Indirect charging processes involving internanocrystal carrier migration are also likely to play a role in increasing the electroluminescence time constant by extending the time scale for exciton formation. Some fraction of the exciton population may be formed by charge carriers that migrate between nanocrystals in the ensemble rather than by direct carrier injection from the channel. When the electroluminescence signal is no longer observed, there are no holes left in the nanocrystal ensemble to form excitons. However, electrons continue to be injected into the nanocrystal array due to the positive gate bias, resulting in each nanocrystal becoming recharged with an electron.

When the gate voltage is switched back to a strong negative potential, an accumulation layer forms in the channel and holes enter the (now electron-charged) nanocrystals, forming excitons. The electroluminescence pulse associated with this injection process is characterized by a faster single exponential rise-time constant ($\tau = 240$ ns) and a faster stretched exponential decay process ($\tau = 10$ μs, $\beta = 0.5$) in comparison to the rising-gate-voltage electroluminescence pulse.

The pulse of electroluminescence associated with hole injection into electron-charged nanocrystals is smaller in magnitude and shorter in duration than the peak associated with electron injection into the hole-charged nanocrystals. This asymmetry may be attributed to the back-tunneling of electrons to the channel during the hole injection process. The loss of stored charge carriers may be more apparent for electrons than holes due to the smaller conduction band offset (∼3.2 eV) than valence band offset (∼4.7 eV) between the silicon nanocrystals and SiO_2.

Electroluminescence is clearly observed to be correlated with transitions in gate bias, suggesting that emission is not caused by impact ionization that might result from a leakage current through the gate stack. As additionally shown in figure 4.4, emission occurs only for bias transitions between complementary gate voltage levels for which the proposed sequential injection process could occur.

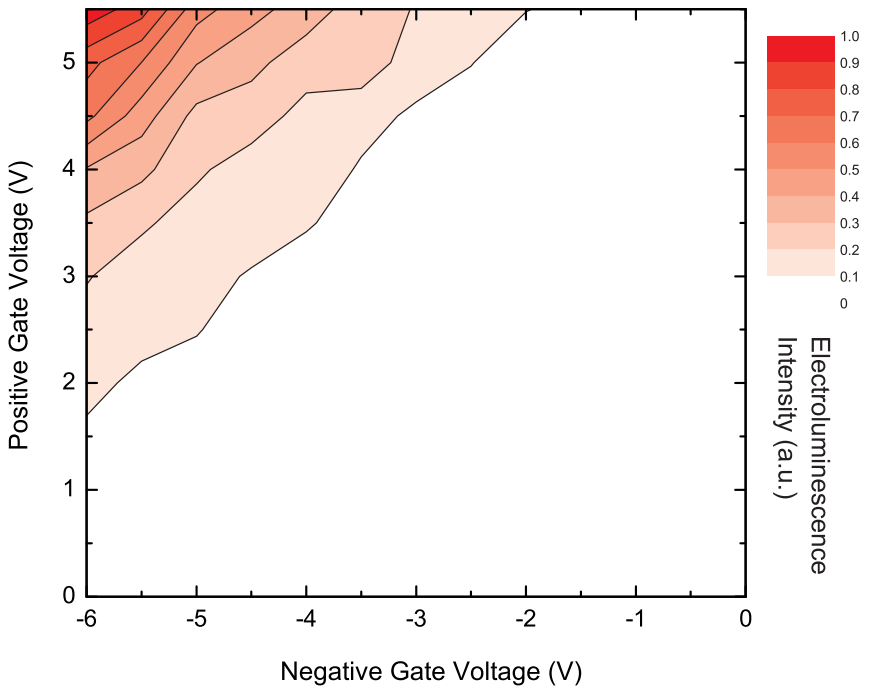

Figure 4.4. Electroluminescence is observed only for transitions in the gate bias for which a sequential complementary charge injection is expected to occur. Values are the average electroluminescence intensity recorded in a time-resolved measurement. The driving gate frequency was held constant at 10 kHz, while the amplitude and offset of the waveform was changed.

The lack of emission under DC electrical bias is further confirmed by an examination of the frequency dependence of electroluminescence (figure 4.5). As the measurement time is held constant at 2 seconds, a linear rise in electroluminescence is initially observed with increasing driving frequency because light is collected from a greater number of integrated complete cycles. Electroluminescence emission peaks at a frequency of ∼10 kHz, and then begins to decrease, which we attribute to a combination of effects. We believe that the ∼10 kHz peak in the frequency response corresponds to a performance-limiting charge

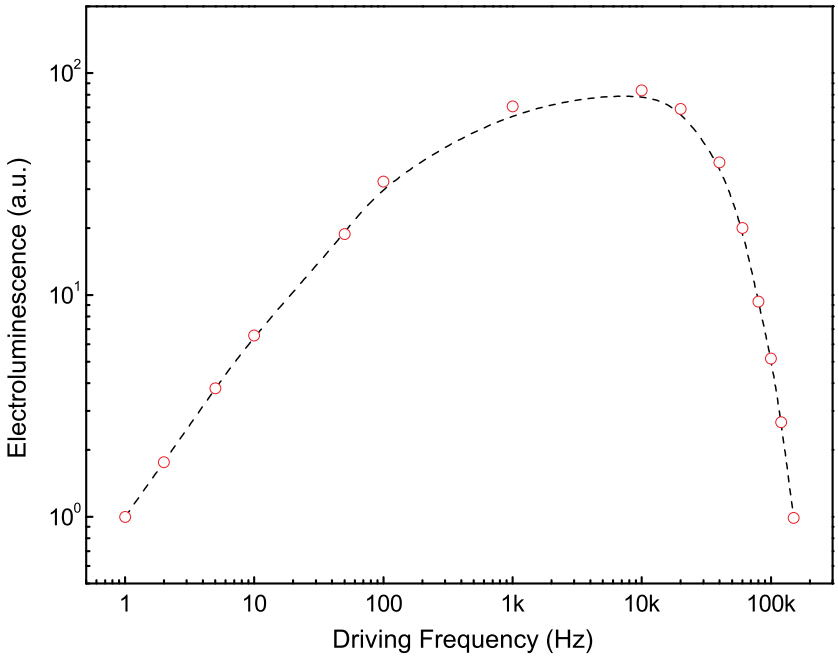

Figure 4.5. The electroluminescence intensity varies with the driving modulation frequency of the applied gate voltage (6 V_{RMS}).

injection time scale for storing first carriers in neutral nanocrystals (∼50 μs). This charge injection time may be associated with a tunneling rate or with the capacitive charging time constant for the device. This hypothesis is supported by the variable charging pulse length experiments discussed in section 4.5. At frequencies above ∼30 kHz, the pulse duration will be shorter than the radiative lifetime of the silicon nanocrystals and some of the excitons will not recombine due to the statistical nature of spontaneous emission. Presumably, this population of excitons is lost to Auger processes when additional charge is injected during the next cycle.

The source and drain regions of the FELED are typically held at ground during electroluminescence measurements. This allows minority carriers to flow laterally into an inversion layer from the source and drain regions and rapidly change the electron density in the channel. The drift velocity of electrons is estimated to be ∼1 mm/μs [168]. A capacitor-based light-emitting device with an identical gate stack could be limited by the minority carrier generation and recombination times. Light emitted from our FELED (device $B3$) under 10 kHz excitation appears spatially uniform over the entire gate stack area, including the 1 mm^2 contact pad area from which light is most conveniently collected using free-space

optics. It is possible that some portion of the high frequency roll off in the electroluminescence signal is due to an incomplete formation of the inversion layer because of the finite drift velocity.

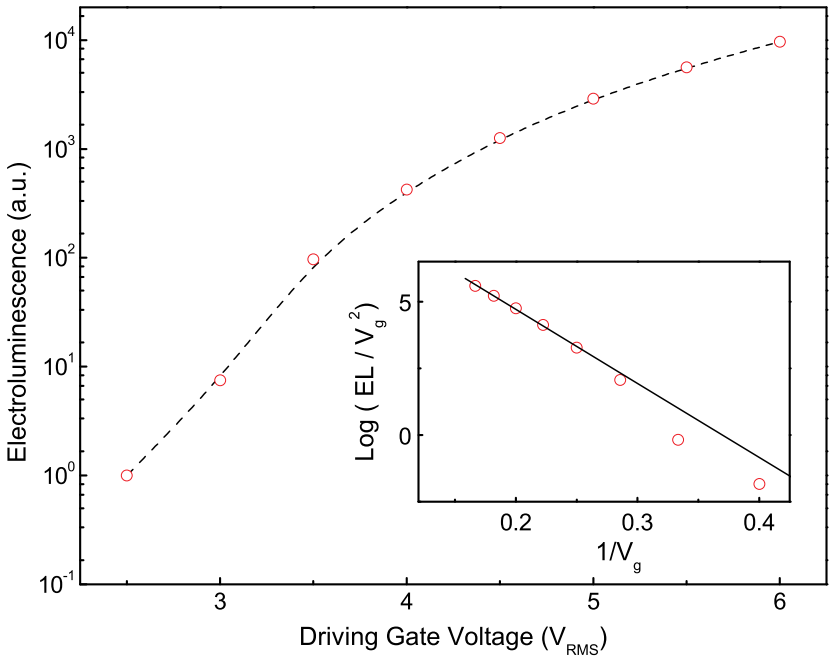

Figure 4.6. The electroluminescence response is a strong function of the driving gate voltage (driving frequency = 10 kHz). An equivalent Fowler-Nordheim plot can be constructed (inset) indicating that Fowler-Nordheim tunneling may be the injection mechanism.

As can be seen in figure 4.6, electroluminescence increases dramatically with increasing RMS drive voltage. The field across the tunnel oxide is approximately proportional to the gate voltage and the magnitude of the electroluminescence signal is proportional to the tunneling current. Thus, we can construct an equivalent Fowler-Nordheim plot (figure 4.6, inset) that follows a linear trend. This suggests that electron or hole injection into the nanocrystals could occur through Fowler-Nordheim tunneling. Electrostatic modeling (section 4.8) suggests that the tunneling bias between the channel and the nanocrystals is typically ~1.3 V for a gate bias of 6 V. In order for tunneling to be dominated by the Fowler-Nordheim mechanism at these low voltages, the tunnel oxide thickness must be less than ~4 nm. This range is consistent with the oxide thickness targeted in our fabrication process.

4.4 Spectral Variation in Frequency Response

The intensity of light output in a FELED scales in proportion to the frequency of the gate bias modulation as long as the device reaches equilibrium during each stage of the field-effect electroluminescence process. The optimal driving frequency is therefore an important parameter for characterizing the performance of a FELED. We typically find a peak in electroluminescence between 5 kHz and 30 kHz, depending on the device and the excitation conditions. We associate this optimal driving frequency with the injection time required to store first carriers in neutral nanocrystals prior to each gate bias transition.

The optimal driving frequency decreases when the device is driven at low gate voltages. Samples with gate contacts that are intentionally etched to reduce the polysilicon thickness also exhibit reduced optimal driving frequency. This suggests that the gate capacitance time constant may impact the charge injection time scale when the gate contact resistance is high. In general our observations correspond to our expectation that charge injection should be a strong function of the potential difference between the channel and the nanocrystal ensemble, as well as the density of charge carriers in the channel.

Variation in the optimal driving frequency is observed at different emission wavelengths. Figure 4.7 shows the electroluminescence intensity emitted by a FELED in several 50 nm wide spectral bands as a function of the driving gate voltage. A clear trend in the optimal driving frequency can be seen when the data are normalized (figure 4.8). Generally, emission at shorter wavelengths peaks at larger optimal driving frequencies than emission at longer wavelengths. Figure 4.9 shows the measured optimal driving frequency as a function of the emission wavelength for electroluminescence integrated over a $\sim$6 nm passband. These data suggest that charge injection into small nanocrystals occurs faster than charge injection into large nanocrystals. This could be a consequence of the distribution of the nanocrystals within the gate oxide. On average we expect smaller nanocrystals to be closer to the channel than the larger nanocrystals that form predominantly at the center of the ion implantation distribution.

If charging processes did not limit electroluminescence, we would create the same exciton population in the nanocrystal ensemble at any driving frequency. Each pulse would begin at the same initial amplitude and decay according to the familiar stretched exponential curve. The optimal driving frequency (which would then correspond to a corner frequency instead

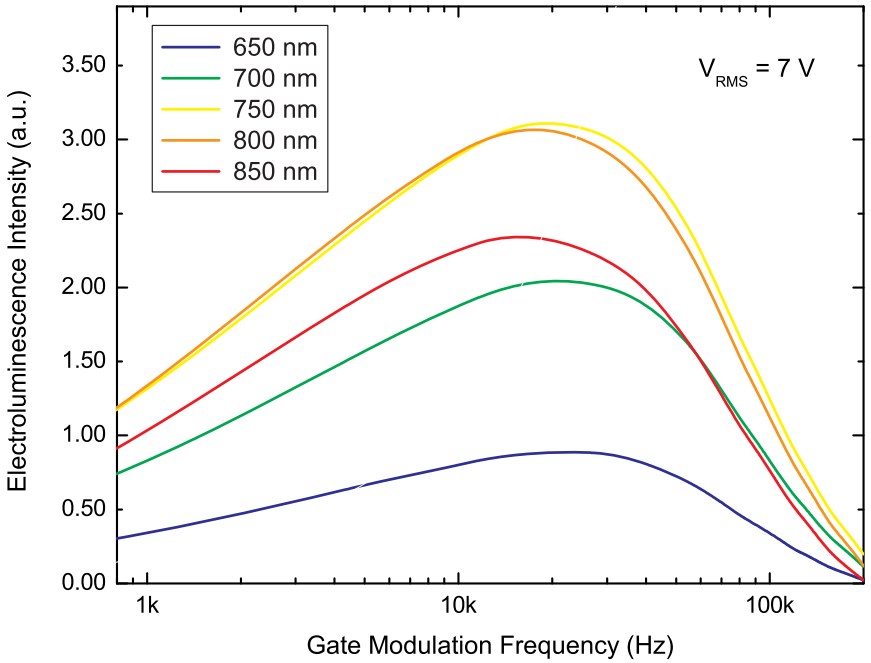

Figure 4.7. The electroluminescence intensity at different emission wavelengths shows broadly similar trends as the gate voltage driving frequency changes. Longer wavelength emission from larger silicon nanocrystals peaks at reduced driving frequencies.

of an emission peak) would vary inversely with the decay lifetime, because emission would be limited by the fraction of the excitons that decay before the gate bias is switched. We have drawn this limit in figure 4.9 for nanocrystals emitting with 100% quantum efficiency and for 30% quantum efficiency, which we estimate as an upper bound for the nanocrystals in our device based on the electroluminescence decay lifetime. Note that the total electroluminescence intensity is reduced in FELED with low quantum efficiency nanocrystals at every driving frequency, despite the optimal driving frequency being higher as a consequence of the reduced decay lifetime.

4.5 Optical Measurement of Charging Processes

Because the magnitude of the electroluminescence signal is related to the charge stored in the nanocrystal ensemble, we can optically monitor charging and discharging processes. For example, the electroluminescence pulse at the transition between $V_g = -6$ V and $V_g = +6$ V becomes smaller as the dwell time at -6 V is reduced (figure 4.10).

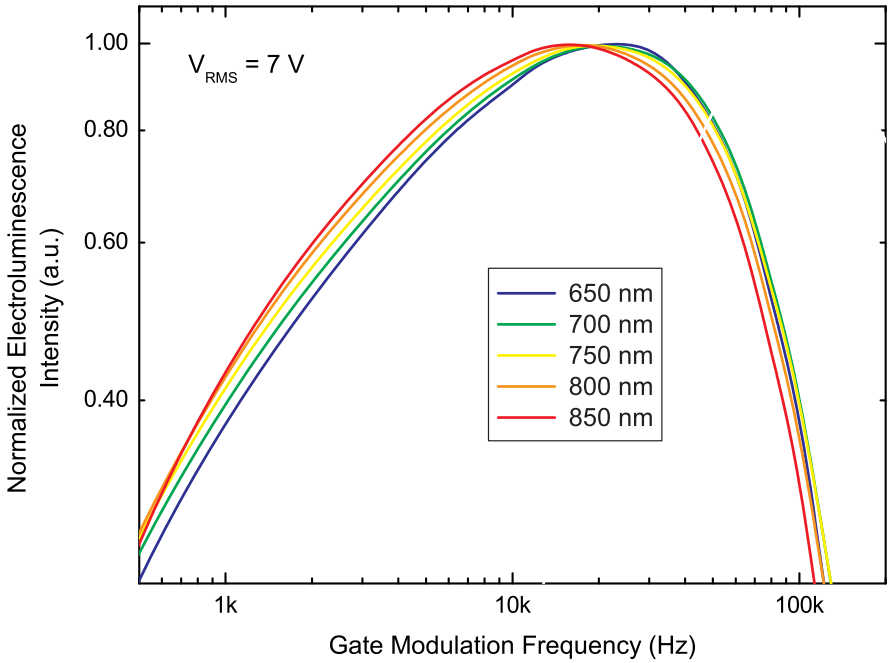

Figure 4.8. The normalized electroluminescence intensity at different emission wavelengths shows the trend in optimal driving frequency more clearly.

Likewise, we can study retention processes by dwelling at an intermediate gate bias before transitioning to the final gate bias level (figure 4.11). In this case, we also observe that some fraction of the electron-charged nanocrystals undergo field effect electroluminescence at the intermediate bias level, while other nanocrystals remain charged with electrons until the gate bias is switched to the final voltage level. This may be attributed to the distribution of the nanocrystals in the gate oxide. The nanocrystals that are closer to the channel will be more sensitive to small changes in the gate bias.

Following this approach, we studied charge injection from the substrate into the nanocrystal layer and charge retention after programming by observing the electroluminescence response when the gate voltage was periodically cycled with a carefully designed waveform. Figure 4.12(a) shows a representative plot of the waveforms used to electrically pump our FELED in order to obtain hole injection and electron retention times. Similar waveforms with inverted polarity were used to measure the electron injection and hole retention times (figure 4.12(b)). The different voltage steps of the waveform are labeled for reference. The injection and retention experiments are separated by the shadowed region III in figure 4.12(a). A reset pulse is applied in region VII to initialize the charge state to the same

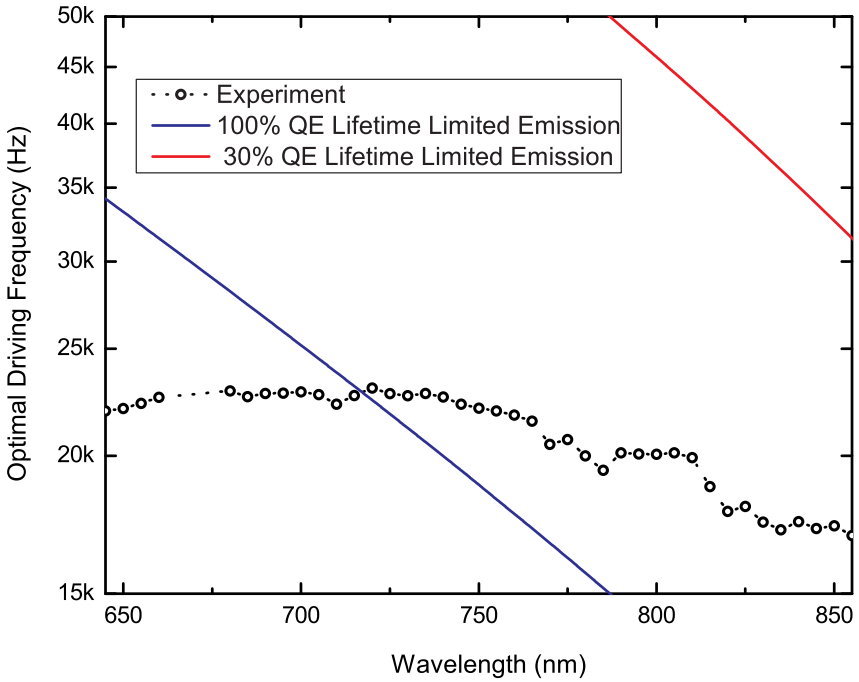

Figure 4.9. The optimal driving frequency for electroluminescence is found to vary with the emission wavelength in our devices. The drawn lines represent the trends that we would expect in a device that was limited by the statistics of spontaneous emission (at 30% and 100% radiative quantum efficiency) rather than by charge injection processes.

value at the end of each cycle. The varying parameters are the programming times for electrons and holes (t_{pe} and t_{ph}, region I), the dwell times for electrons and holes (t_{de} and t_{dh}, region V), and the disturbance voltage at which the retention is measured (V_d, region V). The values chosen for these parameters are summarized in table 4.1.

Table 4.1. Waveform parameter values measured to optically measure charge injection and retention in a FELED

$t_{p(e/h)}$ (μs)	$t_{d(e/h)}$ (μs)	V_d (V)
10, 20, 50, 100, 200, 500, 1000	10, 50, 100, 500, 1000	−2, 0, 2

When these waveforms are used to cycle the gate voltage for the FELED, a peak in electroluminescence is observed at those points where the voltage is abruptly changed (gray-shaded curve in figure 4.12(b)). A relative change in the electroluminescence intensity reflects a relative change in the integrated current between the channel and the silicon nanocrystals,

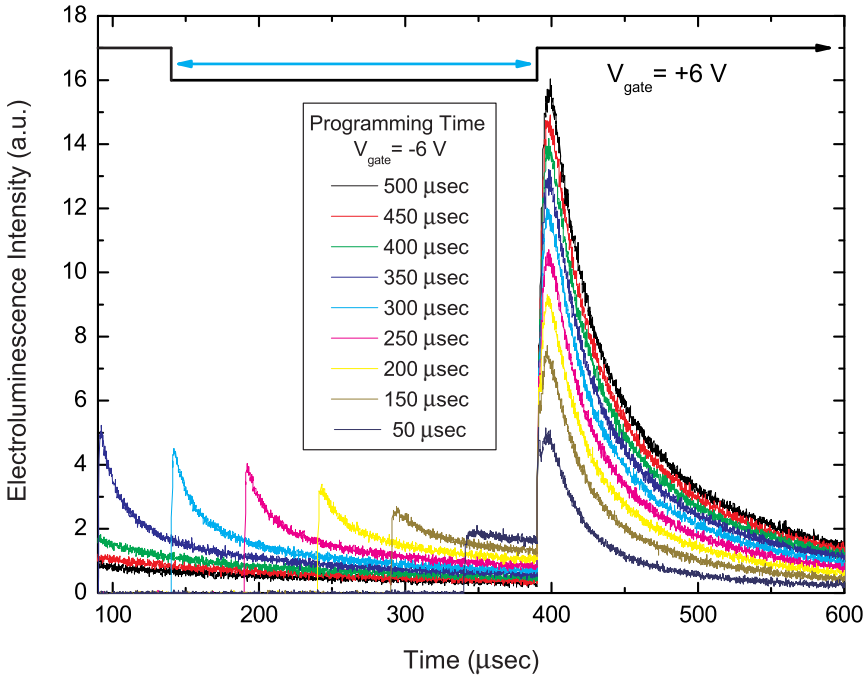

Figure 4.10. Electroluminescence in a FELED decreases if less time is allotted for storing holes in the nanocrystal ensemble. The intensity of the electroluminescence signal can be used an indirect measurement of the stored charge.

enabling us to study the device charging and discharging dynamics by means of optical measurements. Note that the electroluminescence signal arises only from the tunneling current that drives the formation of excitons in silicon nanocrystals. Our measurements are not sensitive to any leakage current flowing through the gate oxide.

Other well-established methods are available for electrically characterizing the charge injection and retention in continuous and discrete trapping memories. However, these techniques measure changes in the conductance of the channel caused by the total charge present in the oxide. In contrast, our optical approach measures the light emitted by the silicon nanocrystals in response to second carrier injection. Therefore, only the charging of optically active silicon nanocrystals is included, leaving aside the electrostatic screening effects of other kinds of oxide charging (e.g., trapping defects or ionic contamination). Such an oxide charging is relevant for evaluating the ultimate performance of memories but may obscure charging phenomena related specifically to the silicon nanocrystals.

Charge injection characteristics for both electrons and holes were determined from regions I and II. The silicon nanocrystal array was partially charged with electrons (holes)

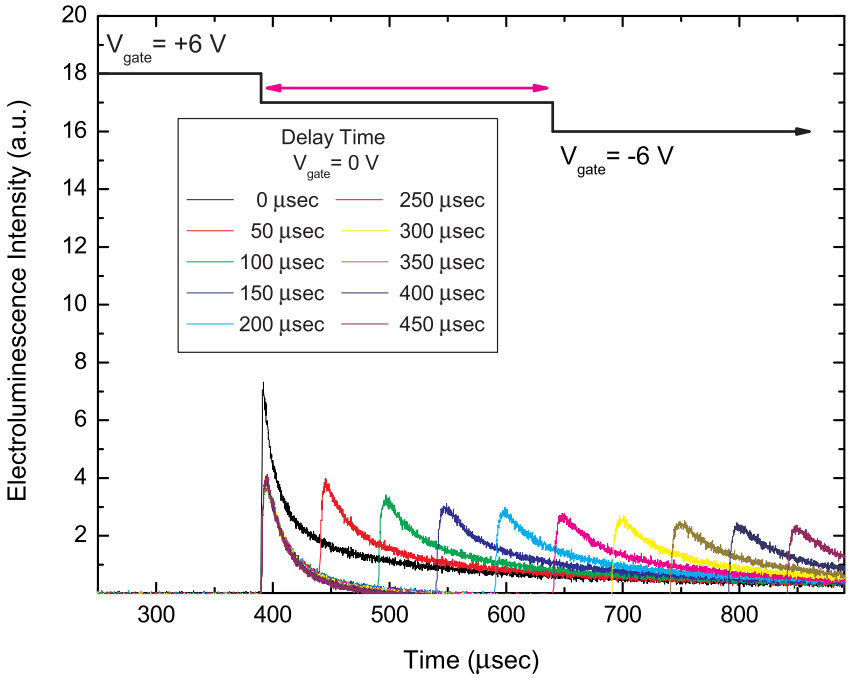

Figure 4.11. The intensity of the electroluminescence pulse decreases when the gate bias is held at 0 V for a dwell period prior to the −6 V readout bias. The decrease is attributed to electrons leaking from the nanocrystal ensemble.

from the inversion (accumulation) layer when a gate voltage of 6 V (−6 V) was applied for t_{pe} (t_{ph}) seconds. The relative amount of charge injected during programming was inferred from the integrated electroluminescence recorded during a subsequent −6 V (6 V), 100 µs readout pulse.

The times for electron and hole injection were found to differ as shown in figure 4.13. It is surprising that the holes appear to be more easily injected than electrons, considering the larger potential barrier SiO_2 presents for the valence band of silicon in comparison to the conduction band. This issue can be resolved by noting the influence of the complementary charge readout pulse. A limitation of our method is the destructive character of the optical charge measurement, due to the fact that the readout process requires the injection of oppositely signed carriers under a reversed gate bias. Since the readout pulse cannot be instantaneous, the charge present in the silicon nanocrystal array may tunnel back to the substrate before forming excitons. This results in an underestimate of the actual charge stored in the nanocrystal ensemble. An ideal measurement is reached only if the measured carriers have an infinite retention or if the readout carriers have an instantaneous injection

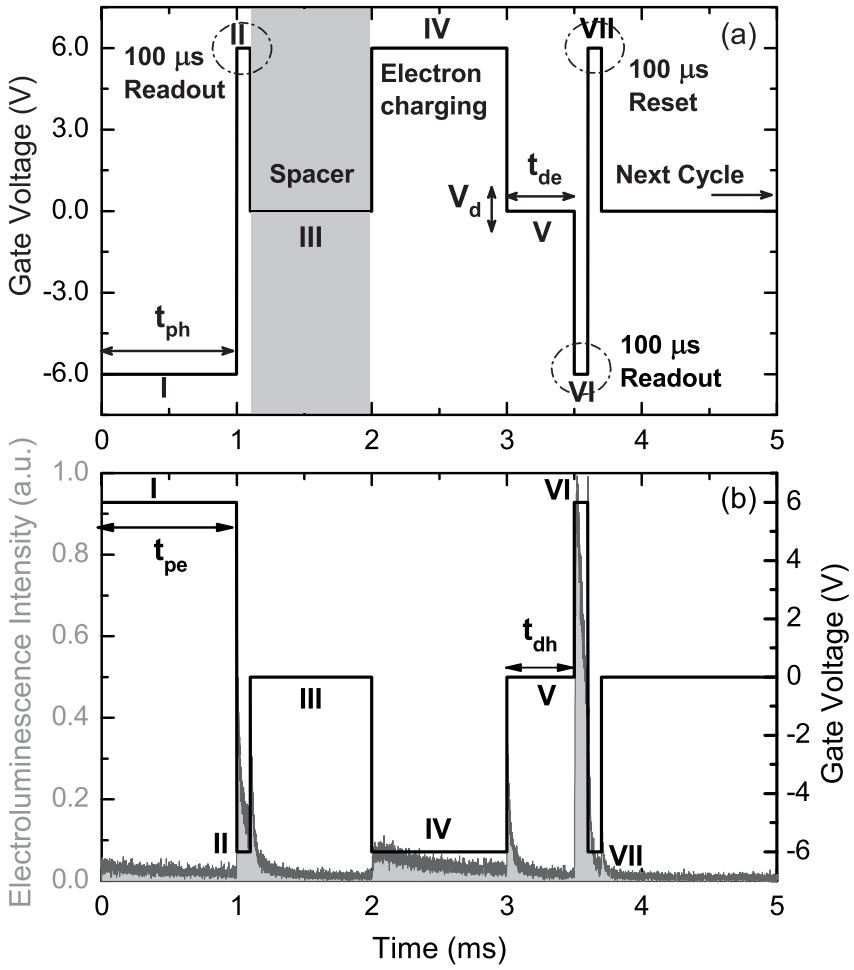

Figure 4.12. This schematic shows the waveforms used to measure the charging processes in the FELED device. The electroluminescence response (gray shading) that is obtained by driving the device with such a waveform is shown in (b).

time.

In our device, the measurement of electron storage is more susceptible to this limitation as a consequence of both the slower injection of holes during the readout pulse and the faster discharging rate for electrons. In contrast, our measurement of hole storage should be more reliable as the number of holes tunneling back to the substrate is small. As reported in the literature [169], this carrier asymmetry could potentially be overcome by scaling down the oxide thickness. It appears that the total hole charge stored in the nanocrystal ensemble does not saturate, even after the programming gate bias has been maintained for 1 millisecond. Based on the optical memory measurements reported in section 3.7, we

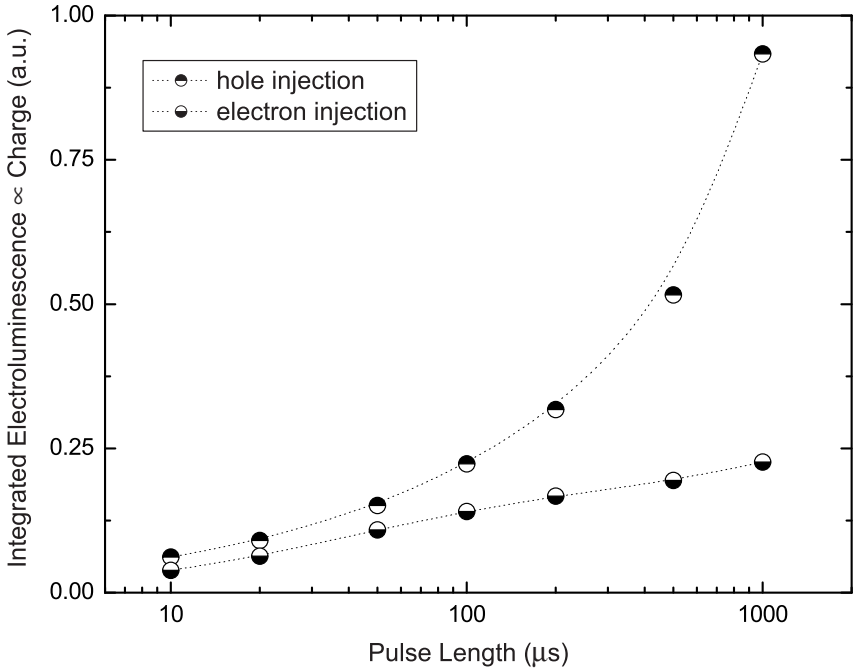

Figure 4.13. Charge injection characteristics for electrons and holes inferred from the electroluminescence signal integrated over the readout pulse (region II in figure 4.12).

would expect that charge injection processes at ±6 V would eventually saturate on second time scales. However, most of the stored charge is injected within the first ∼100 μs.

In order to quantify the retention times, we examine data from regions IV, V, and VI. First, a gate voltage of 6 V (−6 V) was applied for 1 ms, fully charging the silicon nanocrystal array with electrons (holes). Afterwards, a disturbance voltage V_d was applied for t_{de} (t_{dh}) seconds. Finally, the remaining charge in the array was measured by integrating the electroluminescence intensity trace over a 6 V (−6 V), 100 μs readout pulse. The disturbance voltage has an important impact on retention, as can be seen in figure 4.14. The electron (hole) release from the nanocrystal floating gate array to the channel is facilitated by the negative (positive) disturbance voltage due to the gate bias enhancement of the leakage process. For $V_d = -2$ V (2 V), the electron (hole) number is decreased by 62% (38%) compared to 39% (23%) of the charge loss during the first 1 ms at $V_d = 0$ V. The retention is greatly increased for electrons (holes) when a positive (negative) disturbance voltage is applied across the structure. Under this gate bias condition, the external field inhibits the leakage of electrons (holes), and only 25% (10%) of the initial charge is lost within the first 1 ms.

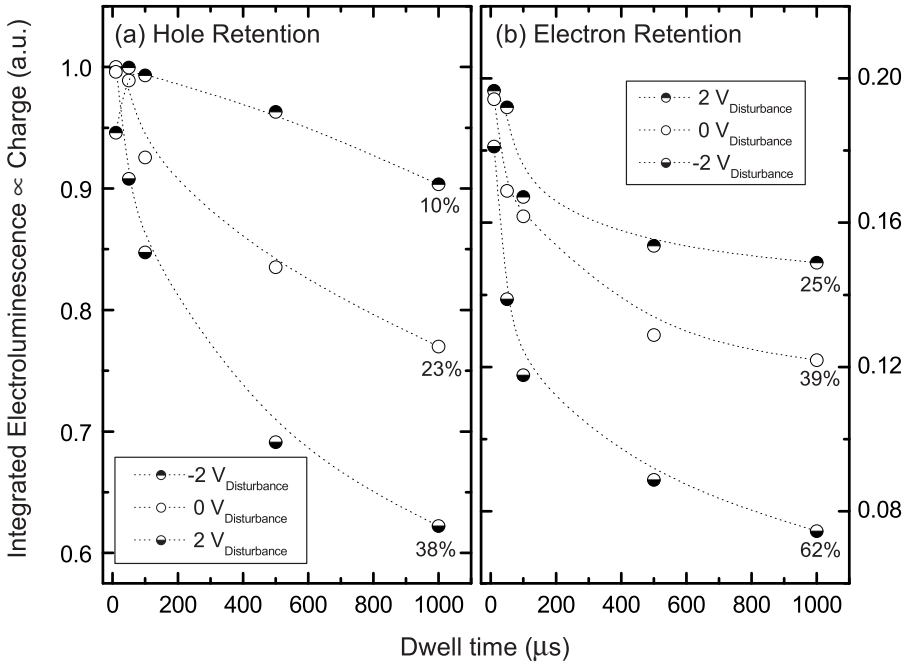

Figure 4.14. The retention characteristics for (a) holes and (b) electrons at different disturbance voltages as extracted from the integrated electroluminescence signal from region VI (see figure 4.12).

The dynamics of the charge retention typically show a substantial negative slope at short dwell times and a more stable charge level for longer time scales. This may be a consequence of the distribution of nanocrystals within the gate stack, since the tunneling rate for the stored charge will decrease exponentially with distance from the silicon nanocrystals to the interface. The effective potential of the nanocrystal array also changes as charge is removed, which would be expected to improve the stability of a partially charged array. It is also possible that some fraction of the excitons created in the transition to the dwell voltage (as in figure 4.11) are recombining during the readout pulse for very short dwell times and inflating the initial values. It is worth noting that the previous discussion of our tendency to underestimate the storage of electrons also holds here, and that the actual loss rates obtained for electrons are therefore expected to be smaller than those reflected in figure 4.14(b).

4.6 Band Edge Emission

At higher driving frequencies, we observe additional electroluminescence at longer infrared wavelengths that we associate with exciton recombination in the channel of the device. Figure 4.15 shows the electroluminescence spectrum observed when the gate bias is switched between 7 V and −7 V at a frequency of 80 kHz. In addition to silicon nanocrystal electroluminescence centered at 780 nm, we see a broad emission component centered at ∼1140 nm, which is consistent with band-to-band radiative recombination in bulk silicon.

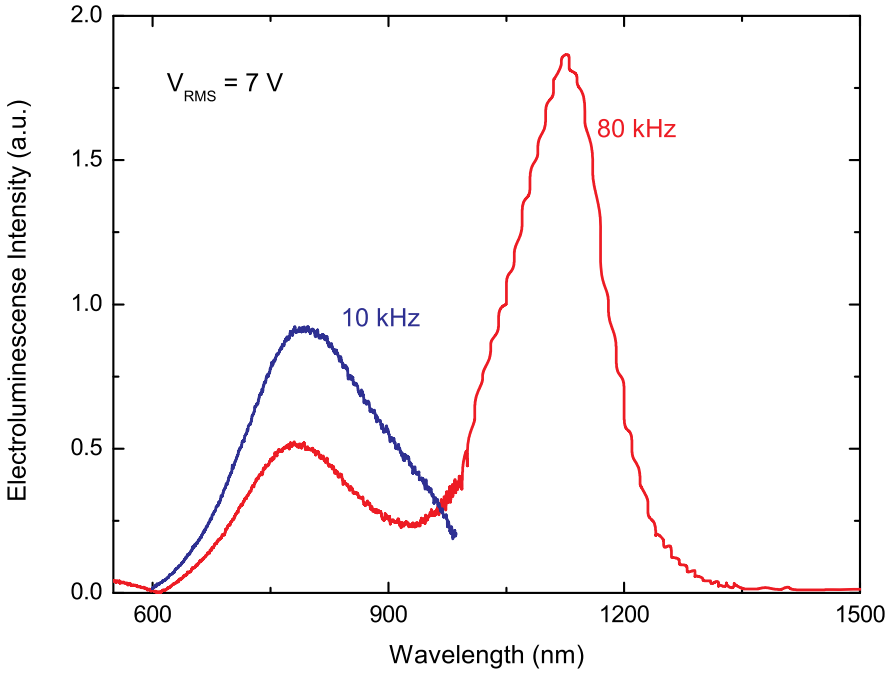

Figure 4.15. We observe electroluminescence associated with recombination in the channel of our device at higher gate bias driving frequencies. The intensity of this signal can be greater than the emission detected from the silicon nanocrystal ensemble.

The frequency dependence of the band edge electroluminescence component is shown in figure 4.16. The signal initially increases linearly with increasing gate modulation frequency until a peak is observed at ∼80 kHz. At higher driving frequencies, the band edge electroluminescence decreases.

The band edge electroluminescence intensity appears to closely track the signal we have associated with field-effect electroluminescence in the silicon nanocrystal ensemble. The initially linear dependence on driving gate frequency strongly suggests that the band edge

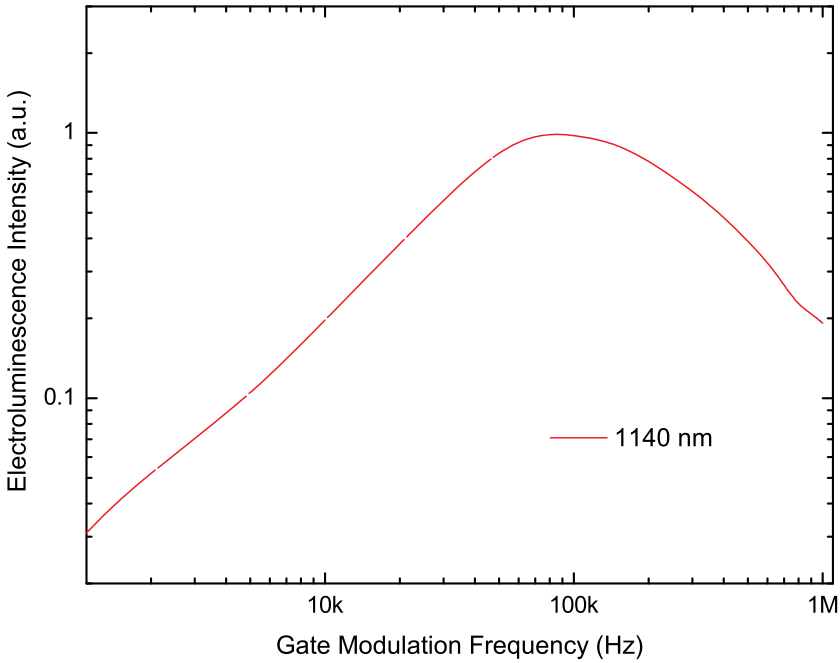

Figure 4.16. The frequency response of Si band edge emission in a FELED.

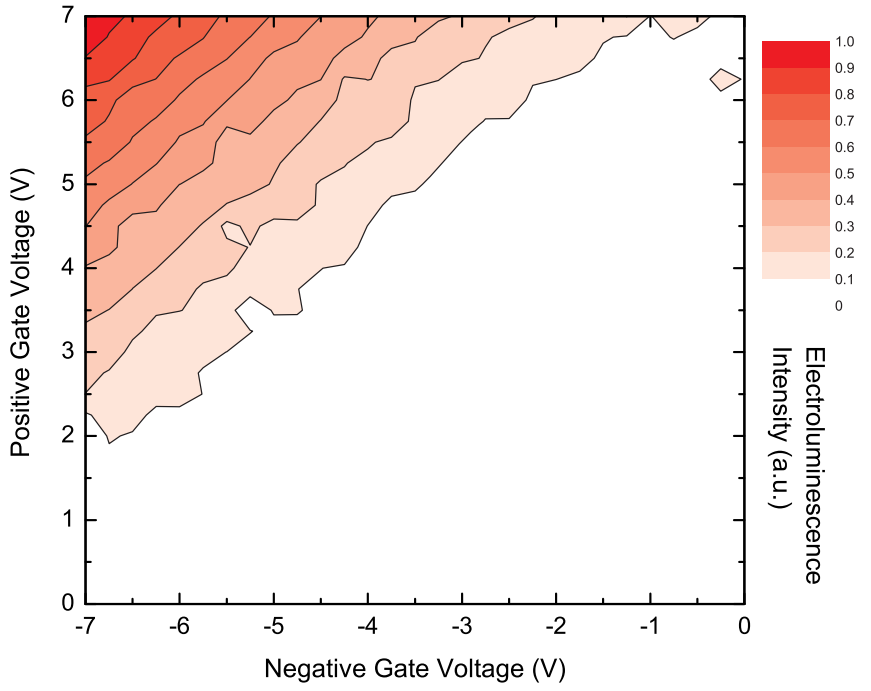

Figure 4.17. The intensity of the Si band edge emission is greatest for large, symmetric transitions in gate bias at a driving gate frequency of 140 kHz.

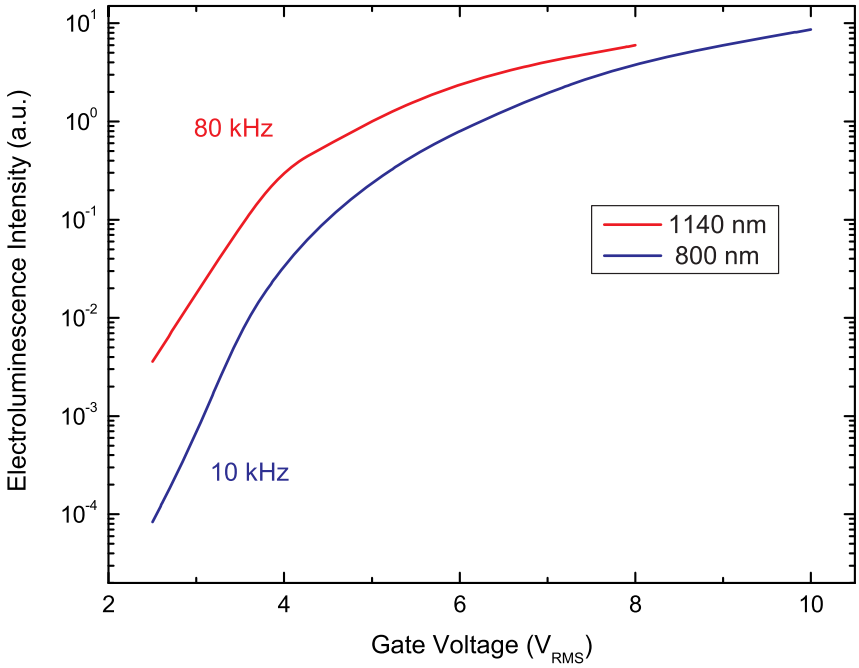

Figure 4.18. The electroluminescence response at the silicon band edge mirrors the driving gate voltage dependency of the silicon nanocrystal emission.

electroluminescence is emitted in pulses at transitions in gate bias. Figure 4.17 shows that the band edge electroluminescence is most intense for large changes in gate bias (compare to figure 4.4). The dependence of the band edge electroluminescence on the driving gate bias is also similar to our observations of silicon nanocrystal field-effect electroluminescence. As shown in figure 4.18, the intensity at 1140 nm rapidly increases over several orders of magnitude as the RMS gate bias is ramped from 2.5 V to 8 V (contrast to figure 4.6).

Taken together, these observations suggest that the band edge electroluminescence we observe is related to charge stored in the silicon nanocrystal ensemble. We speculate that the source of the emission is band-to-band recombination in the channel at positive-to-negative transitions in gate bias. As the depletion zone collapses, electrons from the inversion layer and some fraction of those electrons that are stored in the silicon nanocrystal ensemble will encounter holes that are gathering to form the accumulation layer. This should result in pulses of electroluminescence at positive-to-negative gate bias transitions and a peak frequency response that matches the time scale for electron injection into the nanocrystal ensemble.

4.7 Photoluminescence Recovery

We can also monitor the photoluminescence of the silicon nanocrystal ensemble through the semitransparent gate contact of the FELED while applying the large amplitude gate bias modulation used to drive field effect electroluminescence. As demonstrated in chapter 3, the photoluminescence signal will decrease if the nanocrystal ensemble is charged because Auger recombination will quench the radiative recombination of excitons.

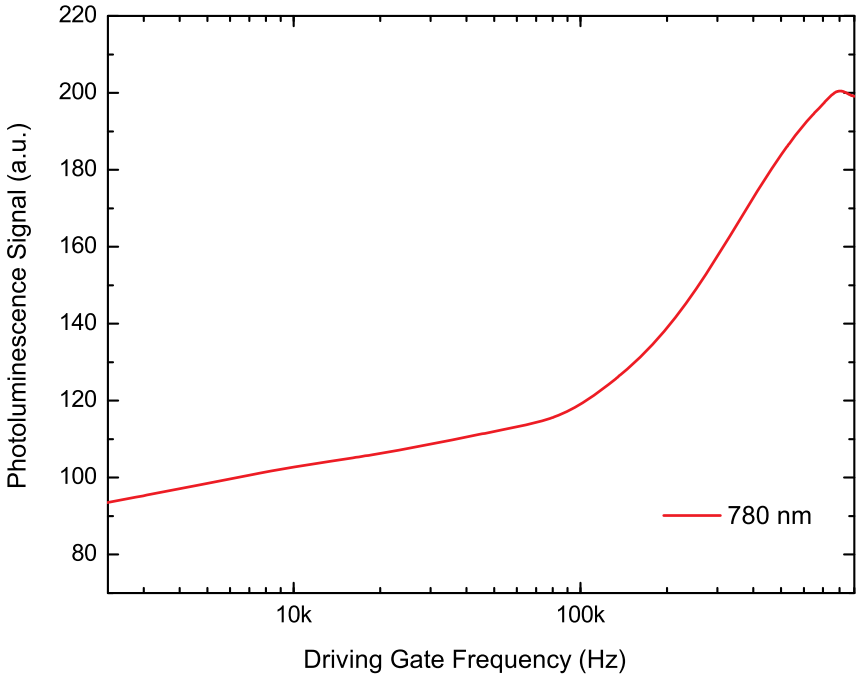

Figure 4.19. The photoluminescence signal of the nanocrystal ensemble is quenched by an applied gate modulation (±7 V), but recovers at driving frequencies above ∼100 kHz. This observation suggests a time scale for electron injection and may be correlated to the frequency dependence of band edge electroluminescence (figure 4.16).

Figure 4.19 shows the photoluminescence signal recorded from the nanocrystal ensemble embedded in a FELED as the driving frequency is increased from 20 kHz to 1 Mhz. We do not observe silicon nanocrystal electroluminescence over this frequency range, because the gate bias is changed too quickly for hole injection to charge neutral nanocrystals with holes. However, we expect that electron injection can still proceed and anticipate that the nanocrystals are charged with electrons for some portion of each bias cycle. Photoluminescence should be reduced in proportion to the average number of electrons stored in the nano-

crystal ensemble. The photoluminescence signal is observed to recover when the driving frequency is increased beyond ∼100 kHz. This suggests that electrons are injected into the nanocrystal ensemble on a characteristic 10 μs time scale. This result is consistent with our explanation of the optimal driving frequency found for band edge emission.

4.8 Simulation

Our model for the field-effect electroluminescence mechanism relies on a sequential carrier injection process that is counterintuitive. It is surprising that second carriers can be injected into the nanocrystal ensemble before the previously stored first carriers return to the channel. It is also unconventional to describe electrical observations in terms of hole transport or hole storage for a floating gate transistor. Typically hole transport is not observed in floating gate memory devices because the valence band potential barrier between silicon and silicon dioxide is so much larger than the conduction band barrier. However, a typical modern FLASH memory cell has a tunnel oxide that is 6–8 nm thick in comparison to the ∼4 nm tunnel barrier targeted in our fabrication process. Tunneling depends exponentially on the barrier thickness, so hole tunneling process are much more likely in our device. However, we still expect that hole transport should be slow in comparison to electron transport.

Our experiments suggest that hole injection into neutral nanocrystals occurs on 100 μs time scales while electron injection requires 10 μs. We have developed a coupled state equation model based on these phenomenological charging time constants that qualitatively reproduces the field-effect electroluminescence phenomenon. We consider the population of nine different nanocrystals states in our model, shown schematically in figure 4.20. Each nanocrystal type is labeled by the number of holes and electrons that it stores. We monitor the nanocrystal population that contains excitons as a measure of electroluminescence while modulating a matrix that represents charge transport for each gate bias level. We assume that charge injection or leakage is enhanced or suppressed by an order of magnitude by Coulomb attraction or repulsion. Further details are provided in appendix B.

Figure 4.21 shows the nanocrystal population state vector solution to the master equation for an initial condition where every nanocrystal is charged with a single hole, when the gate bias is cycled twice between +6 V and −6 V at a rate of 10 kHz. The exciton

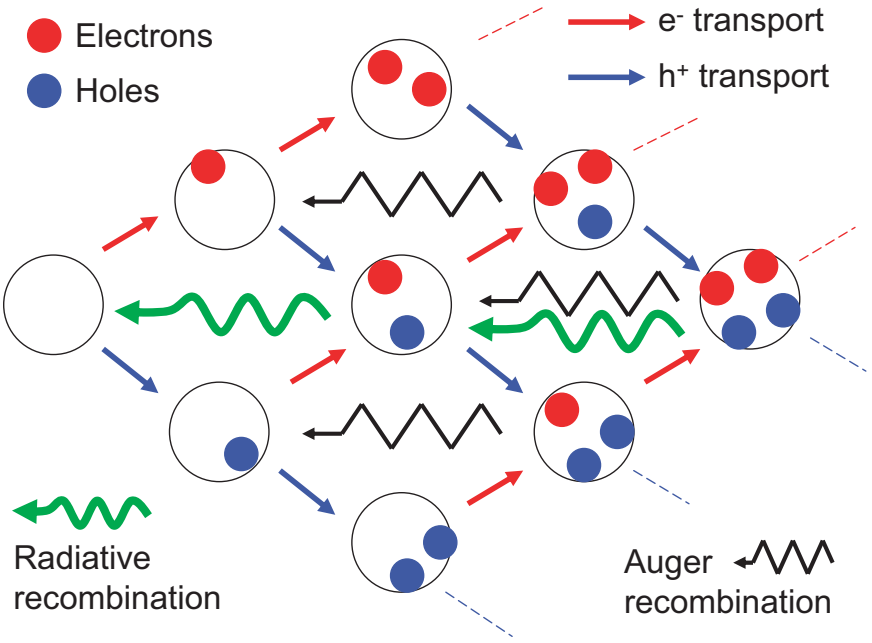

Figure 4.20. This schematic diagram shows the nine nanocrystal populations and the transition processes that connect them in our master equation model for field-effect electroluminescence.

population rises at each transition in gate bias, corresponding to the pulses of emission we observe in field-effect electroluminescence. The model also reproduces the asymmetry in intensity between the pulse emitted at negative-to-positive gate bias transitions and the pulse emitted at positive-to-negative transitions. However, the trends in the time constants for the pulses of electroluminescence do not match our experimental observations. In our model, the weaker pulse of electroluminescence is always associated with slower rise and decay constants.

In principle we could directly perform a least squares fit to our experimental data and find the transition matrices for each gate bias. However, our model has 25 free parameters that we could adjust. It is unlikely that we would converge to a physically meaningful solution by proceeding blindly, especially given that the model does not consider any inter-nanocrystal energy or charge transfer processes or attempt to account for the distribution of tunnel oxide thicknesses in the real device. For this reason we have attempted to determine the injection currents from first principles.

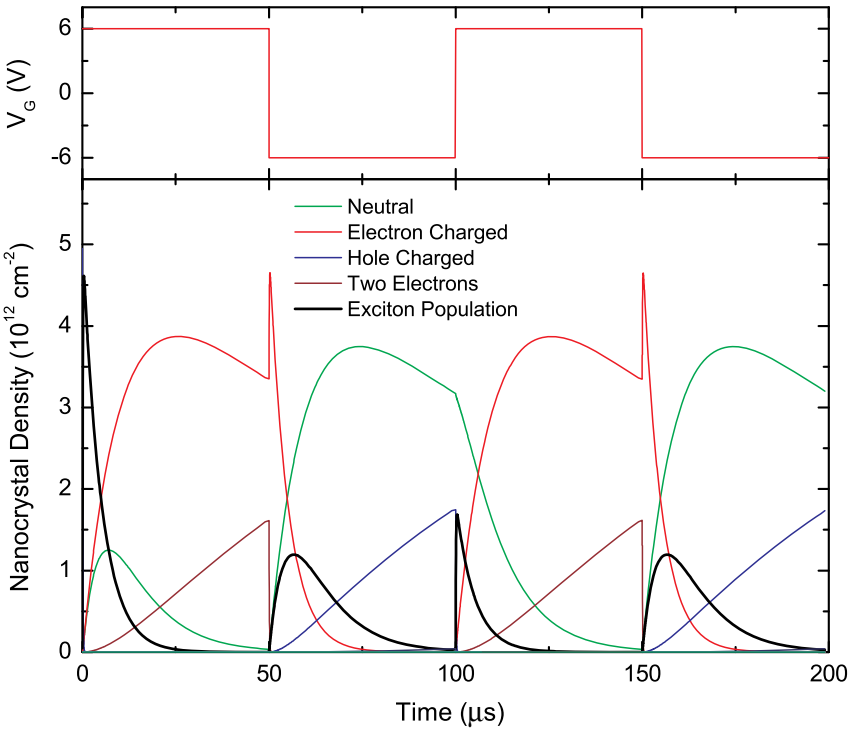

Figure 4.21. The solution to the master equation model for phenomenological injection current values qualitatively reproduces the electroluminescence we observe in a FELED.

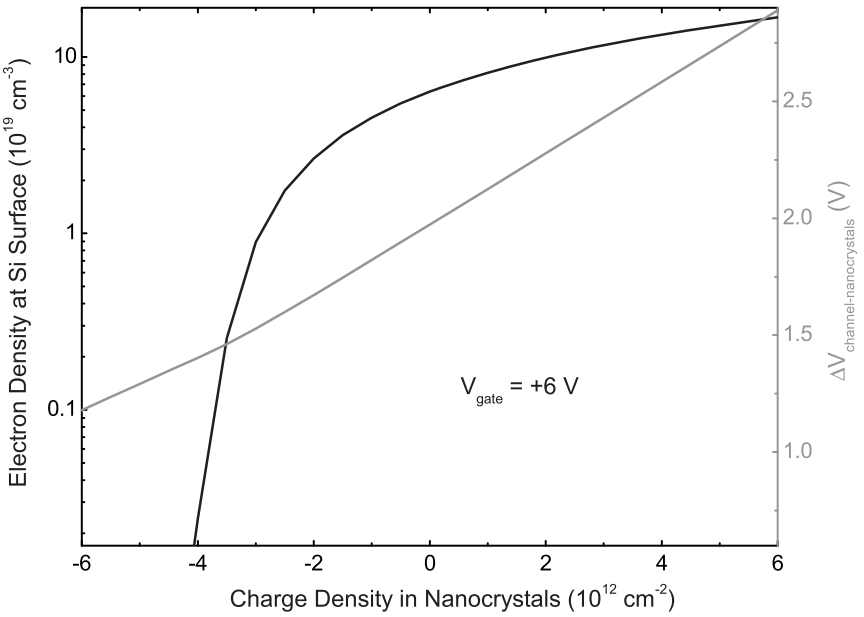

Figure 4.22. Semiclassical self-consistent electrostatic simulation of a FELED in equilibrium at a gate bias of +6 V.

4.9 First Principles Calculation of Tunnel Currents

A semiclassical self-consistent calculation was applied to provide a more quantitative explanation for the observed Coulomb field enhanced and inhibited charge injection processes. This approach does not properly account for the quantization of channel electrons in the inversion layer, but can still provide an estimate of the tunneling barriers for charge injection into the nanocrystals.

The gate stack of the device was modeled as a 15 nm thick oxide layer. Different levels of stored charge in the nanocrystal layer were modeled as a uniformly distributed charge density in a plane 5 nm from the channel. The p-type channel doping level was 3×10^{18} cm^{-3} and the n-type doping level for the polysilicon gate was 10^{20} cm^{-3}. Figures 4.22 and 4.23 show the stored charge dependence of the channel carrier density at the silicon interface and the potential difference between the channel and the nanocrystal layer, at gate biases of +6 V and −6 V, respectively. The barrier potential for tunneling between the channel and the nanocrystals is raised or lowered by the presence of previously injected charge carriers. From these data, it is possible to calculate the tunneling current between the channel and the floating gate of the silicon nanocrystals (figure 4.24) using the method of Simmons [170].

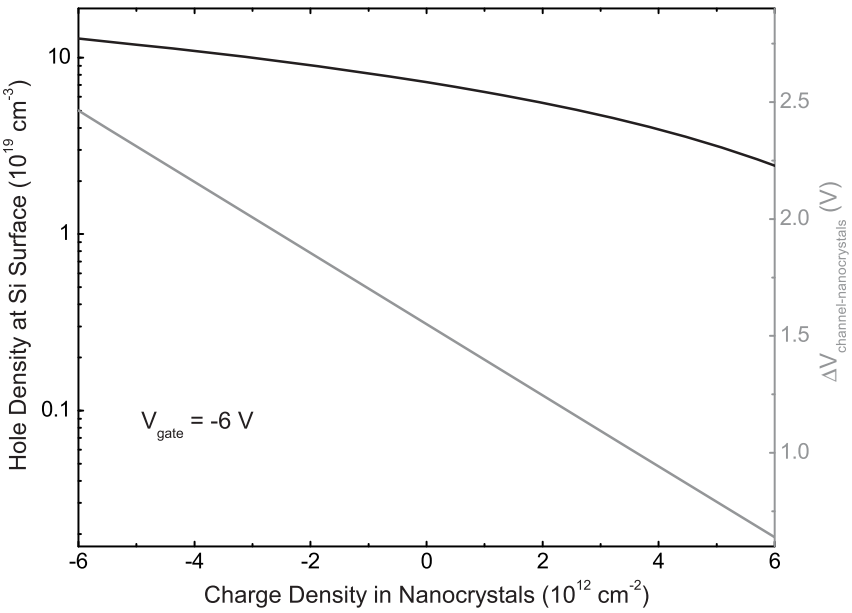

Figure 4.23. Semiclassical self-consistent electrostatic simulation of the FELED in equilibrium at a gate bias of −6 V.

A comparison of the rise times for electroluminescence in figure 4.3 (∼0.25 μs and ∼2.5 μs) to the injection time for the first charges (∼10–100 μs) suggests that tunneling is dramatically enhanced by the presence of the complementary charge in the nanocrystal array. This trend is reproduced by our model for the tunneling currents, which shows that the electron and hole currents vary strongly as a function of the total charge stored in the nanocrystal layer. For example, the electron injection is enhanced by a factor of ∼10 by the presence of holes with an areal density of 2.4×10^{12} cm^{-2} in the nanocrystal ensemble. Hole tunneling is enhanced by a factor of ∼10 by the presence of electrons with an areal density of 1.6×10^{12} cm^{-2} in the nanocrystals (figure 4.24). On the other hand, like charges injected into the nanocrystal array partially shield the electric field due to the gate bias, resulting in a dramatic decrease of channel carrier densities as well as tunneling currents. The phenomenon of Coulomb field inhibited tunneling is especially evident for the injection of electrons. At an applied +6 V gate potential, the strong inversion layer in the channel disappears when the areal density of electrons in nanocrystals exceeds $\sim 3.5 \times 10^{12}$ cm^{-2}. In this case, the electron tunneling current is greatly reduced.

The calculated tunneling current densities in figure 4.24 are far too small to correspond to our observations. The tunneling rates increase if the assumed tunnel oxide thickness is

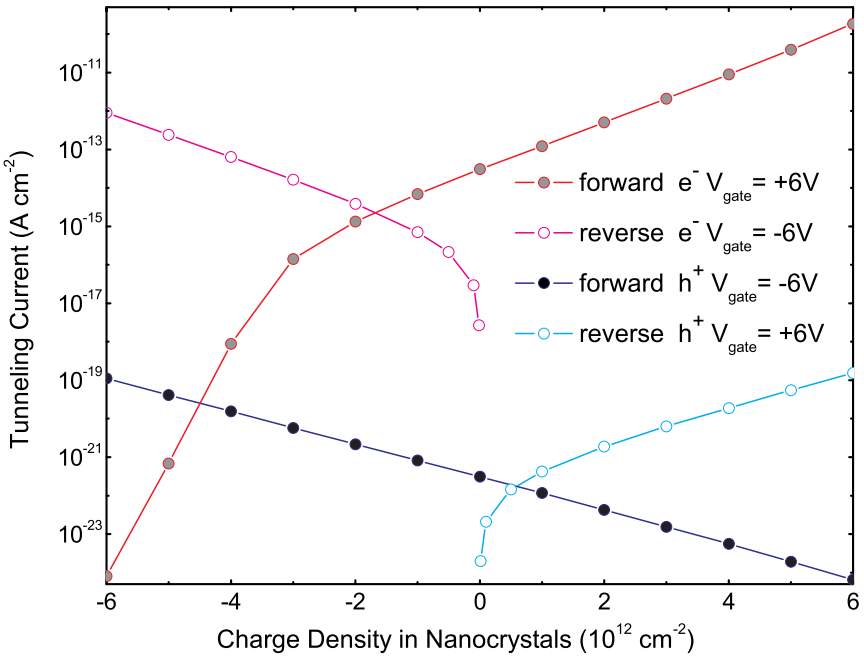

Figure 4.24. Calculated tunneling currents from the channel into the nanocrystal layer demonstrate the Coulomb field enhancement and inhibition of the charge injection. The calculated current magnitudes are far too small to explain field-effect electroluminescence.

reduced. Additionally, the effective mass of holes in SiO_2 is not well known and might be adjusted in the tunneling calculation to improve the match to the experimental charging time constants.

We also calculated the injection currents using the semianalytical direct tunneling model of Cordan [171]. These simulations solve Schrödinger's equation in the channel and in a representative single nanocrystal and look for aligned energy levels that could support direct tunneling. In simulations of structures with 2 nm and 3 nm tunnel oxide thicknesses, the typical tunneling times for charge injection into either neutral or singly charged nanocrystals are orders of magnitude too slow to correspond to our experiment.

Taken together, these simulations suggest that injection may not be dominated by tunneling processes. In view of the damage that ion implantation may cause to the tunnel oxide, it is possible that charge injection could also occur via the Poole-Frenkel mechanism or some other defect mediated process [172]. The particular mechanism for carrier injection in the FELED does not substantially change the sequential carrier injection model.

4.10 Comments on an Impact Ionization Model

We believe the proposed sequential carrier injection mechanism for field-effect electroluminescence is consistent with all of our observations. However, we recognize that the invocation of hole transport processes through the tunnel oxide invites some measure of skepticism. An alternative explanation can be formulated that relies only on electron transport across both the tunnel oxide and the control oxide of the device.

In this alternative model, the silicon nanocrystal ensemble is assumed to be located in roughly the center of the gate oxide, so that charge transport can occur across both the tunnel and control oxide layers. We believe based on our fabrication process that the control oxide is actually thicker than the tunnel oxide. When the gate bias is switched to +6 V, hot electrons are injected into the silicon nanocrystal ensemble from the polysilicon gate contact, causing exciton formation through impact ionization. The gate oxide acquires a net negative charge over a 10–100 μs time scale due to nanocrystal or oxide defect charging. This stored charge eventually inhibits the further injection of electrons from the gate and the device stops emitting light. When the gate bias is switched to −6 V, the previously stored charge is flushed to the gate contact and electrons are injected into the nanocrystal ensemble from the inverted channel. A pulse of electroluminescence is observed while impact ionization occurs. Eventually, negative charge builds up in the gate oxide or on the nanocrystals that are closer to the channel than to the gate and the injection of electrons stops.

We are able to explain the pulsed emission characteristics of our FELED using this model. The asymmetry of the pulses could be attributed to a difference in the thickness of the tunnel and control oxide barriers. The stored electrons that cause the pulsed output might require a large reversed gate bias to flush from the oxide, possibly explaining the small electroluminescence intensity for cycling the gate bias between 0 V and ±6 V in contrast to symmetrical gate bias modulation between −6 V and +6 V (see figure 4.4).

We do not prefer this description for our devices because it does not seem to satisfactorily explain our observation of electroluminescence for gate bias modulation at 2.5 V_{RMS}. We believe impact ionization is unlikely to occur under such low voltage conditions. However, there are reports in the literature that posit impact ionization by electrons that have sub-bandgap energy in silicon [173, 174]. It is also known that charge transport in very thin SiO_2 films can be nearly adiabatic [74]. The process might even be enhanced in silicon

nanocrystals due to carrier confinement, given the reciprocal relationship between impact ionization and Auger recombination. In any case, it appears that this alternative explanation can not be dismissed based on the evidence of our experiments and that further work will be required to resolve the issue.

4.11 Performance Limits

It is useful to estimate the maximum power output that might be achieved from a FELED. For an ideal device containing a close packed array of small nanocrystals, an areal nanocrystal density of $\sim 10^{12}$–10^{13} cm^{-2} could possibly be achieved while maintaining a uniform tunnel oxide thickness. Assuming 100% internal quantum efficiency for the nanocrystals, this device could emit as many as two photons per nanocrystal per complete gate voltage cycle. Multilayer designs might conceivably increase this output capacity but will be excluded from consideration here. For conversion to the units of power, we will further assume that the photons are emitted at 1 eV regardless of the nanocrystal recombination rate. This is an acceptable approximation for the material systems that one might consider in practice.

There may be some room for improvement in the gate contact layer used in our current device. The thin polysilicon design strikes a balance between conductivity and absorption, but no specific efforts have been made to improve the out-coupling of light from the nanocrystals. For the purpose of establishing an upper bound, we will assume that the ideal device emits light with an external quantum efficiency of 50%.

The average power output of a FELED will scale linearly with the driving gate frequency until one of a number of possible limiting factors becomes significant. The maximum useful driving frequency is limited by the statistics of spontaneous emission. If the driving gate frequency is increased beyond about half the radiative recombination rate, the output of the device will rapidly saturate while the efficiency quickly decreases. The integrated probability of emitting a photon decreases linearly at such high frequencies, counteracting the linear improvement gained from cycling the FELED at faster rates. Thus, the optimal driving frequency for a FELED will be determined by the radiative rate of the emitting nanocrystals. We can conclude that an optimized silicon nanocrystal FELED will likely saturate at a driving frequency below 100 kHz. It may be possible to enhance the spontaneous emission rate by engineering the local dielectric environment of the nanocrystals or to extract the energy of

the excitons by some faster nonradiative mechanism [70].

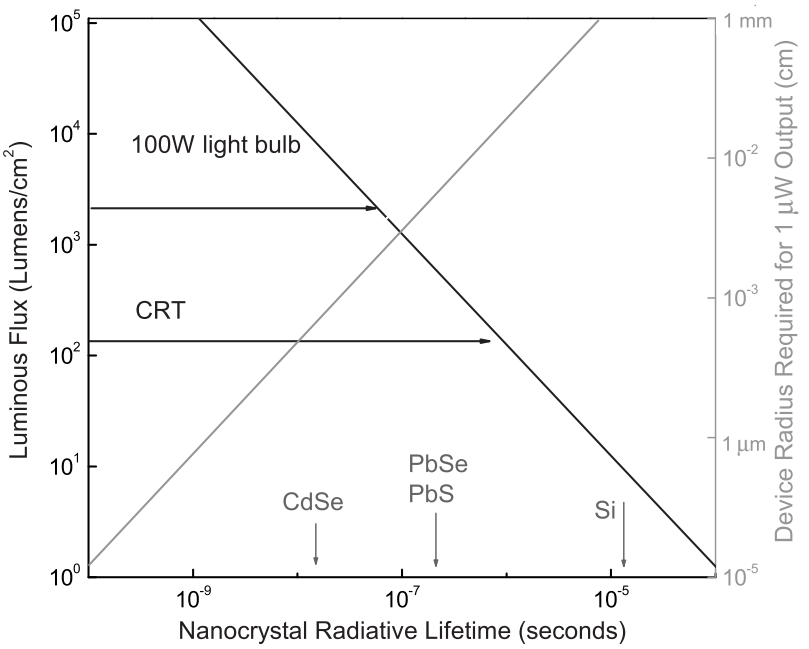

Figure 4.25. Approximate ideal case limits for the maximum power output of a FELED parameterized by the nanocrystal radiative emission rate, which effectively determines the maximum cycling rate for each device.

Within this framework, we can calculate approximate ideal case performance limits for FELEDs constructed from hypothetical nanocrystals with various recombination lifetimes (figure 4.25). Hypothetical performance limits are shown for several commonly studied nanocrystals despite the materials challenges that might arise in the realization of FELEDs that contain them. In consideration of the possible display applications, we have attempted to quantify the luminous intensity of the ideal FELED. The emission wavelength is essential for the conversion of the radiated power to the perceived brightness. Accepted peak values for the conversion factor are 683 lm/W at 555 nm for daylight vision and 1700 lm/W at 507 nm for night vision. We have assumed a value of 300 lm/W in our calculation to reflect an average over the visible range. From this analysis it seems that an optimized silicon nanocrystal FELED could someday be useful in some display applications.

We can further speculate on the maximum power efficiency attainable in an ideal silicon FELED, which would be reached at driving frequencies much lower than the nanocrystal recombination rate, corresponding to a lower output power regime. We have observed

electroluminescence at an energy $\hbar\omega = 1.65$ eV, at driving gate voltages as low as 2.5 V_{RMS}. We will assume that this represents a realistic minimum operating voltage. On a per-nanocrystal basis, each cycle of the gate voltage will require ∼1.2 eV to charge and discharge the gate capacitance. Additional energy will be lost to scattering in the charge injection process, which may be approximated by the voltage drop across the tunnel oxide for the four charge injection events that occur. The potential drop for tunneling into a neutral nanocrystal at a gate bias of 2.5 V is ∼0.8 V, incurred twice per cycle. For electrons tunneling into hole-charged nanocrystals, the drop is ∼1.1 V, while holes tunneling into electron-charged nanocrystals lose ∼0.4 V. Neglecting other sources of loss (e.g., contact resistance), $E_{EL} = 2.2$ eV is required, on average, to program each exciton in an ideal FELED, in contrast to ∼1.1 eV required for exciton formation in an ideal silicon LED. There are two advantages from a power efficiency standpoint for the silicon nanocrystal FELED. The first is that the internal quantum efficiency of a well-passivated silicon nanocrystal can approach 100%, and the second is the greater energy of the emitted photons. If the nonradiative recombination of the excitons is completely suppressed in the nanocrystals, an ideal silicon FELED might reach an internal power efficiency $\eta \equiv \hbar\omega/E_{EL}$ as high as ∼75%.

4.12 Conclusion

Field-effect electroluminescence, as demonstrated in our FELED, is an unanticipated and surprisingly successful approach to the electrical excitation of silicon nanocrystals. Such a device also provides a useful laboratory tool for the study of charge injection processes. In view of our experiments and simulation efforts, it appears that the charge injection process may involve a defect mediated tunneling mechanism. While the efficiency of our FELED is low due to significant gate leakage currents, it should be possible to demonstrate high power efficiency light emission in future optimized silicon nanocrystal devices.

We have additionally considered the power output characteristics of idealized devices to address the feasibility of practical application. In light of our analysis, it appears that an optimized silicon nanocrystal FELED might be a viable candidate for some display applications. While it remains to be experimentally demonstrated that FELEDs can be fabricated in other materials systems, the same performance analysis suggests that a device constructed with direct gap nanocrystals could be very promising.

Chapter 5

Hybrid Infrared FELEDs

5.1 Introduction

In this chapter, we describe preliminary efforts to fabricate hybrid field-effect electroluminescence devices that emit light at infrared telecommunications wavelengths. After briefly discussing photoluminescence in silicon nanocrystal sensitized erbium, we describe the fabrication of an erbium codoped silicon nanocrystal FELED. This device has been proposed as a possible enabling technology for an electrically pumped chip-based erbium laser emitting at 1.5 μm. We then discuss devices designed to allow energy transfer between silicon nanocrystals and solution fabricated PbSe quantum dots.

5.2 Silicon Nanocrystal Sensitized Erbium

The Lanthanide-series "rare earth" elements have a valence configuration that shields the inner $4f$ shell of electrons from the local chemical environment by preferentially shedding one $5d$ and two $6s$ electrons. This gives atoms such as erbium a consistent energy level structure that does not depend significantly on the host medium. The energy levels can be labeled and ordered by applying Hund's Rules within the Russell-Saunders approximation to the charges that remain in the $4f$ shell. Using this approach, we can deduce that the ground state of Er^{3+} is ${}^4I_{15/2}$, and that the relaxation of the first excited state (${}^4I_{13/2}$) is parity forbidden. Erbium ions can only absorb light into or emit light from the first excited state when embedded in a material, like SiO_2 that can impose an asymmetric crystal field to relax the parity constraint. The weak odd parity of the ${}^4I_{13/2}$ state in an erbium ion embedded in SiO_2 gives an excited erbium ion a very long lifetime (∼10 ms). The crystal field also causes Stark splitting of the ionic energy levels, turning each atomic transition into a narrow band of states centered at the atomic energy level.

By a fortuitous coincidence of nature, the energies of the first level excited ion states in erbium ($\sim$0.8 eV) correspond to wavelengths of light ($\sim$1.5 μm) that can travel for extremely long distances through SiO_2 without being absorbed [176, 177]. This makes erbium a useful element for interacting with the optical signals used in the global fiber telecommunications network. Erbium doped fiber amplifiers have played an important role in extending the range and decreasing the cost of large optical data networks [178, 179].

While the long lifetime of the first excited states provides a long time window for inverting a population of erbium ions in a laser or an optical amplifier, it is relatively difficult to excite the ions. The small cross section for optical excitation ($\sim 10^{-21}$ cm^2 in SiO_2) is a consequence of the very small physical size of an erbium ion ($r \sim$Å). The narrow energy bands of erbium also require that the pump wavelength is resonant with a higher lying state of the erbium ion. In practice this increases both the cost and size of erbium-based optical amplifiers, because lasers and long interaction lengths are necessary to invert the desired number of erbium ions.

Silicon nanocrystals have been suggested as a sensitizing intermediary material for erbium-based optical communications devices. Nanocrystals can absorb light much more efficiently than erbium ions, and are not limited to discrete atomic excitation wavelengths. Silicon nanocrystals typically exhibit long photoluminescence decay lifetimes and high quantum efficiency, providing a long time window for energy transfer to indirectly pump erbium. Excitation by energy transfer from silicon nanocrystals gives erbium in silicon nanocrystal doped SiO_2 an effective cross section for optical excitation that is enhanced by up to five orders of magnitude ($\sim 5 \times 10^{-16}$ cm^2) in comparison to erbium in SiO_2. For this reason, silicon nanocrystal sensitized erbium has been extensively studied in recent years [180–201].

Figure 5.1 shows the first few energy levels of an erbium ion in comparison to a typical silicon nanocrystal. A schematic representation of the energy transfer process is drawn in blue. Because the details of this energy transfer process are unclear [202], the optimal fabrication recipe for sensitizing erbium with silicon nanocrystals remains an open question.

In order to develop a recipe for silicon nanocrystal sensitized erbium using CMOS compatible ion implantation processes, we compared the photoluminescence properties of various samples as a function of the nanocrystal formation annealing temperature for six different implantation conditions. Table 5.1 provides a summary of the fabrication process. In all cases, silicon and erbium were implanted into 1 μm oxide films grown by wet thermal

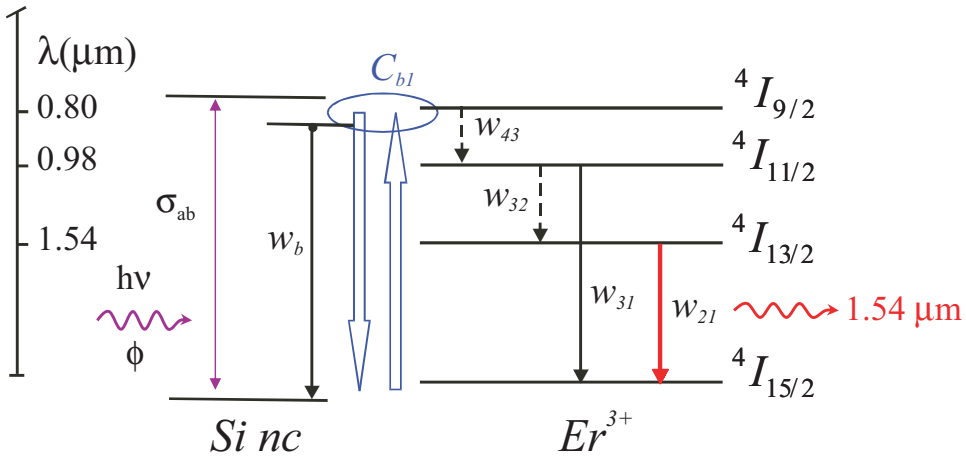

Figure 5.1. This schematic diagram illustrates the nonradiative transfer of energy between an excited silicon nanocrystal and an erbium ion, and the eventual photoluminescence of erbium at 1.53 μm.

oxidation on 100 mm silicon substrates.

Table 5.1. Six samples were prepared using different ion implantation conditions to develop an ion implantation based recipe for silicon nanocrystal sensitized erbium

Erbium Implanted Samples			
	Erbium Dose 300 keV (10^{15} cm^{-2})	Silicon Dose 73 keV (10^{15} cm^{-2})	Target Peak Composition
Wafer 1	1.0×10^{15} cm^{-2}	—	(0.3% Er)
Wafer 2	2.8×10^{15} cm^{-2}	—	(1.0% Er)
Wafer 3	1.0×10^{15} cm^{-2}	5.6×10^{15} cm^{-2}	(0.3% Er + 1% Si)
Wafer 4	2.8×10^{15} cm^{-2}	5.6×10^{15} cm^{-2}	(1.0% Er + 1% Si)
Wafer 5	2.8×10^{15} cm^{-2}	1.7×10^{16} cm^{-2}	(1.0% Er + 3% Si)
Wafer 6	2.8×10^{15} cm^{-2}	5.6×10^{16} cm^{-2}	(1.0% Er + 10% Si)

In past experiments, samples have typically been annealed between the silicon and erbium implantation stages to form silicon nanocrystals. Here we demonstrate that a single annealing process can be used after coimplantation instead. All samples were implanted with erbium first and silicon second at room temperature. The implantation profiles were

designed using SRIM [85] to overlap at a depth of 100 nm. The straggle in the silicon distribution at the implantation energy of 73 keV is 33 nm, while the longitudinal straggle in the erbium depth distribution is 17 nm (300 keV).

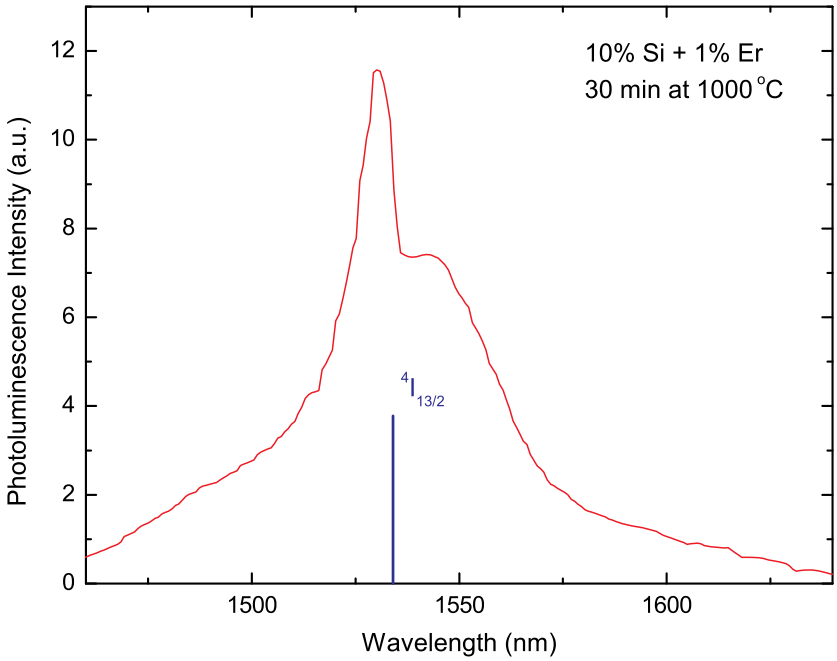

Figure 5.2. A typical photoluminescence spectrum for silicon nanocrystal sensitized erbium in SiO_2 at room temperature.

After the two implantation processes, the samples were annealed in a tube furnace for 30 minutes at various temperatures in an atmosphere of argon and 0.2% O_2. We then measured the photoluminescence spectrum of each sample using a grating spectrometer and a cryogenically cooled Ge diode detector. The samples were pumped with the 488 nm line of an Ar^+ ion laser at $\sim$5 W cm^{-2}. Figure 5.2 shows a typical photoluminescence spectrum for a sample from Wafer 6 that was annealed at 1000 °C. The spectrum shows the characteristic erbium peak at 1.53 μm, homogeneously broadened by the Stark effect in the crystal field of the oxide.

Figure 5.3 shows the compiled photoluminescence intensity data from our parametric study. Noteworthy trends include a decrease in photoluminescence intensity when annealing at very high temperatures, which we attribute to erbium precipitation and clustering. The sample with 1 at. % erbium emits $\sim$3 times more light than the sample with 0.3 at. %

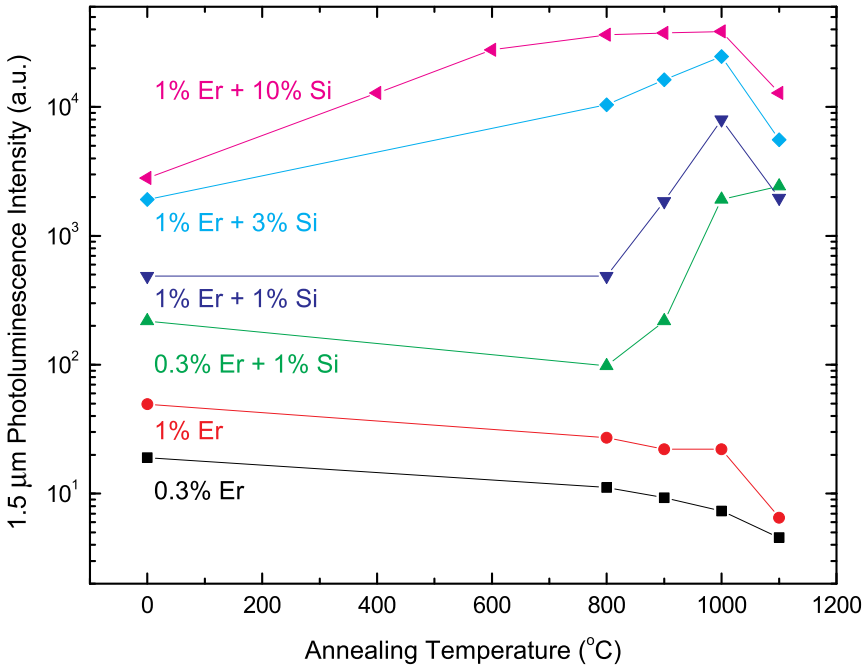

Figure 5.3. The photoluminescence intensity at 1.53 µm is greatly enhanced in samples that are coimplanted with silicon after annealing at high temperature. We find that a high silicon implantation dose provides a better sensitization of the erbium photoluminescence.

erbium as expected. We see the greatest sensitization effect in the sample that contains the most silicon and the highest erbium dose after annealing at 1000 °C. The sensitization factor is ∼800 in comparison to the as-annealed sample from Wafer 2, which contains an identical quantity of erbium. The sensitization factor is nearly 2000 in comparison to a sample from Wafer 2 that was annealed at 1000 °C.

We also measured the improvement in the sensitization factor after a nanocrystal defect passivation annealing process. Samples from each wafer that were annealed at 1000 °C were again annealed in a forming gas atmosphere (10% H_2:N_2) at 500 °C for 30 minutes. The improvement in the erbium photoluminescence sensitization factor is listed in table 5.2. An improvement is only observed after the defect passivation annealing step in samples that are expected to contain silicon nanocrystals. We suggest that nonradiative recombination process associated with surface defect states in the silicon nanocrystals quench energy transfer to erbium ions before the passivation treatment. In our best sample (Wafer 6, 1000 °C), we see a sensitization factor of ∼3900 after passivation.

We also note that we were able to see a strong sensitization effect in samples annealed

Table 5.2. A defect passivation annealing process is observed to improve the sensitization factor in samples that contain silicon nanocrystals

Increase in Er photoluminescence after nanocrystal passivation	
	Enhancement factor
Wafer 1	1.00
Wafer 2	1.00
Wafer 3	1.09
Wafer 4	1.18
Wafer 5	1.41
Wafer 6	2.08

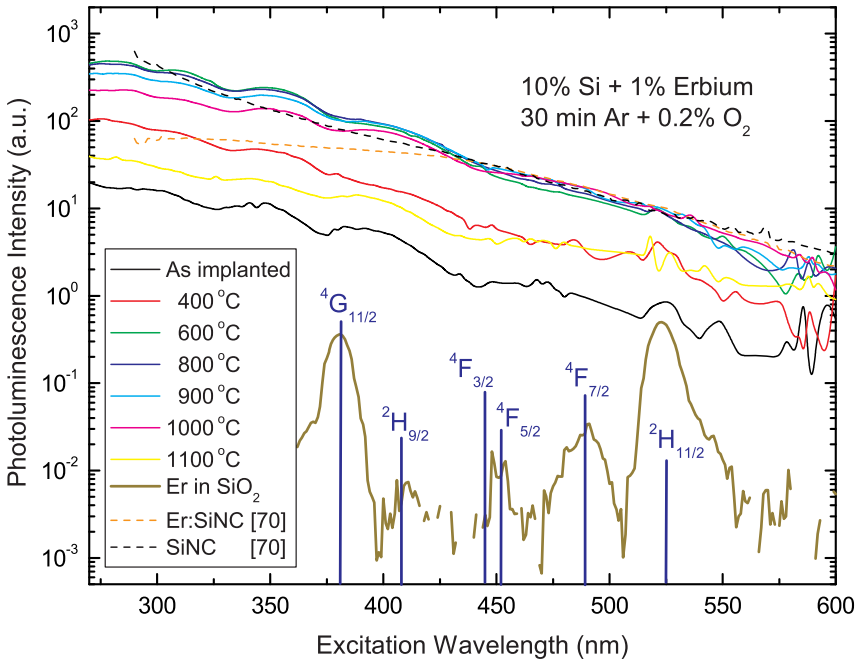

Figure 5.4. Photoluminescence excitation measurements for silicon nanocrystal sensitized erbium demonstrating that erbium emission is observed when exciting off of the atomic resonances of erbium. This is a signature of erbium excitation via energy transfer from silicon nanocrystals

below 800 °C, which is thought to be an approximate threshold for crystallization in silicon nanocrystals [80], Indeed, we see an enhancement of the erbium photoluminescence even in

the as-implanted samples. We believe that small silicon clusters that precipitate during the ion implantation process may be responsible for the sensitization effect in these samples.

Photoluminescence excitation measurements for samples from Wafer 6 suggest that band-to-band absorption in silicon structures leads to erbium emission at 1.53 μm for all annealing temperatures, rather than absorption in any well defined defect energy band (figure 5.4). A measurement of the photoluminescence decay rate of the erbium for each annealing condition could help to confirm that the changes in photoluminescence intensity result from improvements in the effective excitation cross section rather than from an increase in photoluminescence efficiency.

5.3 Erbium Doped FELEDs

Erbium-based optical amplifiers and lasers are typically optically pumped. This is not because erbium is any more difficult to excite electrically than optically. In fact, the cross section for the electrical excitation of erbium ion by impact ionization is typically $\sim 10^{-17}$–10^{-16} cm^2 in bulk silicon [180, 204–206] and up to $\sim 10^{-14}$ cm^2 in silicon nanocrystal doped oxides [207]. This is much larger than the cross section for optical excitation in SiO_2 ($\sim 10^{-21}$ cm^2). However, leakage paths and nonradiative processes limit the power efficiency of electrically pumped erbium light emitting devices to much less than 1%, making them commercially unviable. However, the power efficiency of optically pumped erbium optical amplifiers and lasers is much worse!

The reason that electrically pumped erbium lasers and optical amplifiers have not been produced is that the intensity of the electrical excitation cannot be increased without also increasing the free carrier absorption of the light that is being amplified. It is difficult to pump hard enough to invert the erbium without causing a net loss in the optical signal. The problem of free carrier absorption also plagues optically pumped silicon nanocrystal sensitized erbium optical amplifiers [192, 194]. Any photoexcited excitons that do not decay by transferring energy to the erbium are able to absorb light at 1.5 μm. The maximum net gain observed in an optically pumped silicon nanocrystal sensitized erbium amplifier is typically only a few dB/cm. The cross section for free carrier absorption in silicon is $\sim 10^{-17}$ cm^2 [208], suggesting that the mode to be amplified cannot overlap with an average electron density higher than $\sim 10^{17}$ cm^{-3} without the induced free carrier absorption causing

a net loss.

Field-effect electroluminescence may provide a way to electrically pump erbium while controlling the average density of excess free carriers. The idea is to intermittently create excitons in a silicon nanocrystal layer that will rapidly transfer energy to nearby erbium ions. By carefully controlling the charge injection processes, it may be possible to avoid free carrier absorption in the nanocrystal layer. The overlap of the amplified mode with the device contacts will then become the dominant source of free carrier absorption in the device.

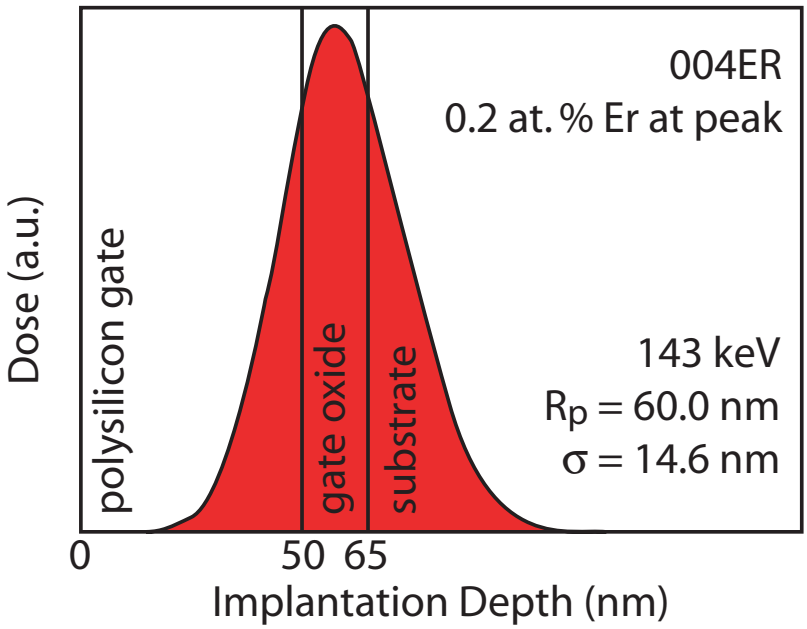

Figure 5.5. Erbium is implanted through the polysilicon gate contact into our FELED structures, targeting the center of the gate oxide and 0.2 peak at. % erbium.

We fabricated a FELED in which erbium could be excited by energy transfer from silicon nanocrystals by implanting erbium through the polysilicon gate contact of our existing devices. The implantation parameters are given in appendix A. Figure 5.5 shows the depth distribution of the implanted erbium as calculated using the SRIM code [85]. While the distribution peaks at the center of the gate oxide, we can anticipate that the broad implantation profile may damage the gate oxide. It would be preferable to implant erbium prior to the deposition of the gate contacts in a future device.

After implantation, the devices were annealed in a tube furnace for 5 min at 1000 °C.

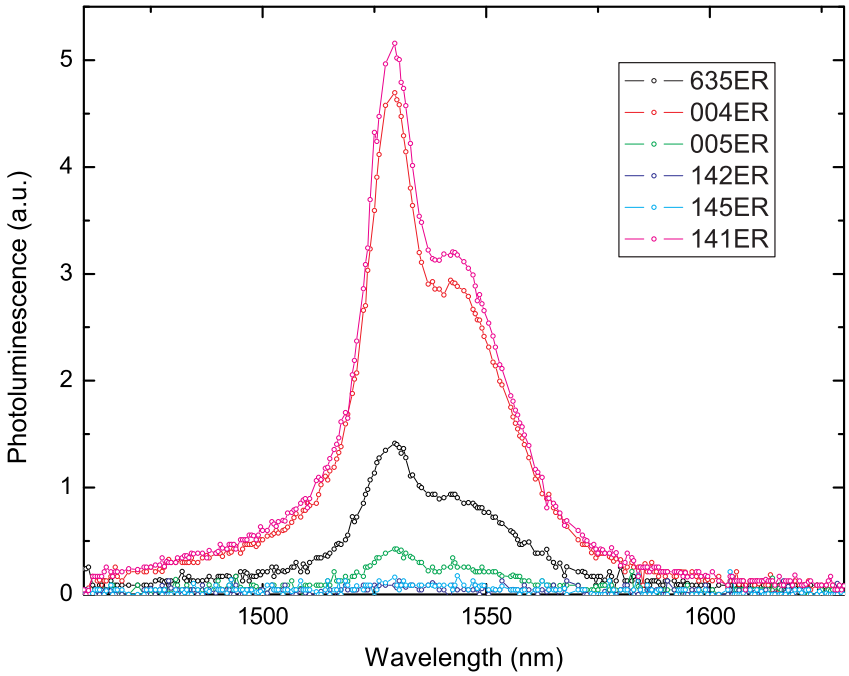

Figure 5.6. Silicon nanocrystal sensitized erbium photoluminescence is observed in coimplanted silicon nanocrystal FELEDs. Control devices (142ER and 145ER) that do not contain silicon nanocrystals emit much less light at 1.53 μm.

None of the erbium implanted devices show near infrared photoluminescence that we can associate with silicon nanocrystals. It is possible that the nanocrystals were heavily damaged during the erbium implantation or that energy transfer to erbium is the dominant recombination mechanism for excitons in the nanocrystal ensemble.

We observe characteristic erbium photoluminescence from the implanted devices that contain silicon nanocrystals when pumping with 488 nm light at ~200 W/cm^2 (figure 5.6). Control samples without silicon nanocrystals show a greatly reduced (~1000x) photoluminescence signal at 1.53 μm. This may indicate that the erbium photoluminescence is sensitized by silicon nanocrystals or perhaps by smaller silicon clusters or defect structures that remain after the ion implantation process.

As we observed for silicon nanocrystal photoluminescence in our optical memory experiments, the steady state erbium photoluminescence can be quenched by an applied gate bias. Figure 5.7 shows a comparison of the normalized steady state photoluminescence signals observed while a gate bias is applied. The quenching of the erbium signal is not as pronounced as the decrease in the silicon nanocrystal signal we observe in a FELED that

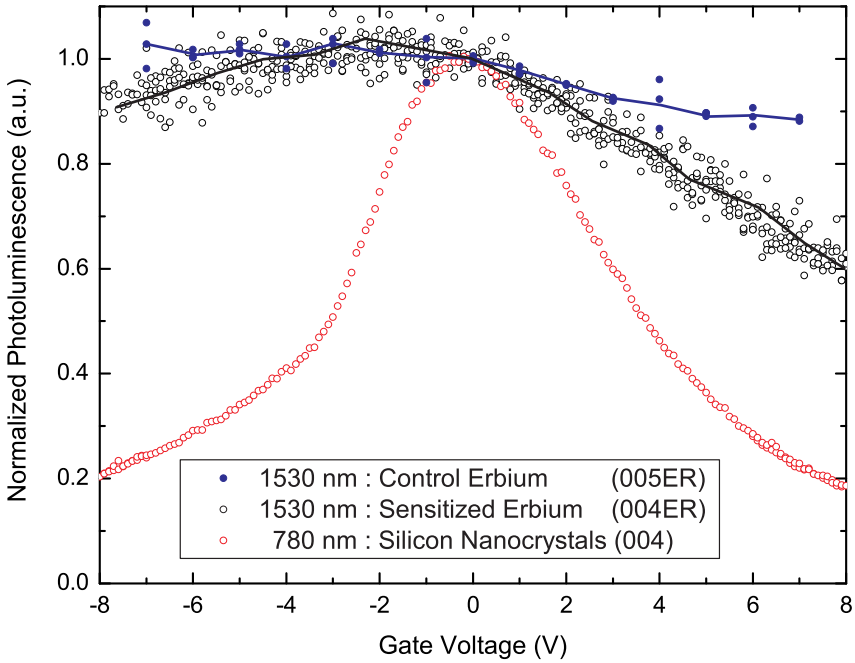

Figure 5.7. Silicon nanocrystal sensitized erbium photoluminescence decreases under an applied gate bias, but is not quenched as easily as the silicon nanocrystal signal in unimplanted devices.

has not been implanted with erbium. The response seems to be stronger for positive gate biases. We also note a small decrease in the photoluminescence of erbium in the implanted control devices at positive gate biases.

These results may indicate that a leakage current through the gate oxide decreases the erbium photoluminescence intensity under positive gate bias conditions. The leakage current could be expected to be smaller for negative gate biases because the gate stack acts as an *np*-junction diode connecting the gate to the substrate. It is tempting to suggest that the remaining symmetric quenching phenomenon observed for the sensitized samples is related to charging processes in the nanocrystal ensemble. In this view, Auger recombination in charged nanocrystals reduces the exciton population that can transfer energy to erbium.

The reduced impact of the Auger recombination on the erbium photoluminescence signal in comparison to the quenching of the silicon nanocrystal photoluminescence may suggest that energy transfer occurs on a very fast time scale. Direct measurements of the energy transfer rate between silicon nanocrystals and erbium have suggested that there are two characteristic time scales [76, 100, 185, 187, 189, 197, 209–211]. The slow energy trans-

fer process is usually associated with the Förster dipole-dipole interaction and occurs on microsecond time scales. The fast component is less understood, but is characterized by ∼100 ns time scales. If the erbium in our nanocrystal sensitized samples is excited by the fast energy transfer component, the reduced quenching efficiency of the Auger process could be explained in terms of competition between the two recombination processes.

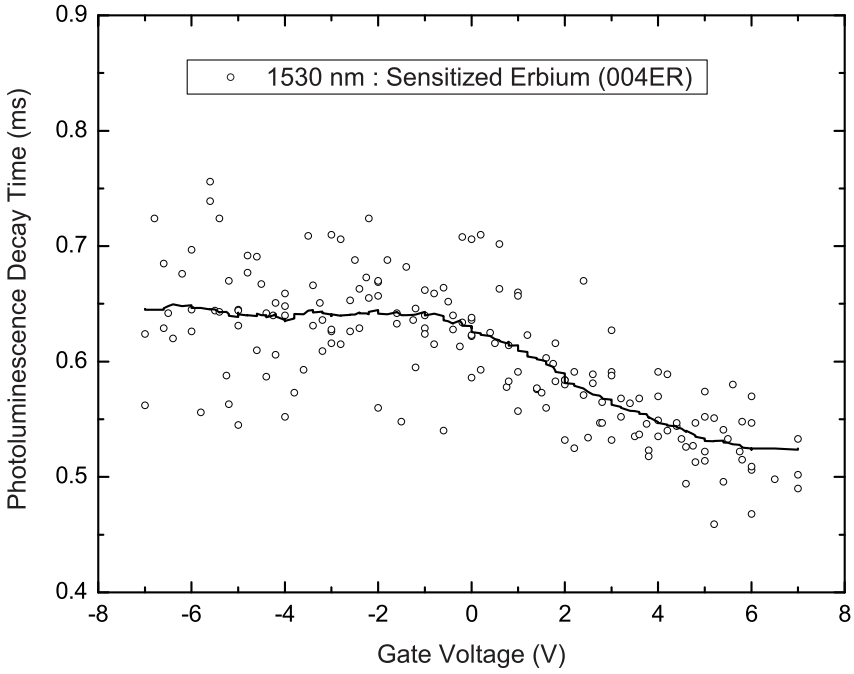

Figure 5.8. The photoluminescence decay lifetime for silicon nanocrystal sensitized erbium decreases by ∼10% at positive gate biases. No decrease in the lifetime is observed at negative bias conditions.

We also measured the erbium photoluminescence decay lifetime in our nanocrystal sensitized erbium implanted FELED (figure 5.8). For these measurements, the sample was pumped with 488 nm light at ∼200 W/cm^2 that was abruptly switched off using an acousto-optic modulator. The signal was recorded using a cryogenically cooled Ge diode detector with a response time constant of ∼30 μs. The diode signal was amplified and converted to a pulse train using a voltage controlled oscillator and the signal was recorded using multi-channel scalar. Each decay trace was fit with a single exponential decay function to extract the $1/e$ lifetime.

We note that the decay lifetime (∼600 μs) is shorter than the lifetimes typically observed

for erbium in SiO_2. Much of this discrepancy can be attributed to the high local density of optical states in our device for 1.5 μm emission at the location of the erbium ions in the gate oxide. It is also possible that concentration quenching is decreasing the quantum efficiency of radiative emission. The photoluminescence decay lifetime decreases by up to ∼10% when the implanted FELED is biased with a positive gate voltage. We suggest that this could be caused by a leakage current and could be the cause of the decrease in the erbium photoluminescence intensity that we observe in control samples that do not contain silicon nanocrystals. Because the lifetime of the erbium is constant at negative gate bias, we must conclude that the decrease in photoluminescence intensity seen in the sensitized samples for negative bias conditions results from a decrease in the effective excitation cross section. This is consistent with our suggestion that sensitization occurs by energy transfer from silicon nanocrystals and that Auger recombination in charged nanocrystals decreases the efficiency of the indirect excitation process.

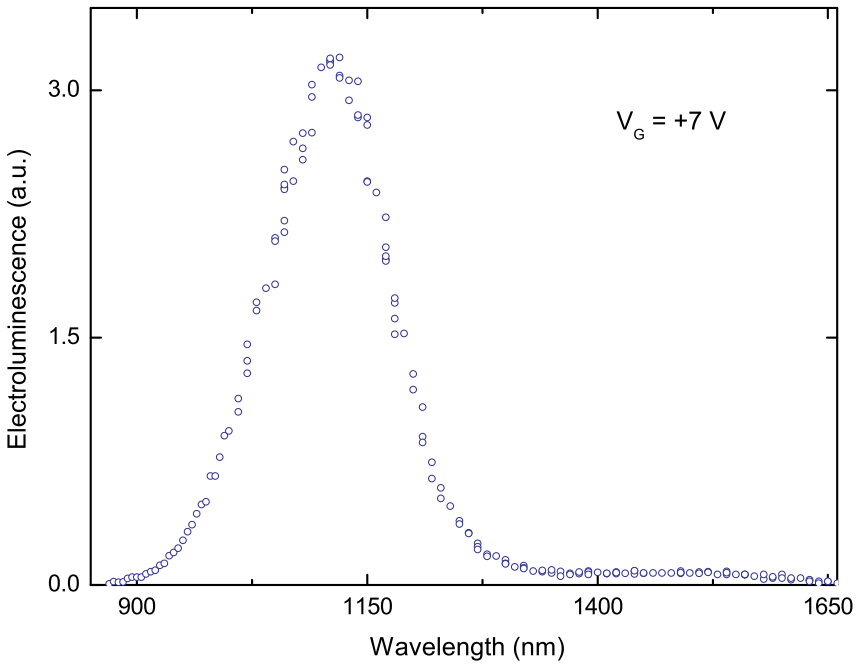

Figure 5.9. The coimplanted FELEDs emit bandedge electroluminescence at positive gate bias, suggesting implantation has damaged the gate oxide. No field-effect electroluminescence has been observed at 1530 nm (erbium) or at 780 nm (silicon nanocrystals).

We have not observed electroluminescence that we can associate with erbium or silicon

nanocrystals in any of the implanted FELED samples. It is possible that the ion implantation process damaged the devices to the extent that field-effect electroluminescence can no longer excite the silicon nanocrystals. However, we do see electroluminescence for positive gate voltages that can be attributed to band-to-band recombination in the silicon channel (figure 5.9) when the gate is biased at a positive voltage. This supports our suggestion that the gate oxide has been damaged by the ion implantation process and that a leakage current is present.

While this first attempt at creating a FELED that can excite erbium was unsuccessful, we see no obstacles to making functional devices with an improved fabrication method.

5.4 Energy Transfer to PbSe Nanocrystals

Solution processed IV–VI semiconductor quantum dots like PbS and PbSe are attractive for photonic applications because they exhibit size-tunable quantum confined emission across a large range of the infrared spectrum, including the 1.3 μm and 1.5 μm optical telecommunications bands [212]. Lead selenide nanocrystals have a large optical cross section for optical excitation ($\sim 10^{-15}$ cm^2 at 488 nm), a fast radiative recombination rate ($\sim$10 MHz), and high quantum efficiency in solution. They have also recently attracted a lot of interest for exhibiting multiexciton generation, a phenomenon in which a single photon is absorbed to create more than one exciton [213, 214]. Previously PbSe and PbS nanocrystal light emitting devices have been fabricated with organic conducting layers [215, 216]. However, these nanocrystals may be difficult to directly incorporate into inorganic solid-state devices, because they are typically passivated by organic ligands that are very sensitive to heat.

We investigated the possibility of integrating solution processed PbSe nanocrystals with our silicon nanocrystal FELED to make an electrically pumped infrared light emitting device. In the same way that energy transfer allows silicon nanocrystals to be used as an indirect excitation channel for erbium ions, energy transfer should result in the excitation of PbSe quantum dots that are very close to the silicon nanocrystals (figure 5.10). Similar experiments with CdSe quantum dots that are excited by energy transfer from a nearby quantum well are encouraging [218]. The energy transfer rate is predicted to scale as the geometric mean of the radiative recombination rates for the donor (in our system, the silicon nanocrystal) and the acceptor (erbium or PbSe) [217]. This suggests that energy transfer

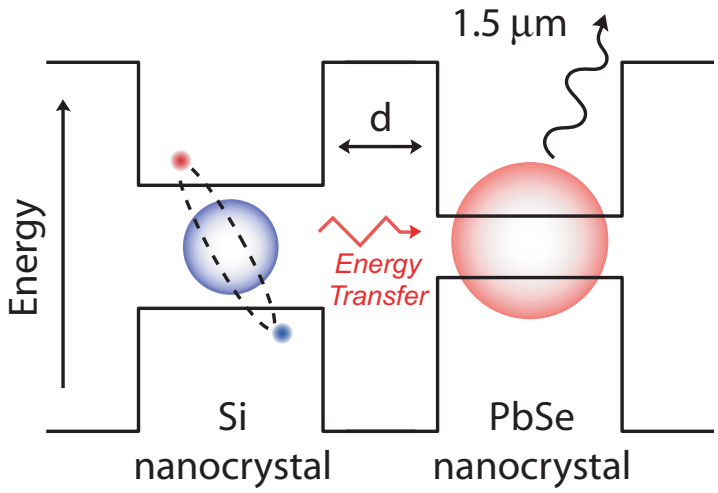

Figure 5.10. Energy transfer should be possible between silicon nanocrystals and nearby PbSe nanocrystals below some critical distance, *d*.

to PbSe will be a very rapid relaxation pathway for excitons in silicon nanocrystals.

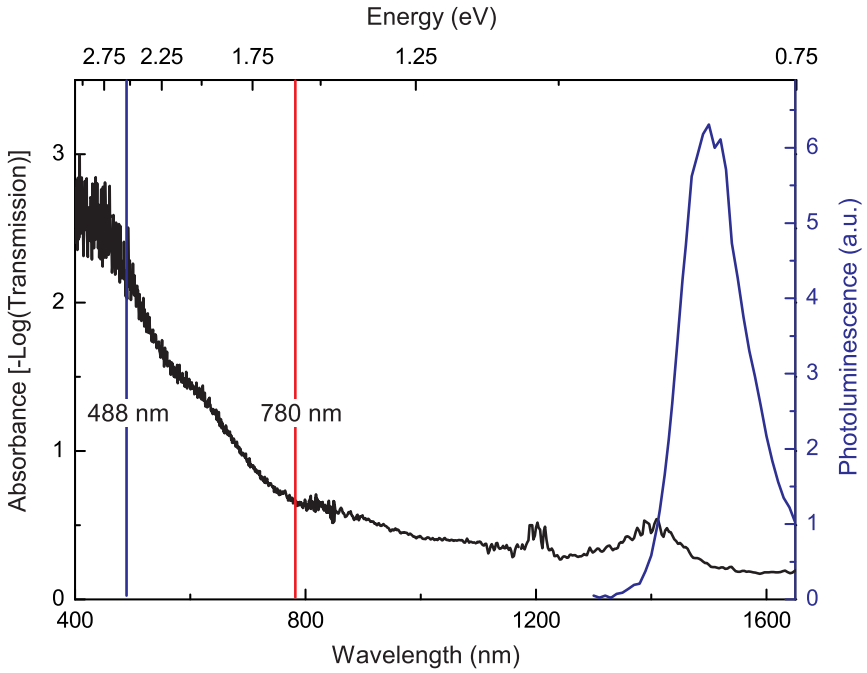

Figure 5.11. Measured photoluminescence and absorption data for solution synthesized PbSe quantum dots.

We purchased PbSe quantum dots in a hexane solution from a commercial vendor for this study. The photoluminescence spectrum for drop cast PbSe nanocrystals is show in

figure 5.11 along with the measured absorption spectrum. The dots emit in a band around 1500 nm with a full width at half maximum of ∼100 nm. From the absorption spectrum and the optical cross section at 488 nm, we can estimate that the cross section for optical excitation of the PbSe dots at the emission wavelength of the silicon nanocrystals (∼780 nm) is $\sim 3 \times 10^{-17}$ cm^2. We can safely conclude that we will not measure any photoluminescence from the PbSe caused by optical pumping by the electroluminescence of the silicon nanocrystals in the FELED. Efficient energy transfer processes are a prerequisite for any observable infrared electroluminescence from our hybrid PbSe nanocrystal FELED.

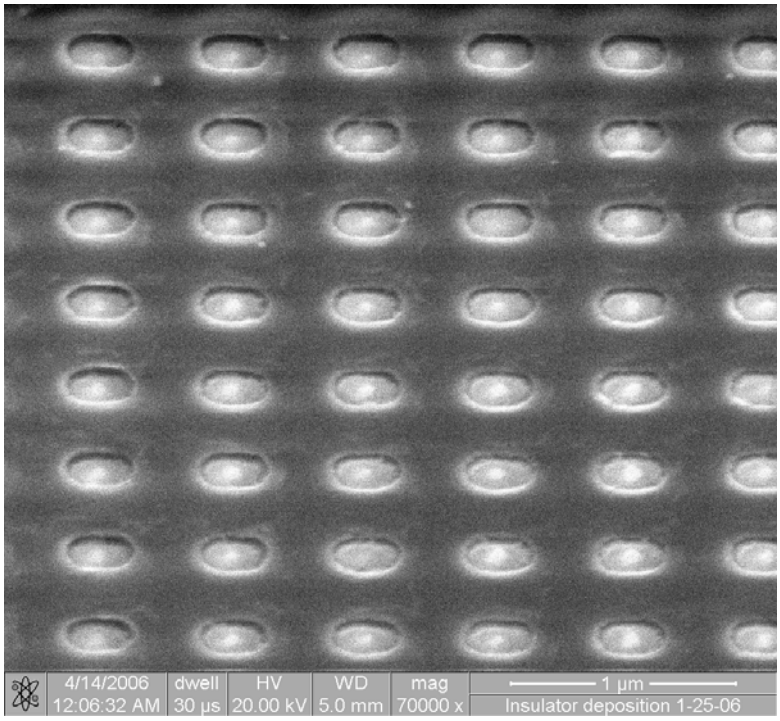

Figure 5.12. Scanning electron microscopy of a FELED gate contact after patterning by focused ion beam milling.

The critical distance for energy transfer processes is typically of order 1 nm, but the silicon nanocrystals in our FELED are buried in the gate oxide underneath the 50 nm thick polysilicon gate contact. In order to position the PbSe nanocrystals closer to the silicon nanocrystal ensemble, the gate contact must be partially removed. We first tried a cyclical etching procedure. Samples were alternately immersed in RCA-2 solution ($HCl:H_2O_2:H_2O$ 1:1:6, 70 °C) to oxidize ∼1 nm of polysilicon and in buffered HF to remove the oxide layer. This procedure reduced the gate thickness by 8.5 Åper cycle as determined through spectral

ellipsometry. However, we found that the etching rate became unstable due to pitting after ~10 cycles. We proceeded by patterning the gate contact with a dense array of holes using a focused ion beam mill. In order to limit the potential for damaging the gate oxide or the nanocrystal array, we experimented with supplementing the ion beam milling process with XeF_2 gas applied in situ through a small nozzle. We found that the native oxide on the surface of the polysilicon could act as a natural mask for the gas phase etch. By removing only ~5 nm of material with the ion beam, we are able to rapidly write very large areas (200,000 holes filling 200 mm^2 in 1 hour). A ~30 second application of XeF_2 was then used to simultaneously etch away all of the polysilicon areas where the native oxide was removed. A scanning electron microscopy image of the device after patterning is shown in figure 5.12.

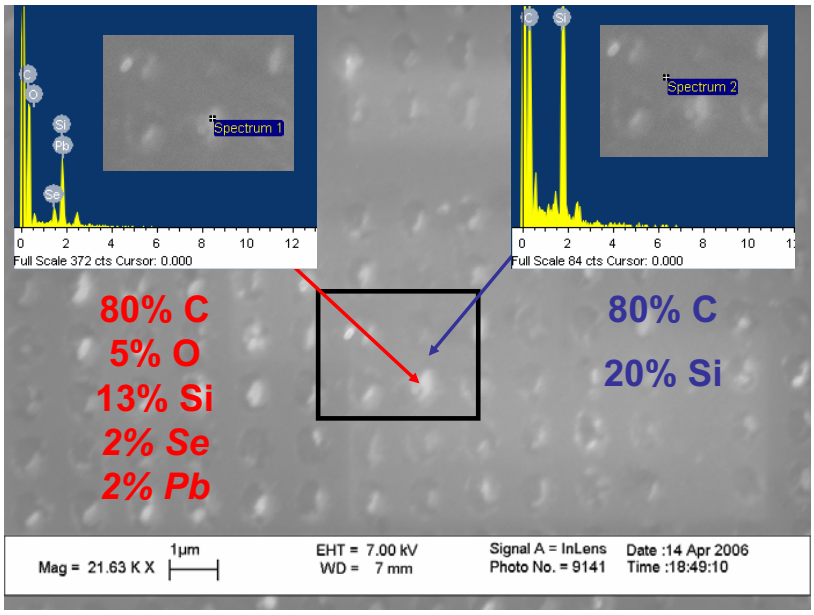

Figure 5.13. X-ray spectroscopy reveals PbSe nanocrystals inside the pattern of holes made in a FELED gate contact after drop casting.

We then drop cast the PbSe nanocrystals on top of the patterned gate contact structures. Using energy dispersive X-ray spectroscopy (EDS, figure 5.13) we were able to verify that PbSe nanocrystals are present at the bottom of the holes patterned in the gate contact. However we have not yet observed electroluminescence that we can associate with the PbSe nanocrystals in these devices. It is possible that the silicon nanocrystals at the perimeter of the holes are no longer electrically excited. Alternatively, the quantum efficiency of the PbSe quantum dots might be too low after drop casting on the patterned FELED device. It

may be possible to further etch the device to partially remove the gate oxide layer in an attempt to further reduce the distance separating the silicon nanocrystal ensemble and the PbSe quantum dots.

5.5 Conclusion

While silicon nanocrystals cannot emit light at energies below the bandgap of bulk silicon, they may be useful in hybrid devices as sensitizers that pass energy to secondary emitters by energy transfer. When this concept is applied to the FELED, it becomes possible to envision electrically pumped nanocrystal sensitized sources operating at telecommunications wavelengths.

Chapter 6

Outlook

There are many open questions remaining to be answered concerning silicon nanocrystals. In this chapter, we identify some experiments that could clarify our understanding. We also highlight a few ideas and devices suggested by our work.

1. Concentration effects in silicon nanocrystal ensembles.

   As described in chapter 2, the photoluminescence decay dynamics of dense ensembles of silicon nanocrystals are suspected to be dominated by efficient internanocrystal energy transfer processes. The details of these processes have been essentially swept under the rug by the widespread use of the stretched exponential function to describe time-resolved photoluminescence measurements. The development of a physical model that predicts the dynamics of photoluminescence is an important challenge for the silicon nanocrystal research community. However, the existing data set is not sufficient to distinguish between the different models that have been proposed. There is a good opportunity for the right experiment to have a significant impact on the discussion.

   Our method of measuring the decay rate while changing the local density of optical states would provide a powerful experimental protocol for reexamining photoluminescence decay in silicon nanocrystals. In particular, we suggest a study in which the concentration of nanocrystals embedded in a staircase-etched oxide is controlled by varying the implantation dose over several samples. An extensive data set could be collected by monitoring the decay lifetime as a function of wavelength, local density of states, excitation rate, and concentration. These data could then be used to construct an improved model for energy transfer processes in silicon nanocrystal ensembles.

2. Developing an internal quantum efficiency metrology protocol for materials evaluation.

   The internal quantum efficiency for radiation is an important measure of sample quality for all optical materials. It would be useful to develop an optimized standard

staircase-etched substrate that could be used to quickly measure the local density of optical states dependent photoluminescence dynamics for any deposited thin-film material layer. With further development, our internal quantum efficiency measurement could become a routine tool that could be used to optimize fabrication recipes.

3. Time-resolved bandedge electroluminescence in a silicon nanocrystal FELED.

   The bandedge electroluminescence signal observed in our silicon nanocrystal FELED deserves further study. We have suggested that light emission occurs only for gate bias transitions that correspond to the collapse of the inversion layer in the channel. Time-resolved measurements will be able to establish whether this is actually the case. These measurements may also clarify the contribution of stored charges to the band edge signal. The decay of the anticipated band edge electroluminescence pulse may correspond to the discharging time scale for the nanocrystal ensemble if the stored charge contributes directly to recombination. If the light is generated only by the inversion layer electrons, the decay dynamics may be more rapid. It might also be interesting to look for bandedge electroluminescence in the control devices that do not have nanocrystals in the gate oxide.

4. Temperature dependent electroluminescence in a silicon nanocrystal FELED.

   The field-effect electroluminescence mechanism has so far provided an adequate conceptual framework for our experiments, but the underlying carrier transport mechanism is unclear. Simulations suggest that tunneling processes would be too slow to explain the time constants that we observe. If transport instead occurs by charge hopping between defect states in the gate oxide, we should be able to measure a characteristic exponential temperature dependence in the electroluminescence signal. For example, in Poole-Frenkel conduction [172, 175], the current density is:

$$J_{P-F} = \mathrm{q}_e n_0 \mu \mathcal{E}_N exp\left[-\frac{\mathrm{q}_e}{\mathrm{k}T}\left(\phi_B - \sqrt{\frac{\mathrm{q}_e \mathcal{E}_N}{\pi \epsilon_N}}\right)\right],$$

   where the current density ϕ_B is the barrier height and $\mathcal{E}_N$ is the electric field in the oxide.

   In this experiment, the silicon nanocrystal FELED would be mounted in a cryostat and the optoelectronic characterization performed for this thesis would be repeated

at a range of low temperatures. It will be important in this work to carefully account for the known temperature dependent emission characteristics of silicon nanocrystals caused by the singlet-triplet exchange interaction in the excitons.

5. Field-effect electroluminescence in nonsilicon quantum dots.

   We have suggested that field-effect electroluminescence could be used to electrically pump nonsilicon semiconductor quantum dots. However, the mechanism may rely on some particular material property of silicon or SiO_2. It would be interesting to design and fabricate FELEDs using III–IV or IV–VI quantum dots to demonstrate that we have indeed developed a new general class of light emitting devices. In view of the performance limits calculated in section 4.11, a FELED that contained direct gap nanocrystals seems especially promising.

6. Single photon electroluminescence in a silicon nanocrystal FELED.

   Our devices were intentionally fabricated with large gate contact pads in order to allow convenient access to the silicon nanocrystal ensemble with free space optics. It would be interesting to scale a silicon nanocrystal FELED down to the very small device area regime. We suggest that this could be accomplished by focused ion beam milling. Our existing devices could be nearly arbitrarily reduced in size by defining reduced gate contact pad regions within the existing polysilicon gate layer. It should be straightforward to make a FELED with a gate area less than 100 nm^2. At this size scale, it is statistically possible to address a single silicon nanocrystal.

   If field-effect electroluminescence were accomplished at the single nanocrystal level, we could observe electrically pumped "photon on demand" single photon light emission. By further controlling the injection of additional carriers, it may even be possible to drive the emission into a regime where the statistics are determined by the gate bias modulation rather than by the spontaneous emission lifetime. One method would involve intentionally quenching the exciton shortly after creating it in the nanocrystal by injecting an additional carrier to induce Auger recombination.

7. An extensive parametric study of silicon nanocrystal FELED electroluminescence.

   In this thesis, we have studied fewer than 1% of the FELED devices that were fabricated during our collaboration with Intel Corporation. We have now developed a suite of

experimental methods that are ready to be applied in a systematic way to more of this sample set. In particular, it would useful to identify and explain trends that are correlated with device area and shape, gate oxide thickness, and implantation conditions.

Imaging the electroluminescence of larger devices at different operating frequencies might reveal if electron drift velocity is important in the charge injection process. Larger devices might exhibit reduced electroluminescence at the center of the gate contact pad.

Finally, we suggest attempting a time-resolved measurement of the first few cycles of electroluminescence to look for nonequilibrium light emission processes. For example, the gate bias could be held at -6 V for several seconds before applying series of 100 μs alternating bias pulses. In these measurements, the transient photoluminescence measurements made during our optical memory experiments should provide a useful guideline for choosing sufficiently long gate bias dwell times. Based on the signal levels we have observed in steady state for modulation at 1 kHz, this type of measurement should be practical with integration times of order 10 min.

8. A FELED pumped silicon nanocrystal sensitized erbium laser.

   An electrically pumped silicon compatible laser is a "holy grail" in silicon photonics. We propose that silicon nanocrystal sensitized erbium could be used as an electrically pumped gain medium in a waveguide integrated FELED structure (figure 6.1). The low index of refraction of silicon nanocrystal doped SiO_2 in comparison to silicon and other potential electrical contact materials suggests the use of a "slot waveguide" design [219]. In this structure, the guided mode can be highly confined in a low index region.

   The slot waveguide structure is ideally suited for the field-effect electroluminescence mechanism. The gate oxide of the FELED will form the slot while the gate contact and a thin film substrate will form the cladding layers. The long decay lifetime of erbium should allow the gain medium to be inverted by intermittent electrical pumping. It will be very important to control losses in the contact cladding layers in order to achieve net gain.

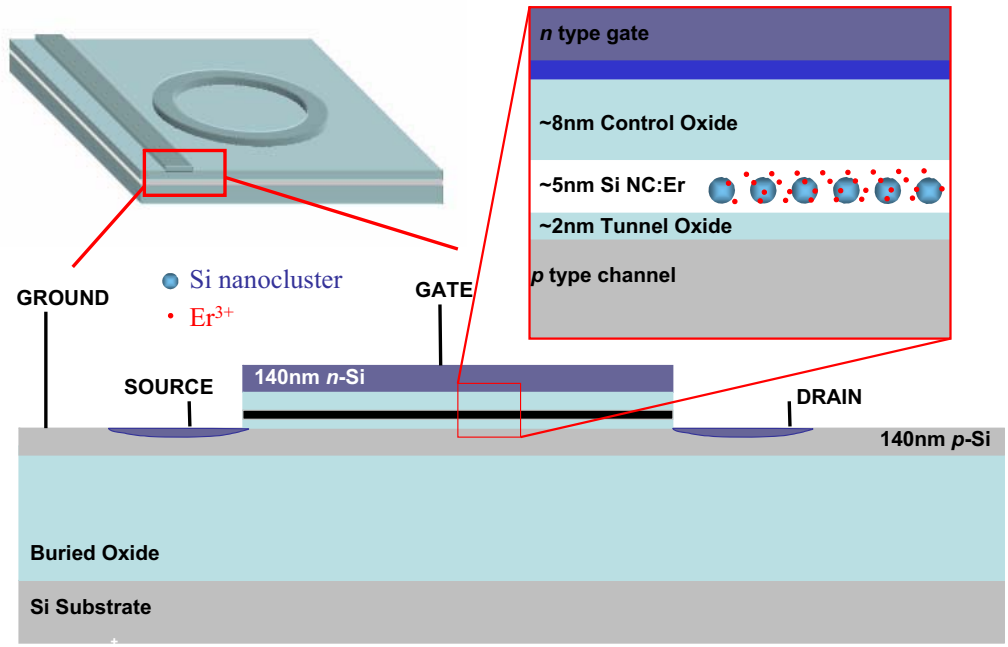

Figure 6.1. A schematic diagram of an electrically pumped silicon nanocrystal sensitized erbium horizontal slot waveguide laser. The erbium ions are pumped by energy transfer from nanocrystals that are excited by field effect electroluminescence.

In this thesis, we have demonstrated that silicon nanocrystals embedded in SiO_2 constitute a fully CMOS compatible optical material system. We have shown through photoluminescence experiments that dense silicon nanocrystal ensembles can be formed in well defined layers using ion implantation, and that these layers can emit light with very high internal quantum efficiency. We have fabricated optoelectronic devices that have allowed us to experimentally contribute to the understanding of charge dependent processes in silicon nanocrystal ensembles. And finally, we have discovered and developed a new electrical excitation mechanism that significantly adds to the promise of silicon nanocrystals for silicon photonics.

Appendix A

Fabrication Split Charts

Table A.1. Split chart for 300 mm wafers fabricated for the Caltech-Intel Silicon Nanocrystal Optical Memory collaboration.

Wafer ID #	Gate Oxide Thickness (nm)	Implant Energy (keV)	Si Implant Fluence (10^{16} cm^{-2})	Implant Depth (nm)	Peak Silicon Atomic % Excess (%)	RTA Anneal Time (sec) (1080 °C; 2% O_2)	Gate Poly Thickness (nm)
744	80	–	–	–	–	–	–
743	160	–	–	–	–	–	–
430	15	5	0.65	10	10	spike	–
431	15	5	0.65	10	10	30	–
432	15	5	0.65	10	10	90	–
598	15	5	0.95	10	15	300	–
625	15	5	1.27	10	20	300	–
626	15	5	1.27	10	20	300	50
628	15	5	1.27	10	20	300	50
629	15	5	1.27	10	20	300	50
633	15	5	1.27	10	20	300	50
634	15	5	1.27	10	20	300	50
635	15	5	1.27	10	20	300	25
640	15	5	1.27	10	20	300	25
004	15	5	1.27	10	20	300	50
005	15	–	–	–	–	–	50
006	15	–	–	–	–	–	50
139	25	7	1.5	13	20	300	50
141	25	7	1.5	13	20	300	50
142	25	–	–	–	–	–	50
143	25	–	–	–	–	–	50
144	25	7	1.15	13	15	300	50
145	8	–	–	–	–	–	50
147	8	–	–	–	–	–	50
148	8	1.5	0.5	4	15	300	50
149	8	1.5	0.33	4	10	300	50

Table A.2. Split chart for erbium doped samples.

Er Doped Sample ID #	Gate Thickness (nm)	Oxide Thickness (nm)	NCs?	Er Implant Fluence (10^{14} cm^{-2})	Implant Energy (keV)	Peak Erbium Concentration (at. %)	Furnace Anneal Time (sec) (1000 °C; 0.2% O_2)
004ER	50	15	Yes	5.81	143	0.2	300
005ER	50	15	No	5.81	143	0.2	300
141ER	50	25	Yes	5.51	180	0.2	300
142ER	50	25	No	5.51	180	0.2	300
145ER	50	8	No	5.96	123	0.2	300
635ER	25	15	Yes	3.86	57	0.2	300

Appendix B

Master Equation Simulator Code

(* Population vector : 0, n, p, nn, pn, pp, nnp, ppn, pnpn *)

$$
\begin{aligned}
NanocrystalDensity &= 5 * 10^{12}\ \text{NCs/cm}^2 \\
\tau_{radiative} &= 1 * 10^{-5}\ \text{seconds} \\
\tau_{Auger,n} &= 1 * 10^{-9}\ \text{seconds} \\
\tau_{Auger,p} &= 3 * 10^{-9}\ \text{seconds} \\
State[t] &= (S_{00}[t], S_{10}[t], S_{01}[t], S_{20}[t], S_{11}[t], S_{02}[t], S_{21}[t], S_{12}[t], S_{22}[t]) \\
Holes[t] &= (0,0,1,0,1,2,1,2,2) \cdot State[t] \\
Electrons[t] &= (0,1,0,2,1,0,2,1,2) \cdot State[t] \\
q[t] &= Holes[t] - Electrons[t] \\
q_{eff}[t] &= (0,1,-1,2,0,-2,1,-1,0) \cdot q[t]/NanocrystalDensity \\
f[tau] &= \frac{1}{\tau * 10^{-6}} (*charges/NC/sec*) \\
J_{e,f}[t] &= f\,[(\ 10,\ 100,\ 0.1,\ 0,\ 10,\ 0.01,\ 100,\ 0.1,\ 10)] \\
J_{e,r}[t] &= f\,[(\ 0,\ 10,\ 0,\ 0.1,\ 0,\ 0,\ 10,\ 0,\ 0)] \\
J_{h,r}[t] &= f\,[(\ 0,\ 0,\ 100,\ 0,\ 0,\ 10,\ 0,\ 100,\ 0)] \\
J_{h,f}[t] &= f\,[(\ 100,\ 10,\ 1000,\ 1,\ 100,\ 0,\ 10,\ 1000,\ 100)]
\end{aligned}
$$

$$\Gamma_{radiative}[t] = \begin{pmatrix} 0 & 0 & 0 & 0 & 1/\tau_{radiative} & 0 & 0 & 0 & 0 \\ 0 & 0 & 0 & 0 & 0 & 0 & 2/\tau_{radiative} & 0 & 0 \\ 0 & 0 & 0 & 0 & 0 & 0 & 0 & 2/\tau_{radiative} & 0 \\ 0 & 0 & 0 & 0 & 0 & 0 & 0 & 0 & 0 \\ 0 & 0 & 0 & 0 & -1/\tau_{radiative} & 0 & 0 & 0 & 4/\tau_{radiative} \\ 0 & 0 & 0 & 0 & 0 & 0 & 0 & 0 & 0 \\ 0 & 0 & 0 & 0 & 0 & 0 & -2/\tau_{radiative} & 0 & 0 \\ 0 & 0 & 0 & 0 & 0 & 0 & 0 & -2/\tau_{radiative} & 0 \\ 0 & 0 & 0 & 0 & 0 & 0 & 0 & 0 & -4/\tau_{radiative} \end{pmatrix}$$

$$\Gamma_{Auger}[t] = \begin{pmatrix} 0 & 0 & 0 & 0 & 0 & 0 & 0 & 0 & 0 \\ 0 & 0 & 0 & 0 & 0 & 0 & 1/\tau_{Auger,n} & 0 & 0 \\ 0 & 0 & 0 & 0 & 0 & 0 & 0 & 1/\tau_{Auger,p} & 0 \\ 0 & 0 & 0 & 0 & 0 & 0 & 0 & 0 & 0 \\ 0 & 0 & 0 & 0 & 0 & 0 & 0 & 0 & 2/\tau_{Auger,n} + 2/\tau_{Auger,p} \\ 0 & 0 & 0 & 0 & 0 & 0 & 0 & 0 & 0 \\ 0 & 0 & 0 & 0 & 0 & 0 & -1/\tau_{Auger,n} & 0 & 0 \\ 0 & 0 & 0 & 0 & 0 & 0 & 0 & -1/\tau_{Auger,p} & 0 \\ 0 & 0 & 0 & 0 & 0 & 0 & 0 & 0 & -2/\tau_{Auger,n} - 2/\tau_{Auger,p} \end{pmatrix}$$

$$J_{+6}[t] = \begin{pmatrix} -J_{e,f_1} & 0 & J_{h,r_3} & 0 & 0 & 0 & 0 & 0 & 0 \\ J_{e,f_1} & -J_{e,f_2} & 0 & 0 & J_{h,r_5} & 0 & 0 & 0 & 0 \\ 0 & 0 & -J_{h,r_3} - J_{e,f_3} & 0 & 0 & J_{h,r_6} & 0 & 0 & 0 \\ 0 & J_{e,f_2} & 0 & 0 & 0 & 0 & J_{h,r_7} + J_{e,f_7} & 0 & 0 \\ 0 & 0 & J_{e,f_3} & 0 & -J_{h,r_5} - J_{e,f_5} & 0 & 0 & J_{h,r_8} & 0 \\ 0 & 0 & 0 & 0 & 0 & -J_{h,r_6} - J_{e,f_6} & 0 & 0 & 0 \\ 0 & 0 & 0 & 0 & J_{e,f_5} & 0 & -J_{h,r_7} - J_{e,f_7} & 0 & J_{h,r_9} + J_{e,f_9} \\ 0 & 0 & 0 & 0 & 0 & J_{e,f_6} & 0 & -J_{h,r_8} - J_{e,f_8} & 0 \\ 0 & 0 & 0 & 0 & 0 & 0 & 0 & J_{e,f_8} & -J_{h,r_9} - J_{e,f_9} \end{pmatrix}$$

$$J_{-6}[t] = \begin{pmatrix} -J_{h,f_1} & J_{e,r_2} & 0 & 0 & 0 & 0 & 0 & 0 & 0 \\ 0 & -J_{e,r_2} - J_{h,f_2} & 0 & J_{e,r_4} & 0 & 0 & 0 & 0 & 0 \\ J_{h,f_1} & 0 & -J_{h,f_3} & 0 & J_{e,r_5} & 0 & 0 & 0 & 0 \\ 0 & 0 & 0 & -J_{h,f_4} - J_{e,r_4} & 0 & 0 & 0 & 0 & 0 \\ 0 & J_{h,f_2} & 0 & 0 & -J_{e,r_5} - J_{h,f_5} & 0 & J_{e,r_7} & 0 & 0 \\ 0 & 0 & J_{h,f_3} & 0 & 0 & 0 & 0 & J_{e,r_8} + J_{h,f_8} & 0 \\ 0 & 0 & 0 & J_{h,f_4} & 0 & 0 & -J_{e,r_7} - J_{h,f_7} & 0 & 0 \\ 0 & 0 & 0 & 0 & J_{h,f_5} & 0 & 0 & -J_{e,r_8} - J_{h,f_8} & J_{e,r_9} + J_{h,f_9} \\ 0 & 0 & 0 & 0 & 0 & 0 & J_{h,f_7} & 0 & -J_{e,r_9} - J_{h,f_9} \end{pmatrix}$$

Given the previous definitions, the simulator runs with the following Mathematica Code:

```
OperatingFrequency = 10000; (*frequency to simulate in kHz*)
SimTime = 1/2/ OperatingFrequency; (* seconds *)
ListInterval = 0.01;
μ = Range[−9, Log[10, SimTime], ListInterval];
A = N[%, 5];

(*1 : Governing equation for initial charging with electrons, positive gate bias,
assume full hole charge *)
(* Population vector : 0, n, p, nn, pn, pp, nnp, ppn, pnpn *)
Eqnlist = {
Inner[ Equal, State′[t], Evaluate[( JP6[t] + RadiativeD[t] + AugerD[t]). State[t]], List],
Inner[ Equal, State[0], {0, 0, 5, 0, 0, 0, 0, 0, 0}, List]
} // Flatten;
solution1 = NDSolve[ ReleaseHold[ Eqnlist],
{ S00[t], S10[t], S01[t], S20[t], S11[t], S02[t], S21[t], S12[t], S22[t]}, {t, 0, SimTime},
StartingStepSize → 1 ∗ 10^ − 9, MaxStepSize → SimTime/100, MaxSteps → 1000000,
PrecisionGoal → 12, AccuracyGoal → 15,
Method → StiffnessSwitching];
B1 = State[t] /. solution1 /.t → 10^t /.t → μ;
Join[{A}, First[ B1]];
Answer1 = Transpose[%];

(*2 : Governing equations for next half cycle, negative gate bias *)
(* Population vector : 0, n, p, nn, pn, pp, nnp, ppn, pnpn *)
Eqnlist = {
Inner[ Equal, State′[t], Evaluate[( JN6[t] + RadiativeD[t] + AugerD[t]). State[t]], List],
Inner[ Equal, State[0], Evaluate[ First[N[ State[t] /. solution1 /.t → SimTime]]], List]
} // Flatten;
solution2 = NDSolve[ ReleaseHold[ Eqnlist],
{ S00[t], S10[t], S01[t], S20[t], S11[t], S02[t], S21[t], S12[t], S22[t]}, {t, 0, SimTime},
StartingStepSize → 1 ∗ 10^ − 9, MaxStepSize → SimTime/100, MaxSteps → 1000000,
PrecisionGoal → 12, AccuracyGoal → 15,
Method → StiffnessSwitching];
B2 = State[t] /. solution2 /.t → 10^t /.t → μ;
Join[{A}, First[ B2]];
```

```
Answer2 = Transpose[%];

(*3 : Governing equations for next half cycle, positive gate bias *)
(* Population vector : 0, n, p, nn, pn, pp, nnp, ppn, pnpn *)
Eqnlist = {
Inner[ Equal, State'[t], Evaluate[( JP6[t] + RadiativeD[t] + AugerD[t]). State[t]], List],
Inner[ Equal, State[0], Evaluate[ First[N[ State[t] /. solution2 /.t → SimTime]]], List]
} // Flatten;
solution3 = NDSolve[ ReleaseHold[ Eqnlist],
{ S00[t], S10[t], S01[t], S20[t], S11[t], S02[t], S21[t], S12[t], S22[t]}, {t, 0, SimTime},
StartingStepSize → 1 * 10^ − 9, MaxStepSize → SimTime/100, MaxSteps → 1000000,
PrecisionGoal → 12, AccuracyGoal → 15,
Method → StiffnessSwitching];
B3 = State[t] /. solution3 /.t → 10^t /.t → μ;
Join[{A}, First[ B3]];
Answer3 = Transpose[%];

(*4 : Governing equations for last half cycle, negative gate bias *)
(* Population vector : 0, n, p, nn, pn, pp, nnp, ppn, pnpn *)
Eqnlist = {
Inner[ Equal, State'[t], Evaluate[( JN6[t] + RadiativeD[t] + AugerD[t]). State[t]], List],
Inner[ Equal, State[0], Evaluate[ First[N[ State[t] /. solution3 /.t → SimTime]]], List]
} // Flatten;
solution4 = NDSolve[ ReleaseHold[ Eqnlist],
{ S00[t], S10[t], S01[t], S20[t], S11[t], S02[t], S21[t], S12[t], S22[t]}, {t, 0, SimTime},
StartingStepSize → 1 * 10^ − 9, MaxStepSize → SimTime/100, MaxSteps → 1000000,
PrecisionGoal → 12, AccuracyGoal → 15,
Method → StiffnessSwitching];
B4 = State[t] /. solution4 /.t → 10^t /.t → μ;
Join[{A}, First[ B4]];
Answer4 = Transpose[%];

(* Concatenate everything and put in linear time *)
A = N[10^μ, 5];
part1 = Transpose[ Join[{A}, First[ B1]]];
part2 = Transpose[ Join[{A + SimTime}, First[ B2]]];
```

```
part3 = Transpose[ Join[{A + 2 * SimTime}, First[ B3]]];
part4 = Transpose[ Join[{A + 3 * SimTime}, First[ B4]]];
AnswerAll = Join[ part1, part2, part3, part4];
Export[ "c:/users/robb/desktop/solution.dat", AnswerAll,
ConversionOptions → { "TableSeparators" ->{ "\n", "\t"}}]

x = Part[ Transpose[ AnswerAll], 1];
y = Part[ Transpose[ AnswerAll], 6];
ListPlot[ Inner[ List, x, y, List], PlotJoined → True]
```

Bibliography

[1] G. E. Moore, *Electronics* **38**, (1965).

[2] International Technology Roadmap for Semiconductors (ITRS) `http://itrs.net/`.

[3] ITRS, *Interconnect*, 2005 Edition.

[4] S. P. Murarka, *Mater. Sci. Eng. R* **19**, 87 (1997).

[5] J. W. Goodman, F. I. Leonberger, S. Y. Kung, and R. A. Athale, *Proc. IEEE* **72**, 850 (1984).

[6] L. C. Kimerling, *Appl. Surf. Sci.* **159/160**, 8 (2000).

[7] D. A. Miller, *Proc. IEEE* **88**, 728 (2000).

[8] S. A. Maier, M. L. Brongersma, P. G. Kik, S. Meltzer, A. A. G. Requicha, and H. A. Atwater, *Adv. Mat.* **13**, 1501 (2001).

[9] A. Shacham, K. Bergman, and L. P. Carloni, *Proc. P=ac^2 Conference*, 12 (2006).

[10] A. Steane, *Rep. Prog. Phys.* **61**, 117 (1998).

[11] E. Knill, R. Laflamme, and G. J. Milburn, *Nature* **409**, 46 (2001).

[12] A. Liu, R. Jones, L. Liao, D. Samara-Rubio, D. Rubin, O. Cohen, R. Nicolaescu, and M. Paniccia, *Nature* **427**, 615 (2004).

[13] B. Schmidt, Q. Xu, J. Shakya, S. Manipatruni, and M. Lipson, *Optics Express* **15** 3140 (2007).

[14] M. A. Green, J. Zhao, A. Wang, P. J. Reece, and M. Gal, *Nature* **412**, 805 (2001).

[15] O. Boyraz, B. Jalali, *Optics Express* **12**, 5269 (2004).

[16] H. Rong, A. Liu, R. Jones, O. Cohen, D. Hak, R. Nicolaescu, A. Fang, and M. Paniccia, *Nature* **433**, 292 (2005).

[17] H. Rong, R. Jones, A. Liu, O. Cohen, D. Hak, A. Fang, and M. Paniccia, *Nature* **433** 725 (2005).

[18] A. W. Fang, H. Park, O. Cohen, R. Jones, M. J. Paniccia, J. E. Bowers, *Optics Express* **14** 9203 (2006).

[19] C. Gunn, A. Narasimha, B. Analui, Y. Liang, T. J. Sleboda, *Proc. SPIE* **6477** (2007).

[20] L. Pavesi and D. J. Lockwood, *Silicon Photonics*, Topics in Applied Physics **94**, Berlin: Springer-Verlag, (2004).

[21] L. T. Canham, *Appl. Phys. Lett.* **57**, 1046 (1990).

[22] A. G. Cullis and L. T. Canham, *Nature* **353**, 335 (1991).

[23] T. Shimizu-Iwayama, K. Fujita, S. Nakao, K. Saitoh, T. Fujita, and N. Itoh, *J. Appl. Phys.* **75**, 7779 (1994).

[24] K. S. Min, K. V. Shcheglov, C. M. Yang, H. A. Atwater, M. L. Brongersma, and A. Polman, *Appl. Phys. Lett.* **69**, 2033 (1996).

[25] T. Shimizu-Iwayama, N. Kunumado, D. E. Hole, and P. Townsend, *J. Appl. Phys.* **83**, 6018 (1998).

[26] M. L. Brongersma, Optical properties of ion beam synthesized Si nanocrystals in SiO_2, PhD thesis, Utrecht University (1998).

[27] J. Linnros, N. Lalic, A. Galeckas, and V. Grivickas, *J. Appl. Phys.* **86**, 6128 (1999).

[28] K. A. Littau, P. J. Szajowski, A. J. Muller, A. R. Kortan, and L. E. Brus, *J. Phys. Chem.* **97**, 1224 (1993).

[29] D. M. Holunga, R. C. Flagan, and H. A. Atwater, *Ind. Eng. Chem. Res.* **44**, 6332 (2005).

[30] Q. Zhang, S. C. Bayliss, and D. A. Hutt, *Appl. Phys. Lett.* **66**, 1977 (1995).

[31] J. U. Schmidt and B. Schmidt, *Mat. Sci. Eng. B* **101**, 28 (2003).

[32] T. Orii, M. Hirasawa, and T. Seto, *Appl. Phys. Lett.* **83**, 3395 (2003).

[33] L. A. Nesbit, *Appl. Phys. Lett.* **46**, 38 (1985).

[34] C. F. Lin, W. T. Tseng, and M. S. Feng, *J. Appl. Phys.* **87**, 2808 (2000).

[35] U. Kahler and H. Hofmeister, *Opt. Mat.* **17**, 83 (2001).

[36] M. Zacharias, J. Heitmann, R. Scholz, U. Kahler, M. Schmidt, and J. Bläsing, *Appl. Phys. Lett.* **80**, 661 (2002).

[37] D. Kovalev, H. Heckler, G. Polisski, J. Diener, and F. Koch, *Opt. Mat.* **17** 35 (2001).

[38] D. Pacifici, *Private Communication*, May 2005.

[39] L. Brus, *J. Phys. Chem.* **90**, 12 (1986).

[40] L. Brus, *IEEE J. Quantum Elec.* **22**, 9 (1986).

[41] K. Leung and K. B. Whaley, *Phys. Rev. B* **56**, 12 (1997).

[42] F. A. Reboredo, A. Franceschetti, and A. Zunger, *Appl. Phys. Lett.* **75**, 2972 (1999).

[43] A. Franceschetti and A. Zunger, *Phys. Rev. Lett.* **78**, 915 (1997).

[44] T. Takagahara and K. Takeda, *Phys. Rev. B* **46**, 15578 (1992).

[45] E. Martin, C. Delerue, G. Allan, and M. Lannoo, *Phys. Rev. B* **50**, 18258 (1994).

[46] T. Takagahara, *Phys. Rev. B* **47**, 4569 (1993).

[47] G. W. Bryant, *Phys. Rev. B* **37**, 8763 (1988).

[48] T. Takagahara and K. Takeda, *Phys. Rev. B* **53**, R4205 (1996).

[49] S. Ögüt, J. R. Chelikowsky, and S. G. Louie, *Phys. Rev. Lett.* **79**, 1770 (1997).

[50] A. Franceschetti, L. W. Wang, and A. Zunger, *Phys. Rev. Lett.* **83**, 1269 (1999).

[51] N. A. Hill and K. B. Whaley, *Phys. Rev. Lett.* **75**, 1130 (1995).

[52] M. V. Wölkin, J. Jorne, P. M. Fauchet, G. Allan, and C. Delerue, *Phys. Rev. Lett.* **82**, 197 (1999).

[53] A. Puzder, A. J. Williamson, J. C. Grossman, and G. Galli, *Phys. Rev. Lett.* **88**, 097401 (2002).

[54] N. Daldosso, M. Luppi, S. Ossicini, E. Degoli, R. Magri, G. Dalba, P. Fornasini, R. Grisenti, F. Rocca, L. Pavesi, S. Boninelli, F. Priolo, C. Spinella, and F. Iacona, *Phys. Rev. B* **68**, 085327 (2003).

[55] G. Ledoux, O. Guillois, D. Porterat, C. Reynaud, F. Huisken, B. Kohn, and V. Paillard, *Phys. Rev. B* **62**, 15942 (2000).

[56] K. S. Cho, N.-M. Park, T.-Y. Kim, K.-H. Kim, G. Y. Sung, and J. H. Shin, *Appl. Phys. Lett.* **86**, 071909 (2005).

[57] T.-Y. Kim, N.-M. Park, K.-H. Kim, G. Y. Sunga, Y.-W. Ok, T.-Y. Seong, and C.-J. Choi, *Appl. Phys. Lett.* **85**, 5355 (2004).

[58] W. Shockley and W. T. Read, Jr., *Phys. Rev.* **87**, 835 (1952).

[59] R. N. Hall, *Phys. Rev.* **87**, 387 (1952).

[60] G. M. Credo, M. D. Mason, and S. K. Buratto, *Appl. Phys. Lett.* **74**, 1978 (1999).

[61] B. Delley and E. F. Steigmeier, *Phys. Rev. B* **47**, 13970 (1993).

[62] D. Kovalev, H. Heckler, M. Ben-Chorin, M. Schwartzkopff, and F. Koch, *Phys. Rev. Lett.* **81**, 2803 (1998).

[63] G. Belomoin, J. Therrien, and M. Nayfeh, *Appl. Phys. Lett.* **77**, 779 (2000).

[64] M. H. Nayfeh, N. Barry, J. Therrien, O. Akcakir, E. Gratton, and G. Belomoin, *Appl. Phys. Lett.* **78**, 1131 (2001).

[65] A. Smith, Z. H. Yamani, N. Roberts, J. Turner, S. R. Habbal, S. Granick, and M. H. Nayfeh, *Phys. Rev. B* **72**, 205307 (2005).

[66] L. Pavesi, L. Dal Negro, C. Mazzoleni, G. Franzò, and F. Priolo, *Nature* **408**, 440 (2000).

[67] L. Dal Negro, M. Cazzanelli, L. Pavesi, S. Ossicini, D. Pacifici, G. Franzò, F. Priolo, and F. Iacona, *Appl. Phys. Lett.* **82**, 4636 (2003).

[68] P. M. Fauchet, J. Ruan, H. Chen, L. Pavesi, L. Dal Negro, M. Cazzaneli, R. G. Elliman, N. Smith, M. Samoc, and B. Luther-Davies, *Opt. Mat.* **27**, 745 (2005).

[69] M. Cazzanelli, D. Navarro-Urriòs, F. Riboli, N. Daldosso, L. Pavesi, J. Heitmann, L. X. Yi, R. Scholz, M. Zacharias, and U. Gösele, *J. Appl. Phys.* **96**, 3164 (2004).

[70] J. S. Biteen, D. Pacifici, N. S. Lewis, and H. A. Atwater, *Nanoletters* **5**, 1768 (2005).

[71] M. Fujii, S. Hayashi, and K. Yamamoto, *J. Appl. Phys.* **83**, 7953 (1998).

[72] A. Mimura, M. Fujii, S. Hayashi, D. Kovalev, and F. Koch, *Phys. Rev. B* **62** 12625 (2000).

[73] M. Fujii, Y. Yamaguchi, Y. Takase, K. Ninomiya, and S. Hayashi, *Appl. Phys. Lett.* **87**, 211919 (2005).

[74] D. Arnold, E. Cartier, and D. J. DiMaria, *Phys. Rev. B* **49** 10278 (1994).

[75] M. Fujii, M. Yoshida, S. Hayashi, and K. Yamamoto, *J. Appl. Phys.* **84**, 4525 (1998).

[76] P. G. Kik, M. L. Brongersma, and A. Polman, *Appl. Phys. Lett.* **76**, 2325 (2000).

[77] P. G. Kik, and A. Polman, *J. Appl. Phys.* **88**, 1992 (2000).

[78] H.-S. Han, S.-Y. Seo, and J. H. Shin, *Appl. Phys. Lett.* **79**, 4568 (2001).

[79] P. G. Kik, Energy transfer in erbium doped optical waveguides based on silicon, PhD thesis, FOM-AMOLF (2000).

[80] D. Pacifici, Erbium doped silicon nanoclusters for microphotonics, PhD thesis, University of Catania (2003).

[81] R. E. Johnson and A. Muan, *J. Amer. Chem. Soc.* **51**, 430 (1968).

[82] B. Garrido, M. López, O. González, A. Pérez-Rodríguez, J. R. Morante, and C. Bonafos, *Appl. Phys. Lett.* **72**, 3145 (2000).

[83] Y. Q. Wang, R. Smirani and G. G. Ross, *Nanotechnology* **15**, 1554 (2004).

[84] A. Claverie, C. Bonafos, G. Ben Assayag, S. Schamm, N. Cherkashin, V. Paillard, P. Dimitrakis, et al., *Defect and Diffusion Forum* **258**, 531 (2006).

[85] `http://www.srim.org/`.

[86] J. F. Ziegler, J. P. Biersack, and U. Littmark, *The Stopping and Range of Ions in Solids*, New York, Pergamon Press, (1985).

[87] P. Normand, D. Tsoukalas, E. Kapetanakis, J. A. Van Den Berg, D. G. Armour, J. Stoemenos, and C. Vieud, *Elec. and Sol. Lett.* **1**, 88 (1998).

[88] T. Müeller, K.-H. Heinig, and W. Möller, *Appl. Phys. Lett.* **81**, 3049 (2002).

[89] G. W. Rubloff, M. Offenberg, and M. Liehr, *IEEE Trans. Semi. Man.* **7**, 96 (1994).

[90] H. Tamura, M. Rückschloss, T. Wirschem, and S. Vepřek, *Appl. Phys. Lett.* **65**, 1537 (1994).

[91] M. L. Ostraat, J. W. De Blauwe, M. L. Green, L. D. Bell, M. L. Brongersma, J. Casperson, R. C. Flagan, and H. A. Atwater, *Appl. Phys. Lett.* **79**, 433 (2001).

[92] A. Meldrum, R. F. Haglund, L. A. Boatner, and C. W. White, *Adv. Mat.* **13**, 1431 (2001).

[93] B. Garrido Fernandez, M. Lpez, C. Garca, A. Prez-Rodrguez, J. R. Morante, C. Bonafos, M. Carrada, and A. Claverie, *J. Appl. Phys.* **91**, 798 (2002).

[94] S. Tiwari, J. A. Wahl, H. Silva, F. Rana, and J. J. Welser, *Appl. Phys. A: Mater. Sci. Process.* **71**, 403 (2000).

[95] T. Feng, Silicon nanocrystal charging dynamics and memory device applications, PhD thesis, California Institute of Technology (2005).

[96] T. Feng, H. B. Yu, M. Dicken, J. R. Heath, and H. A. Atwater, *Appl. Phys. Lett.* **86**, 33103 (2005).

[97] M. Luppi and S. Ossicini, *J. Appl. Phys.* **94**, 2130 (2003).

[98] A. G. Cullis, L. T. Canham, and P. D. J. Calcott, *J. Appl. Phys.* **82**, 909 (1997).

[99] C. Delerue, G. Allan, and M. Lannoo, *Phys. Rev. B* **48**, 11024 (1993).

[100] F. Priolo, G. Franzò, D. Pacifici, V. Vinciguerra, F. Iacona, and A. Irrera, *J. Appl. Phys.* **89**, 264 (2001).

[101] Y. Kanemitsu, T. Ogawa, K. Shiraishi, and K. Takeda, *Phys. Rev. B* **48**, 4883 (1993).

[102] P. Photopoulos, A. G. Nassiopoulou, D. N. Kouvatsos, and A. Travlos, *J. Appl. Phys.* **76**, 3588 (2000).

[103] J. G. Zhu, C. W. White, J. D. Budai, S. P. Withrow, and Y. Chen, *J. Appl. Phys.* **78**, 4386 (1995).

[104] M. L. Brongersma, A. Polman, K. S. Min, E. Boer, T. Tambo, and H. A. Atwater, *Appl. Phys. Lett.* **72**, 2577 (1998).

[105] V. I. Klimov, C. Schwarz, D. McBranch, and C. W. White, *Appl. Phys. Lett.* **73**, 2603 (1998).

[106] F. Iacona, G. Franzò, and C. Spinella, *J. Appl. Phys.* **87**, 1295 (2000).

[107] Z. H. Lu, D. J. Lockwood, and J.-M. Baribeau, *Nature* **378**, 258 (1995).

[108] D. J. Lockwood, Z. H. Lu, and J. M. Baribeau, *Phys. Rev. Lett.* **96**, 539 (1996).

[109] V. Vinciguerra, G. Franzò, F. Priolo, F. Iacona, and C. Spinella, *J. Appl. Phys.* **87**, 8165 (2000).

[110] D. Kovalev, J. Diener, H. Heckler, G. Polisski, N. Künzner, and F. Koch, *Phys. Rev. B* **61**, 4485 (2000).

[111] L. Pavesi, *J. Appl. Phys.* **80**, 216 (1996).

[112] J. S. Biteen, N. S. Lewis, H. A. Atwater, and A. Polman, *Appl. Phys. Lett.* **84**, 5389 (2004).

[113] P. E. Batson and J. R. Heath, *Phys. Rev. Lett.* **71**, 911 (1993).

[114] I. Sychugov, R. Juhasz, J. Valenta, and J. Linnros, *Phys. Rev. Lett.* **94**, 087405 (2005).

[115] J. Valenta, R. Juhasz, and J. Linnros, *Appl. Phys. Lett.* **80**, 1070 (2002).

[116] M. L. Brongersma, P. G. Kik, A. Polman, K. S. Min, and H. A. Atwater, *Appl. Phys. Lett.*, **76**, 351 (2000).

[117] M. L. Brongersma, A. Polman, K. S. Min, and H. A. Atwater, *J. Appl. Phys.* **86**, 759 (1999).

[118] K. R. Williams and R. S. Muller, *J. Microelectromechanical Sys.* **5**, 256 (1996).

[119] J. Dziewior and W. Schmid, *Appl. Phys. Lett.* **31**, 346 (1977).

[120] A. F. van Driel, I. S. Nikolaev, P. Vergeer, P. Lodahl, D. Vanmaekelbergh, and W. L. Vos, *Phys. Rev. B* **75**, 035329 (2007).

[121] M. N. Berberan-Santos, E. N. Bodunov, and B. Valeur, *Chem. Phys.* **315**, 171 (2005).

[122] M. Inokuti and F. Hirayama, *J. Chem. Phys.* **43**, 1978 (1965).

[123] D. L. Dexter, *J. Chem. Phys.* **21**, 836 (1953).

[124] T. Förster, *Ann. Phys.* **2**, 55 (1948).

[125] W. L. Barnes, *J. Mod. Opt.* **45**, 661 (1998).

[126] E. Snoeks, A. Lagendijk, and A. Polman, *Phys. Rev. Lett.* **74**, 2459 (1995).

[127] M. J. A. de Dood, L. H. Slooff, A. Moroz, A. van Blaaderen, and A. Polman, *Phys. Rev. A* **64**, 3807 (2001)

[128] H. P. Urbach and G. L. J. A. Rikken, *Phys. Rev. A* **57**, 3913 (1998).

[129] B. C. Buchler, T. Kalkbrenner, C. Hettich, and V. Sandoghdar, *Phys. Rev. Lett.* **95**, 6 (2005).

[130] D. Barba, F. Martin, C. Dahmoune, and G. G. Ross, *Appl. Phys. Lett.* **89**, 034107 (2006).

[131] R. Smirani, F. Martin, G. Abel, Y. Q. Wang and G. G. Ross, *Nanotechnology* **16**, 32 (2005).

[132] S. M. Orbons, M. G. Spooner, and R. G. Elliman, *J. Appl. Phys.* **96**, 4650 (2004).

[133] E. F. Schubert, A. M. Vredenberg, N. E. J. Hunt, Y. H. Wong, P. C. Becker, J. M. Poate, D. C. Jacobson, L. C. Feldman, and G. J. Zydzik, *Appl. Phys. Lett.* **61**, 1381 (1992).

[134] R. S. Anderssen, S. A. Husain, and R. J. Loy, *ANZIAM J.* **45**(E), C800 (2004).

[135] F. Cichos, J. Martin, and C. von Borczyskowski, *Phys. Rev. B* **70** 115314, (2004).

[136] R. Sprik, B. A. van Tiggelen, and A. Lagendijk, *Europhys. Lett.* **35**, 265 (1996).

[137] P. D. J. Calcott, K. J. Nash, L. T. Canham, M. J. Kane, and D. Brumhead, *J. Phys. Cond. Matt.* **5**, L91, (1993).

[138] K. H. Drexhage, *Prog. Opt.* **12**, 165 (1974).

[139] E. D. Palik (ed.), *Handbook of Optical Constants of Solids*, New York: Academic Press (1985).

[140] M. D. Mason, G. M. Credo, K. D. Weston, and S. K. Buratto, *Phys. Rev. Lett.* **80**, 5405 (1998).

[141] P. Andrew and W. L. Barnes, *Science* **290**, 27 (2000).

[142] T. Nakamura, M. Fujii, K. Imakita, and S. Hayashi, *Phys. Rev. B* **72**, 235412 (2005).

[143] S. Miura, T. Nakamura, M. Fujii, M. Inui, and S. Hayashi, *Phys. Rev. B* **73**, 245333 (2006).

[144] G. W. 't Hooft, Y. A. R. R. Kessener, G. L. J. A. Rikken, and A. H. J. Venhuizen, *Appl. Phys. Lett.* **61** 2344 (1992).

[145] M. Kapoor, K. Singh, and R. K. Pandey, *Physica E* **23**, 183 (2004).

[146] T. Müeller, K.-H. Heinig, and W. Möller, *Mat. Sci. Eng. B* **101**, 49 (2003).

[147] J. A. Rajchman, *J. Appl. Phys.* **41**, 1376 (1970).

[148] D. A. Parthenopoulos and P. M. Rentzepis, *Science* **245**, 843 (1989).

[149] M. Kroutvar, Y. Ducommun, J. J. Finley, M. Bichler, G. Abstreiter, and A. Zrenner, *Appl. Phys. Lett.* **83**, 443 (2003).

[150] T. Lundstrom, W. Schoenfeld, H. Lee, P. M. Petroff, *Science* **286**, 2312 (1999).

[151] S. Tiwari, F. Rana, H. Hanafi, A. Hartstein, E. F. Crabbé and K. Chan, *Appl. Phys. Lett.* **68**, 1377 (1996).

[152] H. Hanafi and S. Tiwari, IEEE Trans. Elec. Dev. **43**, 1553 (1996).

[153] R. Muralidhar, et al., Proceedings of the IEEE IEDM, 26.2.1 (2003).

[154] R. F. Steimle, M. Sadd, R. Muralidhar, R. Rao, B. Hradsky, S. Straub, and B. E. White, Jr., IEEE Trans. Nano. **2**, 335 (2003).

[155] J. J. Lee and D.-L. Kwong IEEE Trans. Elec. Dev. **52**, 507 (2005).

[156] S. Huang, S. Banerjee, R. T. Tung, and S. Odaa, *J. Appl. Phys.*, **93**, 576 (2003).

[157] J. Grosvalet and C. Jund, IEEE Trans. Elec. Dev. **ED-14**, 777 (1967).

[158] D. M. Kim, S. J. Song, H. T. Kim, S. H. Song, D. J. Kim, K. S. Min, and D. W. Kang, IEEE Trans. Elec. Dev. **50**, 1131 (2003).

[159] M. Nirmal, B. O. Dabbousi, M. G. Bawendi, J. J. Macklin, J. K. Trautman, T. D. Harris, L. E. Brus, *Nature* **383**, 802 (1996).

[160] C. Wang, M. Shim, P. Guyot-Sionnest, *Science* **291**, 2390 (2001).

[161] J. Valenta, N. Lalic, and J. Linnros, *Appl. Phys. Lett.* **84**, 1459, (2004).

[162] G. Franzo, A. Irrera, E. C. Moreira, M. Miritello, F. Iacona, D. Sanfilippo, G. Di Stefano, P. G. Fallica, and F. Priolo, *Appl. Phys. A* **74**, 1 (2002).

[163] S. Fujita and N. Sugiyama, *Appl. Phys. Lett.* **74**, 308 (1999).

[164] J. De la Torre, A. Souifi, A. Poncet, C. Busseret, M. Lemiti, G. Bremond, G. Guillot, O. Gonzalez, B. Garrido, J. R. Morante, and C. Bonafos, *Physica E* **16**, 326 (2003).

[165] M. Kulakci, U. Serincan, and R. Turan, *Semicond. Sci. Tech.* **21**, 1527 (2006).

[166] A. Fojtik, J. Valenta, T. H. Stuchlíková, J. Stuchlík, I. Pelant, J. Kočka, *Thin Solid Films* **515**, 775 (2006).

[167] Y. B. Park and D. K. Schroder, *IEEE Trans. Elec. Dev.* **45**, 1361 (1998).

[168] C. Canali, C. Jacoboni, F. Nava, F. Ottaviani, and A. Alberigi-Quaranta, *Phys. Rev. B* **12**, 2265 (1975).

[169] K. Han, I. Kim, and H. Shin, *IEEE Trans. Elec. Dev.* **48**, 874 (2001).

[170] J. G. Simmons, *J. Appl. Phys.* **34**, 1793, (1963).

[171] B. Leriche, Y. Leroy, and A. S. Cordan, *J. Appl. Phys.* **100**, 074316 (2006).

[172] J. G. Simmons, *Phys. Rev.* **155**, 657 (1967).

[173] L. Manchanda, R. H. Storz, R. H. Yan, K. F. Lee, and E. H. Westerwick, *Proc. IEEE IEDM* 28.7.2 (1992).

[174] P. Su, K.-I. Goto, T. Sugii, and C. Hu, *IEEE Elec. Dev. Lett.* **23**, 550 (2002).

[175] J. Frenkel, *Phys. Rev.* **54**, 647 (1938).

[176] S. Hüfner, *Optical Spectra of Transparent Rare Earth Compounds*, New York: Academic Press (1978).

[177] D. A. Pinnow, T. C. Rich, F. W. Ostermayer, Jr., and M. DiDomenico, Jr., *Appl. Phys. Lett.* **22**, 527 (1973).

[178] R. J. Mears, L. Reekie, I. M. Jauncey, and D. N. Payne, *Optical Fiber Communication* **3** W12 (1987).

[179] C. R. Giles and E. Desurvire, *J. Lightwave Tech.* **9**, 271 (1991).

[180] S. Coffa, G. Franzò, and F.Priolo, *Appl. Phys. Lett.* **69**, 2077 (1996).

[181] A. J. Kenyon, P. F. Trwoga, M. Federighi, and C. W. Pitt, *J. Phys.: Condens. Matter* **6**, L319 (1994).

[182] M. Fujii, M. Yoshida, Y. Kanzawa, S. Hayashi, and K. Yamamoto, *Appl. Phys. Lett.* **71**, 1198 (1997).

[183] M. Fujii, M. Yoshida, S. Hayashi, and K. Yamamoto, *J. Appl. Phys.* **84**, 4525 (1998).

[184] T. Komuro, T. Katsumata, T. Morikawa, X. Zhao, H. Isshiki, and Y. Aoyagi, *Appl. Phys. Lett.* **74**, 377 (1999).

[185] G. Franzò, V. Vinciguerra, and F. Priolo, *Appl. Phys. A: Mat. Sci. Proc.* **69**, 3 (1999).

[186] G. Franzò, F. Iacona, V. Vinciguerra, and F. Priolo, *Mat. Sci. Eng. B* **69/70**, 338 (1999).

[187] G. Franzò, D. Pacifici, V. Vinciguerra, F. Iacona, and F. Priolo, *Appl. Phys. Lett.* **76**, 2167 (2000).

[188] S.-Y. Seo, and J. H. Shin, *Appl. Phys. Lett.* **78**, 2709 (2001).

[189] K. Watanabe, M. Fujii and S. Hayashi, *J. Appl. Phys.* **90**, 4761 (2001).

[190] F. Priolo, G. Franzò, F. Iacona, D. Pacifici, V. Vinciguerra, *Mat. Sci. Eng. B* **81**, 9 (2001).

[191] F. Iacona, D. Pacifici, A. Irrera, M. Miritello, G. Franzò, F. Priolo, D. Sanfilippo, G. Di Stefano, and P. G. Fallica, *Appl. Phys. Lett.* **81**, 3242 (2002).

[192] H.-S. Han, S.-Y. Seo, J. H. Shin, and N. Park, *Appl. Phys. Lett.* **81**, 3720 (2002).

[193] J. H. Shin, H.-S. Han, and S.-Y. Seo, *Towards the First Silicon Laser*, edited by L. Pavesi, S. Gaponenko, and L. Dal Negro, NATO Science Series **93**, Dordrecht: Kluwer Academic Publishers (2003)

[194] P. G. Kik and A. Polman, *J. Appl. Phys.* **91**, 534 (2002).

[195] P. G. Kik and A. Polman, *Towards the First Silicon Laser*, edited by L. Pavesi, S. Gaponenko, and L. Dal Negro, NATO Science Series **93**, Dordrecht: Kluwer Academic Publishers (2003)

[196] A. Polman, *J. Appl. Phys.* **82**, 1 (1997).

[197] D. Pacifici, G, Franzò, F. Priolo, F. Iacona, and L. Dal Negro, *Phys. Rev. B* **67**, 245301 (2003).

[198] G. Allan, C. Delerue, and M. Lannoo, *Phys. Rev. Lett.* **78**, 3161 (1997).

[199] G. N. van den Hoven, E. Snoeks, A. Polman, C. van Dam, J. W. M. van Uffelen, M. K. Smit, *J. Appl. Phys.* **79**, 1258 (1996).

[200] J. H. Shin, *Appl. Phys. Lett.* **82**, 4489 (2003).

[201] A. Polman, *Nature Materials* **1**, 10 (2002).

[202] T. Nakamura, M. Fujii, S. Miura, M. Inui, and S. Hayashi, *Phys. Rev. B* **74**, 045302 (2006).

[203] D. Yu Remizov, V. B. Shmagin, A. V. Antonov, V. P. Kuznetsov, and Z. F. Krasilnik, *Phys. Solid State* **47**, 98 (2005).

[204] G. Franzò, F. Priolo, S. Coffa, A. Polman, and A. Carnera, *Appl. Phys. Lett.* **64**, 2235 (1994).

[205] G. Franzò, S. Coffa, F. Priolo, and C. Spinella, *J. Appl. Phys.* **81**, 2784 (1997).

[206] W. Jantsch, G. Kocher, L. Palmetshofer, H. Przybylinska, M. Stepikhova, and H. Preier, *Mat. Sci Eng. B* **81**, 86 (2001).

[207] A. Irrera, D. Pacifici, M. Miritello, G. Franzò, F. Priolo, F. Iacona, D. Sanfilippo, G. Di Stefano, and P. G. Fallica, *Appl. Phys. Lett.* **81**, 1866 (2002).

[208] K. G. Svantesson, *J. Phys. D: Appl. Phys.* **12**, (1979).

[209] J. H. Shin, S.-Y. Seo, S. Kim, S. G. Bishop, *Appl. Phys. Lett.* **76**, 1999 (2000).

[210] M. Fujii, K. Imakita, K. Watanabe, S. Hayashi, *J. Appl. Phys.* **95**, 272 (2004).

[211] K. Imakita, M. Fujii, and S. Hayashi, *Eur. Phys. J. D* **34**, 161 (2005).

[212] B. L. Wehrenberg, C. Wang, and P. Guyot-Sionnest, *J. Phys. Chem. B* **106**, 10634 (2002).

[213] V. I. Klimov, A. A. Mikhailovsky, D. W. McBranch, C. A. Leatherdale, and M. G. Bawendi, *Science* **287**, 1011 (2000).

[214] R. D. Schaller, M. Sykora, J. M. Pietryga, and V. I. Klimov, *Nano Lett.* **6**, 424 (2006).

[215] L. Bakuevaa, S. Musikhin, M. A. Hines, T.-W. F. Chang, M. Tzolov, G. D. Scholes, and E. H. Sargent, *Appl. Phys. Lett.* **82**, 2895 (2003).

[216] J. S. Steckel, S. Coe-Sullivan, V. Bulović, and M. G. Bawendi, *Adv. Mater.* **15**, 1862 (2003).

[217] D. Basko, G. C. La Rocca, F. Bassani, and V. M. Agranovich, *Eur. Phys. J. B* **8**, 353 (1999).

[218] M. Achermann, M. A. Petruska, S. Kos, D. L. Smith, D. D. Koleske and V. I. Klimov, *Nature* **429**, 642 (2004).

[219] Q. Xu, V. R. Almeida and M. Lipson, *Optics Letters* **29**, 1626 (2004).